Effect of impurities in a nickel sulfate electrolyte on internal stress development, morphology and adhesion to titanium of electrodeposited nickel

by

Emmanuel Nsanda Nsiengani

Supervisor: Prof. R.F. Sandenbergh

A dissertation submitted in partial fulfilment of the requirement of the degree of

Master of Applied Sciences (Metallurgy)

Department of Materials Science and Metallurgical Engineering

FACULTY OF ENGINEERING, BUILT ENVIRONMENT AND INFORMATION TECHNOLOGY

University of Pretoria

South Africa

2017

Acknowledgement

I would like to express my sincere gratitude to my supervisor Professor R.F Sandenbergh for his guidance and encouragement in the achievement of this work.

I'm also grateful to:

- my colleagues for the fruitful discussions, ideas and supply of experimental materials

- Mr Robert Cromarty, Mr Salmon and Mr Carole for their assistance and facilities

- my family members for their love, support and encouragement during the long way of achievement of this work.

Abstract

Successful electrowinning and electrorefining processes for the production of high purity and compact electroplated metal require the optimization of the electrolyte composition and operating parameters. In nickel electrowinning and electrorefining plants the optimization of the electrolyte composition for good deposit morphology, optimal adhesion to the substrate, and minimum energy requirements remains a challenge. The influence of some impurities usually present in nickel sulfate electrolytes on the stress level, morphology and adhesion of nickel deposits were investigated using both quantitative and qualitative assessments, such as internal stress, adhesion, grain size and chemical composition measurements, complemented by visual observation of the morphology and condition of the plated nickel.

The results indicate that both the internal stress and yield stress increased, but at different rates, with impurities such as copper, cobalt, chromium and aluminium in the electrolyte. The impurity level at which the internal stress exceeded the yield stress typically resulted in cracking and/or disbonding of the plated metal and could be used to define the allowable impurity levels. The impurity metal contents of the plated nickel increased proportionally to the concentrations of copper, cobalt and chromium in the electrolyte, but not so in the case of aluminium where a maximum was found at an intermediate concentration in the range of concentrations studied. The measured internal stress in the deposits followed the trend of impurity contents in the nickel for aluminium, chromium and copper, while a slight decrease in internal stress was observed at low cobalt concentrations in the electrolyte. It was also found that nickel adhesion to the titanium substrate is relatively weaker in the presence of impurities, with aluminum being the worse impurity, followed by copper, cobalt and chromium impurities, respectively.

Table of contents

Acknowledgement.....I

Abstract.....II

List of tables VI

List of figures.....VII

Chapter 1 Introduction.....1

1.1 Background.....1

1.2 Problems relating to impurities.....1

1.3 Challenge to control stress in nickel deposits 3

1.4 Objective of the work.....3

Chapter 2 Literature review.....4

2.1 Background on stress in nickel deposits 4

2.1.1 Introduction.....4

2.1.2 Some practical measures in industrial plants for influencing deposit morphology and adhesion. 5

2.1.3 Effect of operating parameters on internal the stress development in nickel 6

2.1.4 Mechanism of stress development in the nickeldeposit.....7

2.1.5 Review of previous work.....7

2.2 Overview of nickel electrowinning and nickel electrodeposits 11

2.2.1 Electrowinning of nickel..... ..11

2.2.1.1 Electrolytes, conditions and reactions of nickel electrowinning.....11

2.2.1.2 Electrodeposition from sulfate electrolytes.....13

2.2.1.2.1 Activity of nickel in sulfate solutions 13

2.2.1.2.2 Metallic ion species in the electrolyte.....15

2.2.1.2.3 Mass transport of ions in the electrolyte.....15

2.2.1.2.4 Notion of double layer.....16

2.2.1.2.5 Mechanism of nickel electrodeposition.....17

2.2.1.2.6 Ions discharging at the cathode.....18

2.2.1.2.7 Hydrogen ion reduction at the cathode 22

2.2.1.2.8 Electrocrystallisation process.....28

2.2.1.2.9 Behaviour of metallic impurities present in the electrolyte during electrodeposition.....30

2.2.1.2.10 Electrowinning cell design.....31

2.2.2 Nickel electrodeposits 33

2.2.2.1 Characteristics of nickel metal.....33

2.2.2.2 Nature and origins of internal stresses in electrodeposits..... 33

2.2.2.3 Mechanical properties of nickel.....38

2.2.2.4 Mechanical properties of titanium.....40

2.2.2.5 Effects of impurities on stress in electrodeposits.....40

2.2.2.6 Effect of impurities on the mechanical properties of Electrodeposits 41

2.2.2.7 Constrained electrodeposits 42

2.2.2.8 Brittle fracture mechanism and fracture criteria 43

2.3 Method to assess internal stress 44

2.3.1 Stress measurements in deposited films.....44

2.3.1.1 Curvature based methods 45

2.3.1.2 Stoney equation and its limits.....46

2.3.2 Determination of mechanical properties of the deposit.....47

2.3.3 Methods used for adhesion test of electrodeposits.....49

2.3.3.1 Scratch test method.....50

2.3.3.2 Limitation of the scratch test.....51

2.3.4 Analytical techniques for nickel electrodeposits.....51

Chapter 3 Experimental and analysis.....53

3.1 Electrodeposition experiments.....53

3.2 Internal stress measurement.....54

3.3 Yield stress determination.....55

3.4 Adhesion strength assessment.....55

3.5 Analysis of the deposit.....57

3.6 Potentiodynamic tests.....58

3.7 Range of impurity concentrations investigated.....58

Chapter 4 Results and discussion.....60

4.1 Internal stress in nickel deposits as a function of impurity concentration in the electrolyte 60

4.2 Internal stress in nickel deposits as a function of impurity concentration in the deposit.....62

4.3 Mechanical properties and maximum stress criteria on nickel deposits.....63

4.4 Deposit morphology.....69

4.5 Chemical composition of nickel deposits as a function of the impurity concentration in the electrolyte……71

4.6 Current efficiency……75

4.7 Potentiodynamic polarisation curves……76

4.8 Energy-dispersive X-ray spectrometry analysis of the nickel deposits……79

4.9 Relative adhesion strength of the nickel deposit to the titanium substrate as a function of impurity concentration in the electrolyte……84

5 Conclusions ……88

6 References ……90

7 Appendices……102

List of tables

Table 2.1. Comparison of typical internal stress levels in nickel deposited from different types of electrolytes (Kopeliovich, 2013)……5

Table 2.2. Typical electrowinning operating conditions of some nickel plants (Ji, 1994; Crundwell, 2011; Pavlides, 2000) ……12

Table 2.3. Reactions taking place during nickel electrowinning (Ji, 1994)……..13

Table 2.4. Hydrogen discharge overpotential on different cathode materials (C. Lupi et al., 2006)……23

Table 2.5. Allowable impurity concentrations in the electrolyte for smooth and compact nickel deposits from sulfate electrolytes……31

Table 2.6. Characteristics of nickel metal (Wikipedia, 2015)……33

Table 2.7. Elastic stiffness coefficients for some metals (Allard, 1969)…… …….33

Table 2.8. Lattice constants a_o of common crystal structures as a function of atomic radius of materials (Ouyang, 2009) ……35

Table 2.9. Typical values of tensile properties of nickel (Davis, 2000; Soboyejo et al., 2003; Haluzan, 2004, Mehregany and Roy, 1999) ……39

Table 3.1. Electrolyte impurity concentrations used for: internal stress measurement, yield stress determination, and adhesion at deposit-substrate interface …….. ……59

Table 4.1. Measured grain size and calculated yield stress induced by impurities in nickel deposit……68

Table 4.2. Visual observation on the morphology of nickel deposited on the stiff titanium substrate at different concentrations of impurities ……70

Table 4.3. Chemical composition of the nickel deposits as a function of impurity concentrations in the electrolyte ……73

Table 4.4. Comparaison of the trend of EDS-SEM and ICP-MS results on nickel electrodeposited from aluminium and chromium containing electrolytes……..84

List of figures

Figure 2.1. Schematic representation of the double layer (Liu et al., 2011)……16

Figure 2.2. E-pH diagram for nickel in aqueous solution at 25°C and 1M for soluble species (Schweitzer et al, 2010) ……..19

Figure 2.3. Distribution vs pH diagram of aqueous boron (III) species ……24

Figure 2.4. E-pH diagram of Cu-H_2O system at 25°C and 10^{-1} M for soluble species (Schweitzer et al, 2010)…….. ……25

Figure 2.5. E-pH diagram of Co-H_2O system at 25°C and 10^{-1} M for soluble species (Schweitzer et al, 2010)…….. ……26

Figure 2.6. E-pH diagram of Cr-H_2O system at 25°C and 10^{-1} M for soluble species (Schweitzer et al, 2010)…….. ……27

Figure 2.7. E-pH diagram of Al-H_2O system at 25°C and 10^{-1} M for soluble species (Schweitzer et al, 2010)…….. ……..28

Figure 2.8. Schematic of an electrocrystallisation process (Schwartz, 1994) ….30

Figure 2.9. Metallic structure and defects (Giallonardo, 2013). ……38

Figure 2.10. Typical true stress - true strain curve for pure nickel metal (Hesegawa and Fukutomi, 2002) ……..40

Figure 3.1. Schematic presentation of the experimental setup used for internal stress measurements in the electrodeposited nickel……..54

Figure 3.2. Schematic presentation of the experimental setup used for adhesion strength measurements at the deposit-substrate interface……57

Figure 4.1. Measured internal stresses in electroplated nickel as a function of impurity concentrations in the electrolyte of up to 60 and 100 mg/L……61

Figure 4.2. Internal stresses in electroplated nickel as a function of higher electrolyte impurity concentrations. ……62

Figure 4.3. Variation of the (a) aluminium content in nickel electrodeposited from aluminium containing electrolytes, (b) internal stress and calculated yield stress, as a function of concentration of aluminium in the electrolyte ……64

Figure 4.4. Variation of the (a) copper content in nickel electrodeposited from copper containing electrolytes, (b) internal stress and calculated yield stress, as a function of concentration of copper in the electrolyte. ……65

Figure 4.5. Variation of the (a) cobalt content in nickel electrodeposited from cobalt containing electrolytes, (b) internal stress and calculated yield stress, as a function of concentration of cobalt in the electrolyte ……66

Figure 4.6. Variation of the (a) chromium content in nickel electrodeposited from chromium containing electrolytes, (b) internal stress and calculated yield stress, as a function of concentration of chromium in the electrolyte ……67

Figure 4.7. Typical photographs representing different nickel deposit conditions as a function of impurity concentration in the electrolyte……71

Figure 4.8. Chemical composition of the nickel deposits as a function of impurity concentrations in the electrolyte ……74

Figure 4.9. Current efficiency vs concentration of impurities in the electrolyte……76

Figure 4.10. Potentiodynamic cathodic polarisation from aluminium containing electrolyte……77

Figure 4.11. Potentiodynamic cathodic polarisation from chromium containing electrolyte……78

Figure 4.12. Electrode overpotential in terms of nickel plating vs impurity concentration in the electrolyte……79

Figure 4.13. EDS spectrum of nickel electrodeposited from 20, 300, 625 and 2500 mg/L aluminium impurity in the electrolyte……82

Figure 4.14. EDS spectrum of nickel electrodeposited from 80 and100 mg/L chromium impurity in the electrolyte ……86

Figure 4.15. Normal load vs friction force measured during scratch tests on nickel electroplated from nickel electrolytes containing the concentrations of copper……..85

Figure 4.16. Normal load vs friction force measured during scratch tests on nickel electroplated from nickel electrolytes containing the concentrations of cobalt ……..86

Figure 4.17. Normal load vs friction force measured during scratch tests on nickel electroplated from nickel electrolytes containing the concentrations of chromium……86

Figure 4.18. Normal load vs friction force measured during scratch tests on nickel electroplated from nickel electrolytes containing the concentrations of aluminium……..87

Figure 4.19. Friction coefficients at separation vs impurity concentration in the electrolyte for various impurities.....87

Chapter 1 Introduction

1.1 Background

Industrial electrodeposition of high purity nickel is of great importance in the nickel industry. It is conducted either by electrowinning or electrorefining from electrolytes generally containing impurities from leaching of comminuted and upgraded nickel ore, or the leaching of nickel ore without prior concentration (heap leaching), or leaching of precipitates or nickel-containing solids obtained from other hydrometallurgy processes (typically in base metal refineries), or dissolution of smelted and cast mattes of sulfides or crude metals from pyrometallurgical processes. In electrowinning and electrorefining processes, nickel is primarily produced in the form of sheets and to a lesser extent in the form of crowns. These electrodeposition processes for nickel metal production involve the reduction of the nickel ions present in the electrolyte to nickel metal deposited onto a substrate, coupled to the oxidation of water or chloride for sulfate and chloride electrolytes, respectively, to conserve the charge balance in the electrolyte. The main difference between the two electrodeposition processes resides in the source of nickel ions in the electrolyte and the nature of the anode, with purified nickel-containing solution fed to a cell fitted with an insoluble anode for electrowinning, whilst the nickel is anodically dissolved from an impure soluble anode in the case of electrorefining. The process at the cathode in terms of reactions and mechanism are similar for both electrowinning and electrorefining in terms of ion reduction, nucleation and growth of the plated metal, as in other electrodeposition processes, such as electroforming.

1.2 Problems relating to impurities

Nickel is usually plated by electrowinning or electrorefinning on permanent cathodes made of stainless steel, with suitable dimensions and mechanical properties, to avoid additional processes required to produce and form substrates of thin starter metals, as can alternatively be done. Recently, the use of permanent cathode substrates made of titanium has been introduced in a nickel electrowinning plant, Rustenburg Base Metal Refinery (the only nickel plant using sulfate electrolyte and titanium cathodes; other nickel plants using titanium cathodes with chloride electrolytes are provided in table 2.2). Poor adhesion and deposit morphology have been noticed, which were related to excessive stress in the deposit, although moderate adhesion of the plated nickel to the electrode is required such that it does not peel off during

electrowinning, but also that it may be removed without too much difficulty at the end of the plating cycle.

In modern nickel electrowinning and electrorefining plants where the cell configuration is such that the anode and the cathode are parallel and separated by a relatively short distance (typically around 20 mm), the above mentioned consequences of high stresses can cause among others, short circuits in the electrodeposition cells in case of direct contact of anode and cathode, causing serious losses in terms of current efficiency, energy consumption and production. The characterization and understanding of internal stress development in nickel electrodeposit is thus of great importance.

Impurities present in the electrolytes, among many other causes of stress development in nickel deposits, may significantly affect stress generation, and thus adhesion to the substrate and deposit morphology, on top of their effects on the efficiency of the plating process and the purity of the plated nickel. Electrolytes always contain trace or relatively higher concentrations of impurities due to the limitations of the purification processes and the accumulation of impurities in the electrolyte over time.

In previous work, studies of the effect of impurities on the morphology of nickel deposits have been carried out on other type of substrates, e.g., stainless steel, and under electrodeposition conditions typically not used in practical plants. Moreover, the assessment in terms of morphology was only based on visual observations, with little information on the adhesion of nickel to the substrate (Kittelty, 2002; Das and Gogia, 1988, 1991; Holm and O'Keefe, 2000; Mohanty et al., 2005). This work focused on the effects of copper, cobalt, chromium and aluminium impurities under conditions close to those of practical nickel electrowinning on a titanium substrate. The assessment of the effect of impurities on the quality of the electrodeposit was done by following the internal stresses developed in the deposit and estimating the mechanical properties based on measured grain sizes. The effect of impurities on the tendency for delamination from the substrate was evaluated by measuring parameters related to the interface adhesion strength, such as the critical load and relative friction coefficient of scratch tests.

1.3 Challenge to control stress in nickel deposits

Internal stresses are influenced by numerous parameters, many of them are interdependent, so that the stress state in the deposit is related to a particular set of conditions of all interdependent parameters that obviously require optimization. A change of one parameter may affect many others and the stress level in the deposit. A typical list of parameters that affect the internal stresses in an electrodeposition process includes the current density, the electrolyte temperature, the solution pH, the nature and concentration of impurities and additives in the electrolyte, the cell geometry, the cathode-to-anode area ratio, the quality of the direct current (DC) power, and the metal concentration in the electrolyte (Stein, 1996), of which the temperature, pH, current density and electrolyte composition are the main parameters. Moreover, impurities in the electrolyte are time dependent, because they tend to accumulate, which makes the prediction and control of the deposit morphology and adhesion to the substrate a challenge.

1.4 Objective of the work

In this work the focus was on the development of stress in nickel deposits obtained from sulfate solutions as influenced by copper, cobalt, chromium and aluminium present in the electrolyte. The aim was to correlate the nature and concentration of the impurities with the stress level in the nickel deposit to predict the morphology in terms of continuous, compact, delaminated, cracked or peeled deposits, as well as the relative plated metal-to-substrate adhesion strength on a titanium electrode under electrowinning conditions.

Chapter 2 Literature review

2.1 Background on stress in nickel deposits

2.1.1 Introduction

For nickel metal production by electrowinning, the cathode used to initiate the electrowinning process may be in the form of a thin starter sheet of the same metal that becomes part of the metal product, in which case maximum adhesion is desirable. This is typically not favoured because of the additional processes required to produce and form these thin starter metals onto electrodes with suitable dimensions and mechanical properties. The use of permanent cathodes, made from materials such as stainless steels and titanium, is typically preferred. In this case, the adhesion of the plated metal should be carefully controlled to maintain adhesion during the plating process, but should also allow the convenient separation of the plated metal from the substrate at the end of the plating cycle. In contrast, the electrodeposition conditions are typically chosen such that a high rate of metal production is achieved while maintaining good quality deposits in terms of morphology and smoothness to reduce impurity entrapment in the deposit and assure an uniform current distribution over the cathode area to obtain a deposit of uniform thickness and acceptable appearance (Jing et al., 2010).

Unfortunately, relatively high internal stresses are typically developed during nickel plating compared with other metals such copper and zinc. Stresses may be such that the plated metal disbonds from the substrate or delaminates, cracks, curls or peels, resulting in a non-uniform current distribution and even shorting to the anode. This is especially the case when nickel is electroplated from the sulfate and chloride electrolytes typically used for electrowinning and electrorefining (Ji, 1994; Jing et al., 2010; Crundwell et al., 2011), which is in contrast to the decorative and functional plating of nickel from sulfamate and Watts electrolytes where internal stress development is typically not a problem (Schlesinger and Paunovic, 2010; Parkinson, 2009). Table 2.1, taken from Kopeliovich (2013), shows the magnitude of internal stresses typically developed for the industrial electroplating of nickel.

Table 2.1. Comparison of typical internal stress levels in nickel deposited from different types of electrolytes (Kopeliovich, 2013).

Type of solution	Chemicals	Concentration (g/L Ni)	Temperature (°C)	pH	Boric acid (g/L)	Tensile strength (MPa)	Internal stress (MPa)	Current density (A/dm^2)
Chloride	$NiCl_2.6H_2O$	225 - 300	43 - 65	1 - 3	30 - 35	620 - 930	275 - 340	2.5 - 10
Sulfate	$NiSO_4.6H_2O$	225 - 400	38 - 70	1.5 - 4	30 - 45	415 - 485	200 - 300	1 - 10
Watts solution	$NiCl_2.6H_2O$ $NiSO_4.6H_2O$	240 - 300 30 - 90	40 - 65	3 - 4.5	30 - 45	345 - 485	125 - 185	2 - 10
Sulfate-chloride	$NiCl_2.6H_2O$ $NiSO_4.6H_2O$	150 - 225 150 - 225	43 - 52	1.5 - 2.5	30 - 45	480 - 725	200 - 275	2.5 - 15
Sulfamate	$Ni(SO_3N_2)_2$ $NiCl_2.6H_2O$	300 - 450 0 - 30	40 - 60	3.5 - 4.5	30 - 45	415 - 610	0 - 55	2 - 25
Hard	$NiSO_4.6H_2O$ NH_4Cl	180 25	43 - 60	5.6 - 5.9	30	415 - 610	0 - 55	2.5 - 5
Fluoroborate	Ni(BF4)2 $NiCl_2.6H_2O$	225 - 300 0 - 15	38 - 70	2.5 - 4	15 - 30	380 - 600	90 - 200	3 - 25

2.1.2 Some practical measures in industrial plants for influencing deposit morphology and adhesion

In both electrowinning and electrorefining, carefully controlled moderate adhesion of the deposit to the substrate is required to not only ensure the integrity of the cathode deposit during plating but also such that the removal of the deposit after electrodeposition can be readily done. Plating of compact and smooth deposits is also aimed for industrial plants. To achieve these requirements, on top of optimization of electrodeposition parameters, isolating strips are fitted to the edges of the cathode substrate to prevent the formation of an envelope of plated metal that would be very difficult to remove from the substrate, and three small holes or

so, of about 3 mm diameter are typically made in the cathode substrate to allow the bonding of plated metal through these holes to counter the peeling of the plated metal from the substrate during electrowinning due to internal stresses (Crundwell et al., 2011). The bonding to the substrate is further managed by controlling the roughness and surface condition of the substrate, the use of surfactants, and by controlling the initial stages of the electroplating process to achieve more or less bonding, as required. Bonding inside the plated metal itself may become an issue if plating is interrupted for some time and changes in the surface condition are such that lesser bonding is achieved when plating is resumed. The development of internal stresses during plating thus significantly complicates the management of the adhesion between the plated metal and the cathode, especially when stresses become excessive. The use of stress-reducing additives, typically saccharin (Schlesinger and Paunovic, 2010), is also usual in some plants to control the stress level in the nickel deposit and prevent cracked and delaminated deposits. The optimization of plating conditions and the levels of impurities in the electrolyte are the best ways to control issues of both deposit adhesion and morphology.

2.1.3 Effect of operating parameters on internal stress development in nickel

In addition to the electrolyte composition, the bath temperature, pH and current density are the main operating parameters in electrowinning and electrorefining of nickel that affect the stress in a nickel deposit in different ways. The cell electrolyte is usually heated to increase the solution conductivity and the kinetics. Moreover, when other parameters are kept constant, internal stress usually shifts to less tensile or more compressive values with increased temperature (Watson, 1989; Goods et al., 2006). The optimal bath temperature in nickel electrolytes is generally chosen to balance the stress level in the deposit and the energy consumption of the process and is about 60^{o}C for electrowinning in sulfate electrolytes. Operating at high pH ranges generally lead to the precipitation of nickel and /or other metallic impurities present in the electrolyte. Precipitation typically occurs on the surface of the cathode where the pH may be significantly elevated due to hydrogen ion reduction. When reporting in the nickel lattice, such solid precipitates increase the internal stress, probably by localised lattice distortions, and spoil the deposit quality macroscopically. Thermodynamically, hydrogen reduction is more favourable than nickel ion reduction to nickel metal. Significant hydrogen gas is typically evolved at the cathode surface in the low pH ranges, a fraction of which may incorporate in the

nickel deposit and cause deposit embrittlement (Eastman et al., 1980; Sofronis et al., 2001; Bernstein and Thompson, 1976). The typical acceptable pH range for electrowinning of nickel is between 1.5 and 4, and mostly around 3.5 for sulfate solutions, to prevent excessive hydrogen evolution at low pH values and the precipitation of solid particles as hydroxides at high pH values (Ji, 1994). Internal stress levels in the nickel deposit are strongly dependent on the operating range of current density and usually increase to more tensile values with increased current density.

2.1.4 Mechanism of stress development in nickel deposits

Internal stresses are usually defined as forces that develop in a three-dimensional (3D) body or a two-dimensional (2D) surface when all the external boundaries are free of traction. Such forces develop in deposits obtained from electrodeposition as well. The mechanism of internal stress development in metal electrodeposits is not yet completely understood (Moharana, 2013); however, many mechanisms of stress development have been proposed in terms of island coalescence, grain growth, lattice distortion, impurity incorporation, vacancy annihilation, shrinkage of grain boundaries, voids, and grain boundary relaxation (Moharana, 2013; Ziebell and Schuh, 2012, Nicol and kittelty, 2001; Kittelty, 2002). The study of these mechanisms for the development of the internal stress in the nickel deposit is beyond the scope of this work.

2.1.5 Review of previous work

Previous work reported in the literature focused mainly on plating from sulfamate and Watts electrolytes, with relatively little reported work on stress development during nickel plating from sulfate or chloride electrolytes. Previous work on stress in nickel and its dependence on other parameters in various electrolytes are briefly reviewed in this section.

Watson (1989) reported a change from compressive to tensile stress in Watts and sulfamate electrolytes with increasing current density in the range of 250-3800 A/m^2 at 60^{o}C and pH 4, with zero stress in sulfamate at about 1800 A/m^2. This work also mentioned that, as stress increased to more tensile values with increasing current density and to more compressive values with increasing solution temperature, it was possible to choose pairs of suitable values that gave deposits with zero internal stress by controlling these two parameters. Such conditions would, however, not be

attractive for electrowinning from sulfate electrolytes as the low deposition rate at lower current densities and excessive energy consumption at higher temperatures would make these less attractive. An increase in internal stress with current density in sulfamate electrolytes was also observed by Pathak et al. (2011). They found that the internal stress varied from 74.5 MPa to 94.1 MPa when the current density varied from 15 A/m^2 to 50 A/m^2, with a decrease in the hardness of the deposit as the grain size increased. Luo et al. (2006) investigated the effect of process conditions on the properties of electroplated nickel thin films from a sulfamate solution (300 g/L) at 60^{o}C and pH 3.8. They found a change from compressive to tensile stress from -120 to +120 MPa when the current density varied from 10 to 300 A/m^2. However, in contrast to most other work, they also found a shift to more tensile stresses with increasing temperatures from 20 to 80^{o}C. Such response to the change of temperature has also been reported in the work of Woo and Kim (2011) in sulfate solutions of 225-410 g/L at 40^{o}C, where the stress increased to more tensile values when the temperature increased from 20 to 80^{o}C at a constant current density of 86 A/m^2, with zero stress at 45^{o}C and compressive stresses for lower temperatures. They also reported that the stress shifted to more tensile values with increasing the current density from 50 to 900 A/m^2.

The internal stress was found to slightly decrease with increased pH in the range of 0 to 4 in a Watts solution (Schlesinger and Paunovic, 2010) and significantly increased in the pH range of 4 to 6. This may be linked to the effects of, respectively, hydrogen evolution and precipitation at low and high pH ranges. They also found a decrease of internal stress followed by an increase in internal stress as the current density was varied from 100 to 1300 A/m^2 with a minimum internal stress at around 900 A/m^2 at pH 3 and 55^{o}C.

Holm and O'Keefe (2000) assessed the significance of nickel concentration, pH and bath temperature in the absence of additives on current efficiency and morphology using a stainless steel cathode blank in an aqueous sulfate electrolyte. They reported that these parameters caused poor deposit morphologies when set at improper levels. Typically, 60 g/L nickel in 150 g/L sodium sulfate, pH 2.5 and 40^{o}C resulted in more ductile, compact and flat deposits, compared with a poor deposit obtained at 20 g/L nickel. Improved deposit morphologies were obtained at higher nickel concentrations, e.g., 40 g/L and 50 g/L, with other parameters being maintained constant. Ductile and flat deposits were obtained at pH 2 in 40 g/L nickel, 150 g/L

sodium sulfate and 40°C solution, while severely degraded and extensively cracked and curled deposits were obtained at relatively higher pH values of 2.5 and 3.5. The use of a temperature of 60°C in the latter work dramatically improved the morphology of the deposit but poor morphology and brittle deposits were obtained, even with pure electrolyte at lower temperatures.

In the work of Kittelty (2002) and Nicol and Kittelty (2001), on the electrocrystallization of nickel and its relationship to the physical properties of the nickel, stress generated in the nickel deposit, expressed in terms of shear strain, was found independent of the current density, but was decreased with increasing nickel concentration in the electrolyte and increased with increased electrolyte pH with formation of nickel hydroxide in the <111> planes. The development of tensile stress in the deposit was attributed to the reduction of inter-crystallite spacings of the nickel crystals that grow together, thereby reducing the volume available for growth, as well as the size and shape of the nickel crystals, and the formation of structural defects in the crystalline structure such as those caused by hydrogen pits, that disrupt the growth of the nickel. Smaller crystals size was associated with higher strain in the deposits and a harder deposit. A columnar structure in the nickel deposit was found highly stressed compared with a fan-shaped structure. They also found that the adhesion of the nickel to the titanium substrate was quite low compared with the stainless steel and could be controlled with the anodization of the titanium surface.

Impurities in the electrolyte, as well as the temperature and the pH, affect other electrolyte parameters such as electrical conductivity and density (Wu et al., 2003), which, in turn, can greatly influence the electrodeposition process by influencing the energy consumption, mass transfer, incorporation of particulates into the nickel deposits and the deposit morphology. Electrodeposition parameters are thus interdependent and affect each other.

The effects of impurities during nickel electrodeposition from sulfate solutions have also been studied under different working conditions. However, the assessment was mostly limited only to the physical appearance of the deposits.

Das and Gogia (1988) studied the effects of Mg^{2+}, Mn^{2+}, Zn^{2+} and Al^{3+} during electrowinning of nickel from a sulfate bath at 30°C, pH of 2.5, 400 A/m^2, 60 g/L, nickel, and 12 g/L for both boric acid and sodium sulfate. Their study of Al^{3+} carried

out up to 100 mg/L showed increasing aluminium contents in the deposit with increasing concentrations of Al^{3+} in the electrolyte with a slight decrease in current efficiency, and serious degradation of the quality of the deposit above 5 mg/L Al^{3+}. They suggested that the contamination of the deposit was due to the precipitation of hydroxides or codeposition along with nickel.

In their other study on the effect of Cu^{2+}, Co^{2+}, Fe^{2+} and Fe^{3+} during electrowinning of nickel from sulfate solutions under the above conditions (Das and Gogia, 1991), they found tolerance limits of 100 mg/L, 500 mg/L and 5 mg/L for copper, cobalt and iron (II), respectively, for good deposits. Their results showed codeposition of all these impurities with the nickel and only minor effects of these impurities on the current efficiency in the range of concentrations studied. The shift of potentiodynamic curves in the presence of low Fe^{2+} and Co^{2+} to more negative and more positive values, respectively, compared with that of impurity-free nickel electrolyte, was related to the anomalous codeposition of these impurities with nickel.

O'Keefe and Holm (2000) studied the anomalous behaviour of Al^{3+} in nickel electrowinning from sulfate electrolytes of 40 g/L nickel at pH 2.5 and 3.5 and temperatures of 40^0C and 60^0C in the absence of a modifying agent. They noticed serious degradation of the deposit morphology and current efficiency with 20 mg/L to 100 mg/L Al^{3+}. Bad morphologies were also found at low temperatures, typically 40^oC, and/or a high electrolyte pH of 3.5. Higher concentrations, e.g., 1 g/L Al^{3+}, in the electrolyte decreased the current efficiency and prevented the deposition of metallic nickel, giving instead a green and black layer that might have allowed significant hydrogen evolution with hydroxide layer formation. However, a higher addition of 5 g/L Al^{3+} again gave a smooth and compact deposit that might be due to the role of Al^{3+} as modifying agent, similar to that of boric acid or NH_4^+.

The electrodepostion of nickel in the presence of Al^{3+} in a sulfate solution was studied by Mohanty et al. (2005) in the range of 0 to 40 mg/L Al^{3+}, for 60 g/L nickel electrolyte with 12 g/L of both boric acid and sodium sulfate. The increase in aluminium content in the deposit with increased aluminium concentration in the electrolyte was related to hydroxides and a surface pH rise, with significant deterioration of the deposit observed from 10 mg/L Al^{3+}. A shift to more negative potentials of potentiodynamic polarization diagrams in the presence of aluminium in the electrolyte was also related to the formation of hydroxide. However, the experimental pH and temperature used in this work were not reported

Aluminium, cobalt and copper impurities as well as iron and zinc, all at 20 mg/L in the electrolyte, were found to incorporate into the deposit (Kittelty, 2002; Nicol and Kittelty, 2001). Copper caused an increase in the strain, while low levels of aluminium in the electrolyte (20 and 40 mg/L) caused a large disruption of growth and a highly stressed deposit that possibly due to the formation of $Al(OH)_3$. However, they found that a higher concentration of aluminium, i.e. 2700 mg/L, in the presence of boric acid, produced smooth nickel deposits with a low impurity content, but deposits from electrolytes with intermediate aluminium concentrations in the presence of boric acid were not assessed. This was attributed to a possible increase in pH buffering capacity of the solution at high aluminium concentrations. Only two experiments were run at 2700 mg/L Al^{3+} in the electrolyte in the presence of boric acid, that gave a high measured strain for the first and a low one for the repeat, making difficult the result interpretation. 20 mg/L chromium was shown not to affect the nickel electrocrystallization process but a trace of chromium was found in the nickel deposit.

2.2 Overview of nickel electrowinning and nickel electrodeposits

2.2.1 Electrowinning of nickel

2.2.1.1 Electrolytes, conditions and reactions of nickel electrowinning

Electrowinning of nickel is usually carried out from three types of electrolytes: typically sulfate, chloride and sulfate-chloride mixtures (Ji, 1994), with the operating parameters and the cell configuration closely related to the nature of the electrolyte used. Typically, for sulfate electrolytes, electrowinning is conducted in a range of pH 2 to 4, as lower pH values give excessive hydrogen evolution at the cathode surface, while higher pH values, lead generally to the formation of hydroxide precipitates of metallic cations in the electrolyte that may be entrained in the deposit and spoil the deposit quality. A current density of 200 - 240 A/m^2 is usual and represents a balance between the rate of deposition and the deposit quality, as high current densities may lead to dendritic or powdery metal deposits. To improve the kinetics of reactions at the electrodes, the conductivity of the electrolyte and the deposit quality, electrowinning from sulfate is usually carried out in the range of temperatures of 60 to 65^{o}C. The anolyte is typically separated by a membrane from the catholyte to lower the transport of hydrogen ion generated at the anode to the cathode surface

where it would compete with the nickel reduction and significantly reduce the current efficiency. A positive hydrostatic head is also typically maintained in the cathode bag relative to the anolyte to reduce the rate of mass transport of hydrogen ions to the cathode compartment by carefully controlling the flow of electrolyte (Pavlides, 2000; Brown and Mason, 1977). The types of additives and the dimensions of the electrodes differ from one plant to another.

The main advantages of sulfate solutions over chloride and sulfate-chloride solutions are less corrosion, the possibility to use less-expensive lead or lead-alloy anodes, much simpler equipment as there is no gas to be collected for environmental reasons and the possibility to produce electrodeposits with acceptable internal stress levels. However, the industrially optimal current densities attainable in sulfate solutions are significantly lower than those for chloride-based electrolytes, mainly due to the relatively lower activity of nickel in sulfate electrolytes (Wu et al., 2003; Holm and O'Keefe, 2000; Ji, 1994). A sulfate-chloride solution is usually used for electrowinning using the matte from traditional matte-smelting operations as anodes. Typical operating conditions available in the literature for some nickel electrowinning plants are given in Table 2.2 and the reactions taking place during electrowinning at the electrodes are described in Table 2.3.

Table 2.2. Typical electrowinning operating conditions of some nickel plants (Ji, 1994; Crundwell et al., 2011; Pavlides, 2000).

Company	Ni^{2+} (g/L)	Boric acid (g/L)	Na_2SO_4 (g/L)	T (^oC)	Current density (A/m^2)	pH	Cell voltage (V)	Cathode	Anode	Electrolyte
Outokumpu (Finland)	97			60	200 - 230	3.5	3.6	Acid-proof steel	Pb	Sulfate
Rustenburg (South Africa)	80	6 - 10	120	60 - 65	205 - 230	3.5	3.6 - 3.9	Ni sheet (2009); Ti (2011)	Pb-Sn-Sr	Sulfate
Falconbridge (Norway)	60	-	-	60	220	-	-	-	DSA	Chloride
Sumitomo Metal Mining (Japan)	50	-	-	55 - 60	233	1 - 1.2	3.0	Ti	DSA	Chloride
Societe Le Nickel (France)	-	-	-	-	500	-	-	Ti	Graphite	Chloride
Vale	75	8	120	50	240	3 - 4	3.6	Stainless steel	Ni anode matte	

- : not used or no data has been provided

T: Temperarature

Table 2.3. Reactions taking place during nickel electrowinning (Ji, 1994).

	Matte electrowinning	Nickel sulfate electrowinning	Nickel chloride electrowinning
Anode reactions	$Ni_3S_2 \rightarrow 3Ni^{2+} + 2S + 6e^-$ $Ni \rightarrow Ni^{2+} + 2e^-$ $Cu \rightarrow Cu^{2+} + 2e^-$	$2H_2O \rightarrow 4H^+ + O_2 + 4e^-$	$2Cl^- \rightarrow Cl_2 + 2e^-$
Cathode reactions	$Ni^{2+} + 2e^- \rightarrow Ni$ $2H^+ + 2e^- \rightarrow H_2$	$Ni^{2+} + 2e^- \rightarrow Ni$ $2H^+ + 2e^- \rightarrow H_2$	$Ni^{2+} + 2e^- \rightarrow Ni$ $2H^+ + 2e^- \rightarrow H_2$
Desired cell reactions	$Ni_3S_2 \rightarrow 3Ni + 2S$	$2NiSO_4 + 2H_2O \rightarrow 2Ni + 2H_2SO_4 + O_2$	$NiCl_2 \rightarrow Ni + Cl_2$
E^o_{cell} at 25°C (V)	0.35	1.48	1.61

2.2.1.2 Electrodeposition from sulfate electrolytes

For metals to electrodeposit, ions in the electrolyte have to move to the cathode surface and be transformed from hydrated metal ions to the metal. This paragraph describes the background of the main successive steps in the electrodeposition process.

2.2.1.2.1 Activity of nickel in sulfate solutions

When an ion in solution is surrounded by other ions, it behaves differently from its ideal behaviour when it is alone in the solution. A factor called activity coefficient is used in thermodynamics to account for deviations from ideal behaviour in a mixture of ions. It provides the activity of species in aqueous solution, which is obtained by multiplying the species molar concentration by the activity coefficient of the species, which can be written as:

$$a_i = \gamma_i (C_i/C_0) \quad (2.1)$$

where C_i is the species concentration in the electrolyte (mol/L),

C_0 is the species standard state concentration in the electrolyte (mol/L),

a_i is the activity of the species,

γ_i is the activity coefficient of the species.

The activity of a specie in the electrolyte is related to the concentration of other ionic species in the electrolyte through the relationship between the activity coefficient of

the specie and the ionic strength of the solution given by the Debye-Hückel equation (Brahmajirao et al., 2012) as:

$$\log \gamma_i = (- z_i^2 q^2 k)/(8 \varepsilon_r \varepsilon_o K_b T) = - A z_i^2 I^{½} \quad (2.2)$$

where q is the elementary charge (C),

k is the Debye screening length (nm),

ε_r is relative permittivity of the solvent (F/m),

ε_o is the permittivity of free space (8.85 F/m),

K_b is the Boltzmann's constant ($1.38\ 10^{-23}$ m^2 kg/S k),

T is the temperature of the solution (K),

I is the ionic strength of the solution (mol/L),

A is a constant depending on the solvent,

γ_i is the activity coefficient of a species.

Ions in a nickel sulfate electrolyte contribute to increase the ionic strength of the electrolyte; however, because the concentrations of impurity ions are far lower (typically less than 1 g/L) compared with other ionic species, such as Ni^{2+} or SO_4^{2-}, their contribution to the ionic strength should be relatively low, even for trivalent impurity ions such as Al^{3+} or Cr^{3+}. However, the addition of significant sodium sulfate to the electrolyte, e.g., 80 - 160 g/L, to increase the conductivity of the electrolyte, would also significantly change the ionic strength and hence the activity of nickel present in the electrolyte. This should increase the overpotential for plating but decrease the energy loss in the electrolyte, which may account for more than 15% of the total energy required for the nickel electrowinning process, which is significantly more than the energy loss for copper or zinc electrowinning (Wu et al., 2003). The ionic strength of the solution and hence the nickel activity coefficients should thus not change significantly in the presence of the impurities and may be regarded as constant for this purpose.

2.2.1.2.2 Metallic ion species in the electrolyte

Impurities investigated in this work were introduced to the electrolyte as sulfates of Cu(II), Co(II), Al(III) and Cr(III) for copper, cobalt, aluminium and chromium, respectively, which dissolve readily in aqueous medium because all sulfates are soluble in water except the few particular cases known, such as those of Ag(I), Ba(II), Ca(II) and Pb(II). Once dissolved in solution, metallic ions may be involved in hydrolysis reactions with water to form species of the $M_n(OH)_m^{(n-m)}$ form which are likely more stable and thus predominate at relatively higher pH values, e.g., neutral or alkaline conditions. In acidic media, typically around the pH of 3.5 used in this work, the bivalent ions Ni^{2+}, Cu^{2+} and Co^{2+} are the predominant species for nickel, copper and cobalt, respectively, while the trivalent ions Al^{3+} and Cr^{3+} are the predominant species for aluminium and chromium, respectively, as follows from the respective E-pH diagrams in range of impurity concentrations, i.e., 10^{-3}—10^{-5} M (Schweitzer and Pesterfield, 2010; Alrehaily et al., 2013; Christina et al., 2012; Cuppett et al., 2006).

2.2.1.2.3 Mass transport of ions in the electrolyte

The transport of ions in the electrolyte to the electrode, typically cations to the cathode and anions to the anode, occurs through three basic mechanisms namely, by diffusion, convection and migration (Garrido, 2009):

1. Diffusion occurs due to the concentration gradient of ions that develops close to the electrode surface due to the removal or addition of ions from and to the solution by the electrochemical reactions. The flux of ion transport by diffusion at steady state is given by Fick's first law.

2. Convection is due to the hydrodynamic velocity of the solution that typically results from density gradients generated by gas evolution and, to a lesser extent, by the generation or removal of ions at the electrodes. In the case of nickel electrowinning cells, the electrolyte is typically separated into catholyte and anolyte compartments, with fluid interaction being limited by bagging one or both electrodes. Fluid flow close to the cathode is thus limited to that generated by the evolution of hydrogen gas, the hydrostatic head between the catholyte and anolyte, the density gradient due to the removal of metal ions from the electrolyte and the flow of fresh solution into the cathode bag.

3. Migration of ions is due to the presence of a potential gradient in the electrolyte between the electrodes. This is typically not a major transport mode for the metal to be plated because the electrolyte typically contains an abundance of more mobile supporting ions that carry most of the charge between the electrodes.

2.2.1.2.4 Notion of a double layer

Metallic ions in the electrolyte are hydrated and brought to the cathode through the mass transport modes described above. Once in the vicinity of the electrode surface, they distribute in proportion to the electrostatic and other forces present and dehydrate as they move closer to the electrode surface (Schwartz, 1994). If a flat electrode is considered, the net effect is that the negatively charged cathode surface and the positively charged layer of cations close to the surface of the electrode may be considered as the two parallel plates of a capacitor, called the double layer. The reality is, however, more complicated, with distinct planes formed by adsorbed dehydrated cations closest to the surface and by the more distant still hydrated cations, with these planes being called, respectively, the inner (IHP) and outer Helmholtz (OHP) planes. The latter is separated from the bulk solution by a diffuse layer (generally about 10^{-7} m thick), where the concentration of cations decreases with increasing distance into the bulk solution. Internal stress development in electrodeposited metals is likely also affected by the double layer conditions but this relationship is not yet well understood. A schematic representation of a typical double layer in the vicinity of a cathode is given in Figure 2.1.

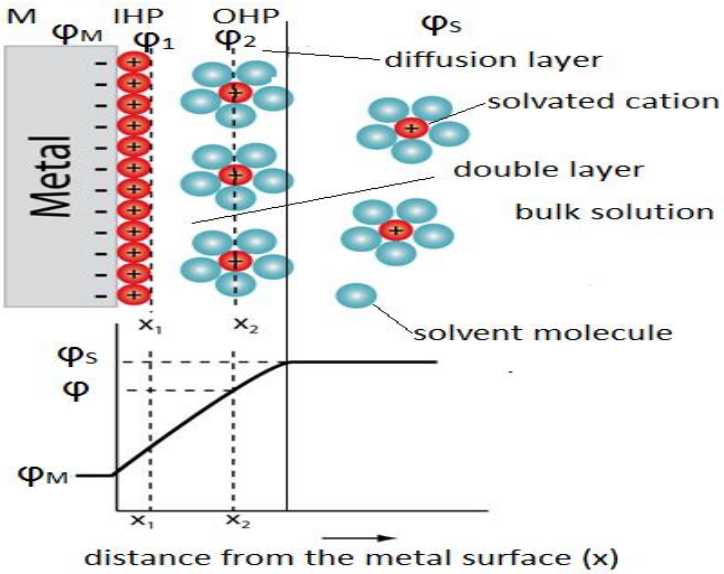

Figure 2.1. Schematic representation of the double layer (Liu et al., 2011).

2.2.1.2.5 Mechanism of nickel electrodeposition

The mechanism of nickel electrodeposition is not well understood. Most authors assume a mechanism that involves two consecutive one-electron charge transfer steps and with the participation of anions such as OH^-, SO_4^{2-}, or Cl^-, in the formation of an adsorbed complex (Smith et al., 2006; Epelboin et al., 1981). Some other studies of electrochemical deposition of nickel have indicated that nickel monohydroxide ions $NiOH^+$ are the main species in the charge transfer steps in aqueous unbuffered solutions and that adsorbed intermediates such as $Ni(OH)_{ads}$ or chloride-containing complexes take part in the mechanism (Hessani, 1989; Santana et al., 2009). Watson and Walters (1991) and Smith et al. (2006) studied the mechanism of Ni^{2+} reduction from acidic sulfate, chloride and Watts electrolytes using impedance studies and characterised the hydrogen evolution reaction on the nickel deposit.

The most accepted nickel electrodeposition mechanism is that of Epelboin et al. (1981). The sequence of reactions suggested by Epelboin et al. (1981) for an electrolyte with pH 2 - 4 is as follows:

$$2H^+ + 2e^- \rightarrow H_2 \quad (2.3)$$

$$N^{2+} + e^- \rightarrow Ni^+_{(ads)} \quad (2.4)$$

$$Ni^+_{(ads)} + e^- \rightarrow Ni^o \quad (2.5)$$

$$Ni^+_{(ads)} + Ni^{2+} + 2e^- \rightarrow Ni^o + Ni^+_{(ads)} \quad (2.6)$$

$$Ni^+_{(ads)} + H^+ + e^- \rightarrow Ni^+_{(ads)} + H^*_{(ads)} \quad (2.7)$$

$$2H^*_{(ads)} \rightarrow H_2 \quad (2.8)$$

$$Ni^+_{(ads)} + H^*_{(ads)} + e^- \rightarrow Ni + H_{(included)} \quad (2.9)$$

This mechanism suggests the existence of a more or less solvated, intermediate adion $Ni^+_{(ads)}$, probably complexed as $NiOH_{ads}$, resulting from electron transfer at the cathode surface on the bivalent nickel ion present in the electrolyte (Equation 2.4), that acts as both catalyst and intermediate consumed for the nickel atom Ni^o formation as described in Equations 2.5 and 2.6, respectively. It also suggests that in sulfuric solution, a similar intermediate $H^*_{(ads)}$ can be formed on the surface of a growing nickel deposit under the catalytic influence of the $Ni^+_{(ads)}$ intermediate according to the Equation 2.7, which will be slowly consumed resulting in either

hydrogen evolution or hydrogen inclusion as described in Equations 2.8 and 2.9, respectively.

2.2.1.2.6 Ions discharging at the cathode

The reduction of ions at the cathode surface occurs via electron transfer from the negatively charged electrode to the ions at the electrode surface. A net transfer of electrons occurs only at potentials more negative than the reversible potential of the half cell, which is described for non-standard conditions by the Nernst equation, indicated as Equation 2.10. A reverse process for oxidation of species with electron transfer to the electrode occurs at the anode, which is water oxidation with oxygen gas evolution for electrowinning from sulfate solutions. Theoretically, the cell voltage required for both oxidation at the anode and reduction at the cathode is the algebraic difference between the two electrode half-cell potentials (Ec- Ea), that is about 1.5 V for nickel ion reduction at the cathode ($Ec^o = -0.25V_{SHE}$) and water oxidation with oxygen gas evolution at the anode ($Ea^o = +1.23V_{SHE}$) for nickel electrowinning from a sulfate electrolyte at pH 0. A typical E-pH diagram for nickel in aqueous solution at 1 M nickel is given in Figure 2.2.

$$E = E^o + \frac{R\,T}{n\,F} \ln a(Me^{n+}) \qquad (2.10)$$

where E^o is standard reversible potential (V),

T is the temperature (K),

$a(Me^{n+})$ is the metal ion activity,

F is the Faraday's constant (96 485 C/mol),

n is the ion valence (mol electrons/mol).

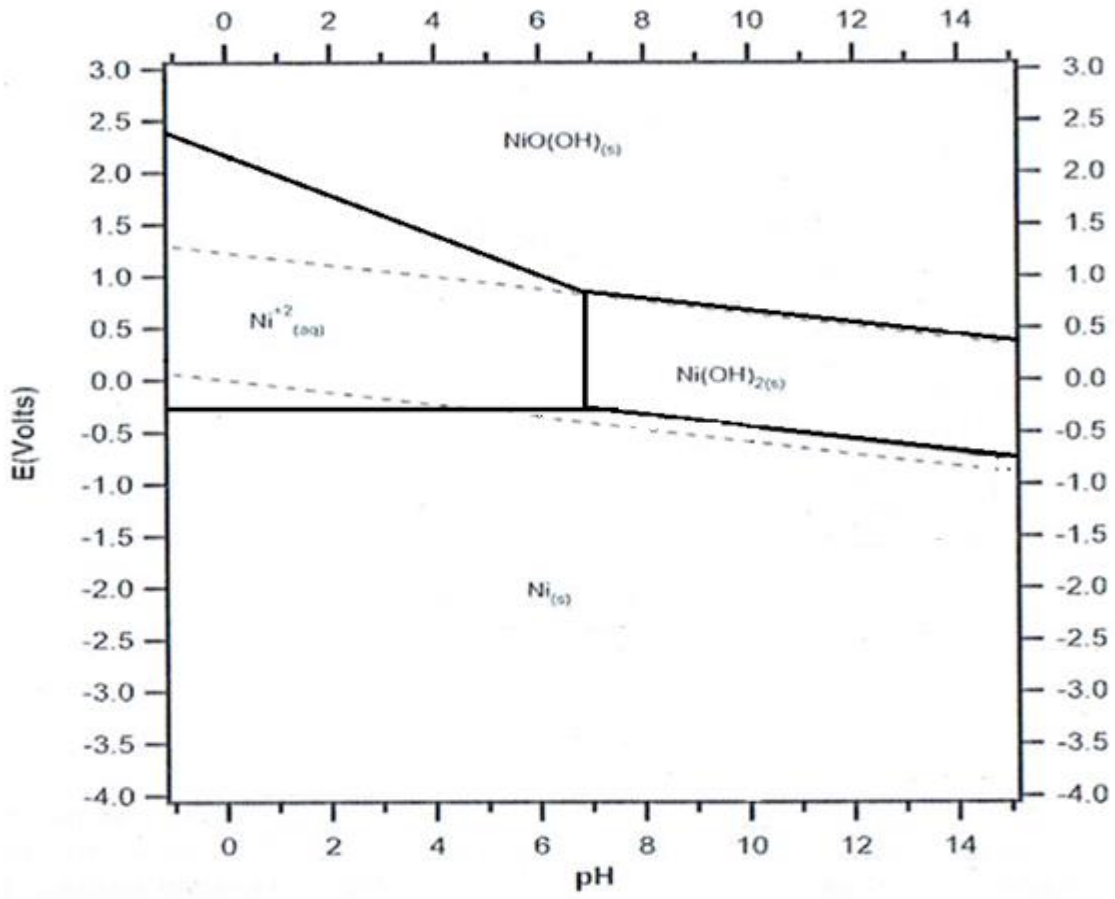

Figure 2.2. E-pH diagram for nickel in aqueous solution at 25°C and 1 M for soluble species. ΔG° in kJ/mol: Ni (0.0), Ni^{2+} (-45.7), $Ni(OH)_2$ (-446.9), NiO(OH) (-316.9), $NiOH^+$ (-227.3), $HNiO_2^-$ (-350.0), H_2O (-237.2), H^+ (0.0), OH^- (-157.3) (Schweitzer and Pesterfield, 2010).

In practice, the electrode potentials required for the reduction reaction at the cathode and oxidation reaction at the anode to occur at significant rates are much higher than the reversible potentials, such that a cell voltage of typically 3.6 - 3.9 V is required to electrodeposit nickel onto a substrate for nickel electrowinning from sulfate electrolytes (Crundwell et al., 2011; Ji, 1994). The extra voltage is apart from the cathodic and anodic overpotentials, also due to the ohmic drop in the electrolyte, and that over the contacts and conductors. The cell voltage is thus the sum of these potentials, as indicated by Equation 2.11.

$$V = Ec - Ea + \eta_c + \eta_a + \sum RI \qquad (2.11)$$

where V is the cell voltage (V),

Ec and Ea are, respectively, the cathode and anode electrode potentials (V),

η_c and η_a are, respectively, the cathode and anode overpotentials (V),

∑RI is the sum of the ohmic potential drops in the contacts and electrolyte (V).

The overpotentials, or driving force required for electrodeposition at the cathode where nickel deposits, may be categorized in the following terms:

(a) Diffusion overpotential: the partial overpotential due to the decrease in the concentration of species at the interface, resulting from the inability of the mass transfer to keep pace with the rate of reduction of the species at the interface. In the limiting case, the concentration at the interface will drop to very low values and the rate of electroreduction will become independent of the potential of the electrode because it will now only be determined by the rate of mass transfer to the interface, which is only slightly dependent on the potential gradient next to the electrode.

(b) Reaction overpotential: the partial overpotential due to the chemical reactions that influence the concentrations of reactants or products in the vicinity of the electrode. The chemical process can be a homogenous reaction in solution or heterogeneous at the electrode surface. This partial overpotential component is significant when the reactions are slow. Dehydration of ions in the electrolyte prior to reduction at the electrode surface and different intermediate steps involving ad-ions in the reduction process are typical reactions that require a reaction overpotential driving force.

(c) Transfer overpotential: the partial overpotential due to slow electron transfer from the electrode to the solution species. Generally, reactions involving the breaking of strong chemical bonds have a large transfer component.

(d) Crystallization overpotential: the partial overpotential due to the incorporation of the product into or release of the reactant from the metal lattice. Large crystallization components are found when these processes are hindered. The relative contributions of the various overpotentials to the overall polarization of the electrode have important consequences in determining the morphology of the electrodeposited metals.

In the electrowinning process, the current density is an important factor that determines the metal production rate and has a strong influence on the quality of the deposit. The current density typically used for nickel electrowinning from sulfate electrolytes is relatively low compared with that from chloride electrolytes due to the relatively lower nickel concentration attainable in sulfate electrolytes (Ji, 1994). The

choice of the current density to be used depends on numerous parameters which may broadly be characterised as those that influence the mass transfer rate of the species to be reduced to the electrode and those that inhibit the plating process itself. Nickel plating from sulfate electrolytes is naturally inhibited and the maximum current density at which good quality deposits can be obtained is typically defined at around one third of the mass transfer limiting current density, e.g., 200 to 240 A/m^2 at a temperature of 60 to 65°C (Deni, 1994; Ji, 1994). The relationship between the rate of charge transfer, i.e., the current, and the overpotential at the electrode may be described in terms of the Butler-Volmer equation (2.12) if charge transfer is rate determining and the contributions of the other overpotentials are small (Garrido, 2009):

$$i = n F k_o C_R^{\alpha} Co^{(1 - \alpha)} [e^{- \alpha f \eta} - e^{(1 - \alpha) f \eta}] \quad (2.12)$$

with $f = F/RT$ and $\eta = E - E_{eq}$

where k_O is the standard rate constant (m/s),

η is the overpotential (V),

n is the metal valence (mol electrons/mol),

C_R is the concentration of the reduced species (mol/L),

C_O is the concentration of the oxidised species (mol/L),

α is the transfer coefficient (a measure of the energy barrier symmetry),

T is the temperature (K),

F is the Faraday constant (96 485 C/mol).

The rates at which impurities in the electrolyte are reduced will depend on the reversible potential of the half-cell reactions involved but are, in many cases, under mass transfer control due to the rather low concentrations at which impurity ions are present in the electrolyte. If it is presumed that the impurities plate uniformly over the whole surface, which is typically not the case, and that the process is at steady state, then the rate of plating may be described by the limiting case of Fick's first law (2.13):

$$i_L = DnFC/\delta \quad (2.13)$$

where D is the diffusion coefficient (m^2/s),

n is the number of electrons exchanged (1/mol),

C is the concentration of the impurity in the electrolyte (mol/m^3),

F is the Faraday's constant (96 485 C/mol),

δ is the mass transfer layer thickness (m),

i_L is the limiting current density (A/m^2).

2.2.1.2.7 Hydrogen ion reduction at the cathode

The standard reversible potential for hydrogen ion reduction to hydrogen gas is 0 volt Standard Hydrogen Electrode (V_{SHE}) as the E-pH diagram in Figure 2.2 shows, i.e., it is far more positive than that required for the reduction of the nickel ion to nickel metal (– 0.25 V_{SHE}) under standard conditions (25°C, 1 M). Although the hydrogen half-cell potential decreases with pH, it is still more positive than that of nickel at the pH of 3.5 typically used in this work. This indicates that the driving force for hydrogen ion reduction under nickel plating conditions should be highly favoured and unless, kinetically hindered, should be the dominant cathodic reaction. Nickel is indeed a good catalyst for the reduction of hydrogen ions, as indicated by the rather low overpotential for hydrogen discharge, as listed in Table 2.4. The presence of hydrogen on the surface of the electrode may also cause a localised reduction in the current density, such that if the bubbles adhere to the surface for a significant time, the local electrode potential may be more positive under the bubble than that required for nickel plating and would cause dissolution of the nickel below the bubble. The pit so formed may stabilise the adherence of the bubble on the surface of the nickel such that deep pits may be formed on the plated metal. This is especially a problem in sulfate electrolytes in which the surface tension typically favours bubble adhesion (Schlesinger and Paunovic, 2010). Sodium lauryl sulfate is usually used to lower the cathode surface tension to decrease hydrogen gas bubble adhesion to the cathode (Jing et al., 2010; Kittelty, 2002).

It is thus necessary to reduce the tendency and kinetics of hydrogen ion reduction relative to that of nickel reduction to enable economic electrowinning of nickel. This is typically done by decreasing the hydrogen ion concentration, i.e., by increasing the

pH of the electrolyte. However, this can only be done to a limited extent because nickel hydroxide and basic nickel sulfates will precipitate out at higher pH values, as indicated in Figure 2.2. The limiting pH value is further reduced if it is considered that hydrogen ion reduction together with mass transfer limitations may result in a significant increase of the pH next to the electrode relative to that in the bulk of the solution that may cause localised precipitation of hydroxides at the electrode surface. This effect may be countered by adding a buffer, such as boric acid, to the electrolyte, as is typically done in practice. Tilak et al. (1977) suggested that the buffering action may be by a nickel borate complex ($Ni(H_2BO_3)_2$) that would act at lower pH values. When adding boric acid to a nickel sulfate electrolyte, the nickel borate that forms promotes the release of hydrogen ions for pH stabilization (Jing et al., 2010). The buffering action of the boric acid should function at a pH close to 4 (Hinz et al., 2015) if it is in the form of $H_2B_4O_7$. Sodium is one of the elements usually present in an aqueous system and forms borax ($Na_2B_4O7.10H_2O$) in presence of boric acid. The system borax-boric acid is actually complex, with ten different equilibrium reactions in solution (Trejo et al., 2012); however, dihydrogen tetraborate (pKa = 5), monohydrogen tetraborate ion (pKa = 9) and tetraborate ion are actually the primary species in this system (Thorsten, 2013). Many other species (e.g., $B_3O_3(OH)_4^-$, $B(OH)_4^-$) are present at lower concentrations. Figure 2.3 illustrates a typical distribution diagram when considering only the main species in this system with a buffer action around pH 4 and an increase in $HB_4O_7^-$ from pH 5.

Table 2.4. Hydrogen discharge overpotentials on different cathode materials from 1 M sulphuric acid saturated with boric acid (Lupi et al., 2006).

Cathode material	Hydrogen overpotential (V)
Pt	– 0.121
Ni	– 0.253
AISI 316L	– 0.361
Al	– 0.668
Ti	– 0.688

Boric acid also acts as an inhibitor for nickel electrodeposition by shifting the deposition potentials to more negative values, probably by adsorption at the cathode surface (Supicova et al., 2006; Zech and Landolt, 2000; Yin and Lin, 1996). Moreover,

boric acid extends the useful current density range for nickel deposition and improves the morphology and appearance of the deposit, which usually becomes brighter and less brittle in its presence (Davalos et al., 2013).

In this work, boric acid was used mainly to maintain the pH around the initial pH of 3.5, typically used for nickel electrowinning from sulfate solutions. This value is somewhat lower than the pH at which the hydroxides of nickel, cobalt and copper would form but close to that at with chromium oxide and aluminium hydroxide would form, as illustrated by the series of E-pH diagrams shown as Figures 2.4 to 2.7. The precipitation pH values would be higher for lower concentrations of the metal species in electrolytes, i.e. 10^{-3} to 10^{-6}M, than those for higher concentrations, i.e, 10^{-1} M.

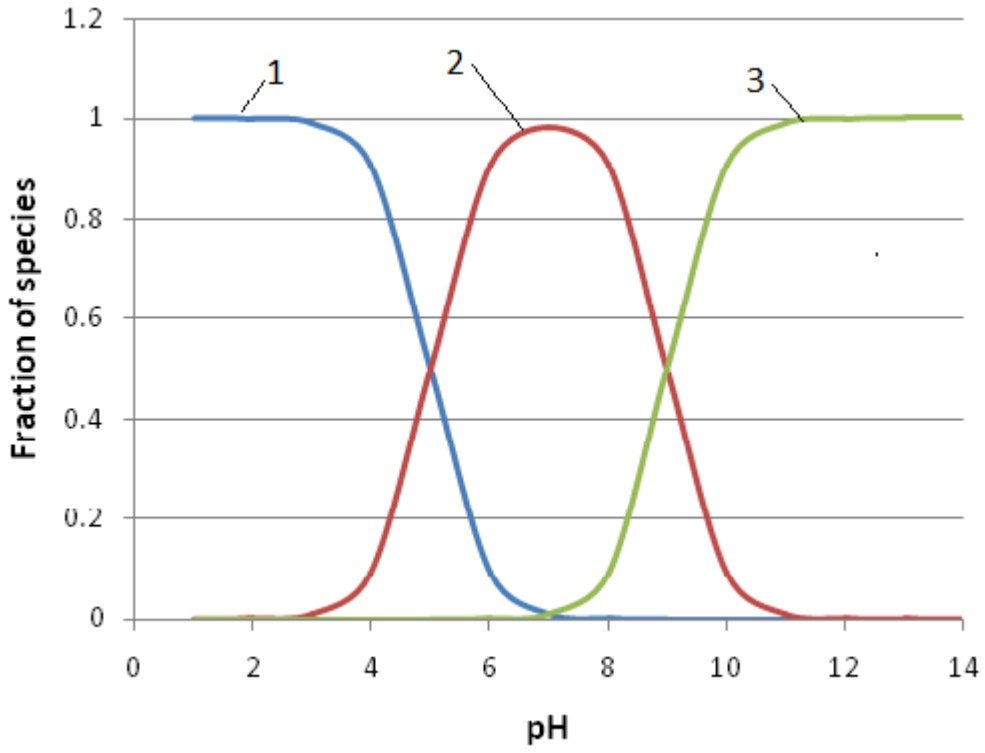

Figure 2.3. Distribution vs pH diagram of aqueous boron (III) species: $H_2B_4O_7$ (1), $HB_4O_7^-$ (2) and $B_4O_7^{2-}$ (3) (Thorsten, 2013).

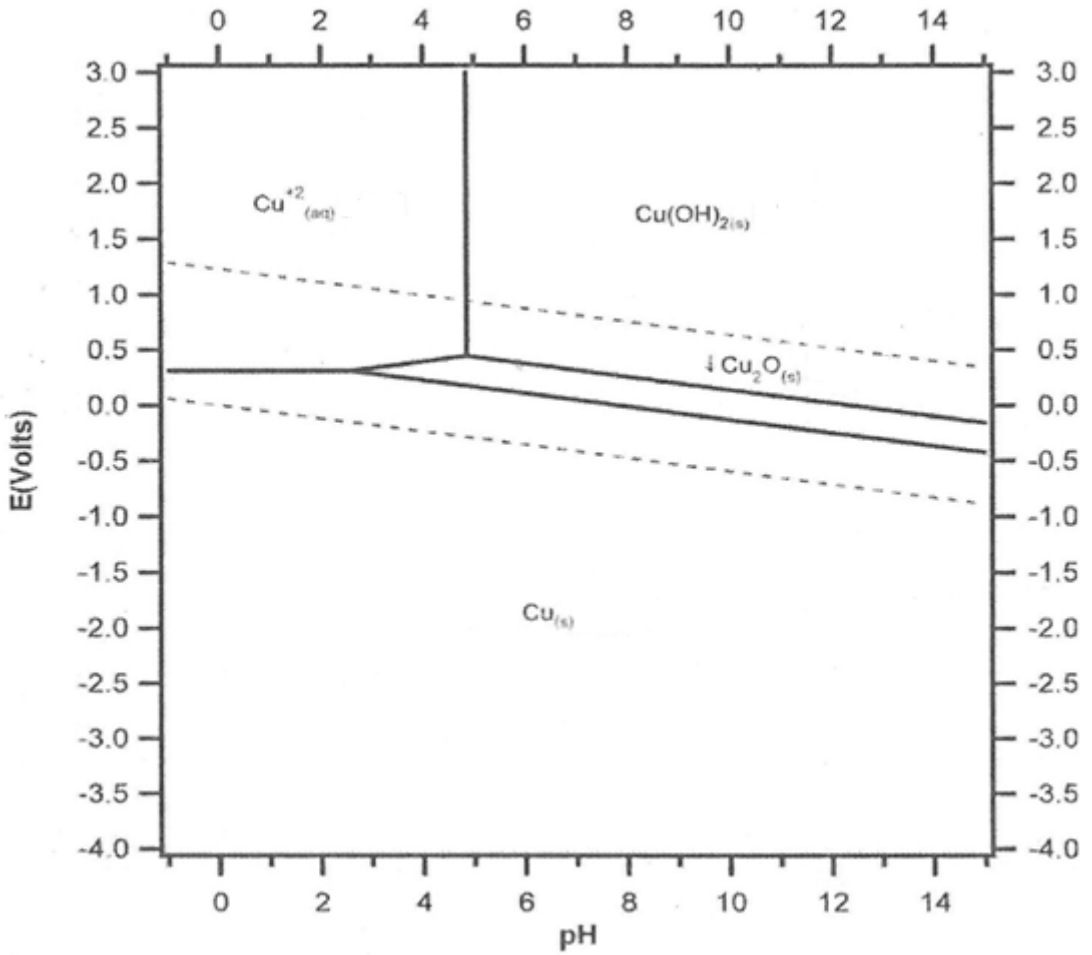

Figure 2.4 E-pH diagram of Cu-H_2O system at 25°C and 10^{-1} M for soluble species. ΔG^o in kJ/mol: Cu (0.0), $Cu(OH)_2$ (-359.0), Cu_2O (-147.7), Cu^{2+} (65.7), Cu^+ (49.8), $HCuO_2^-$ (-264.4), H_2O (-237.2), H^+ (0.0), OH^- (-157.3) (Schweitzer and Pesterfield, 2010).

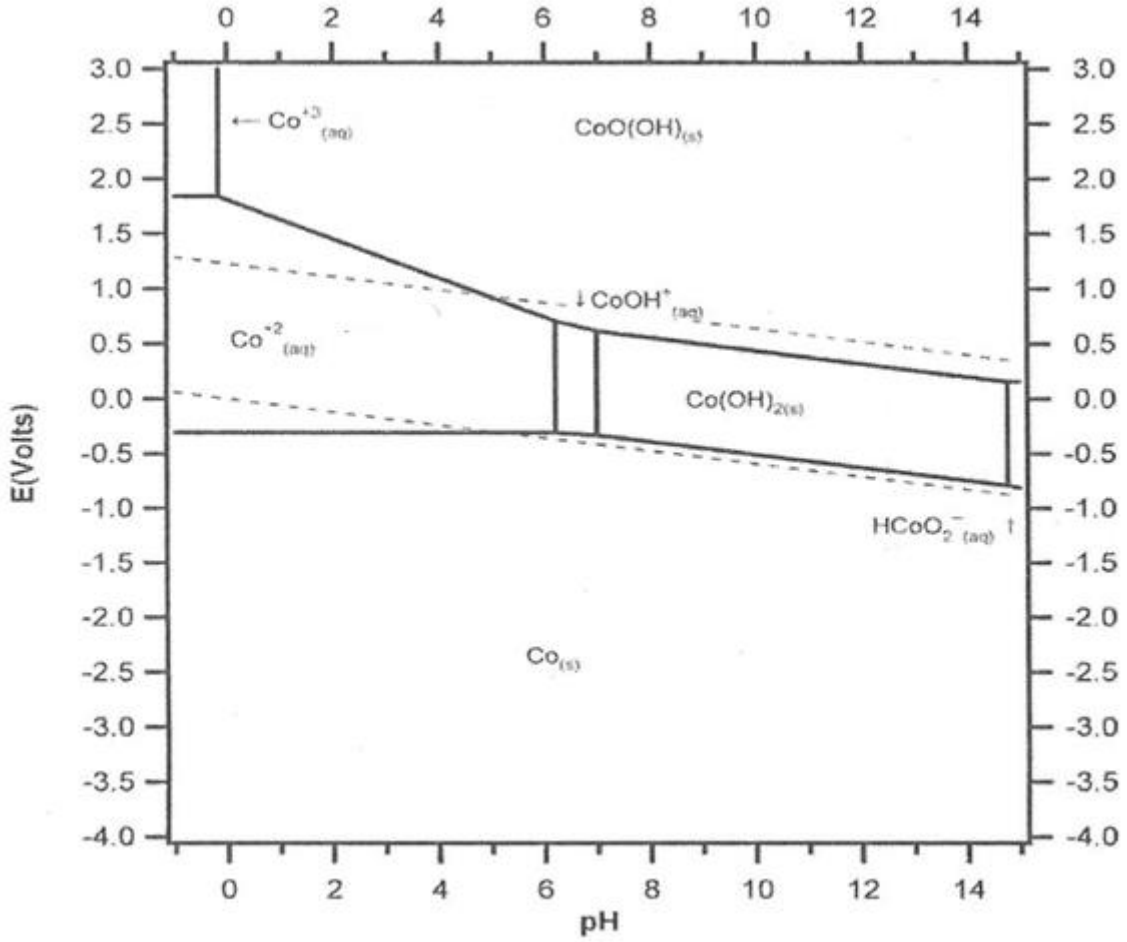

Figure 2.5. E-pH diagram of Co-H_2O system at 25°C and 10^{-1} M for soluble species.
ΔG^o in kJ/mol: Co (0.0), Co^{2+} (-53.6), Co^{3+} (+123.8), $Co(OH)_2$ (-458.1), CoO(OH) (-359.0), $CoOH^+$ (-255.2), $HCoO_2^-$ (-368.2), H_2O (-237.2), H^+ (0.0), OH^- (-157.3) (Schweitzer and Pesterfield , 2010).

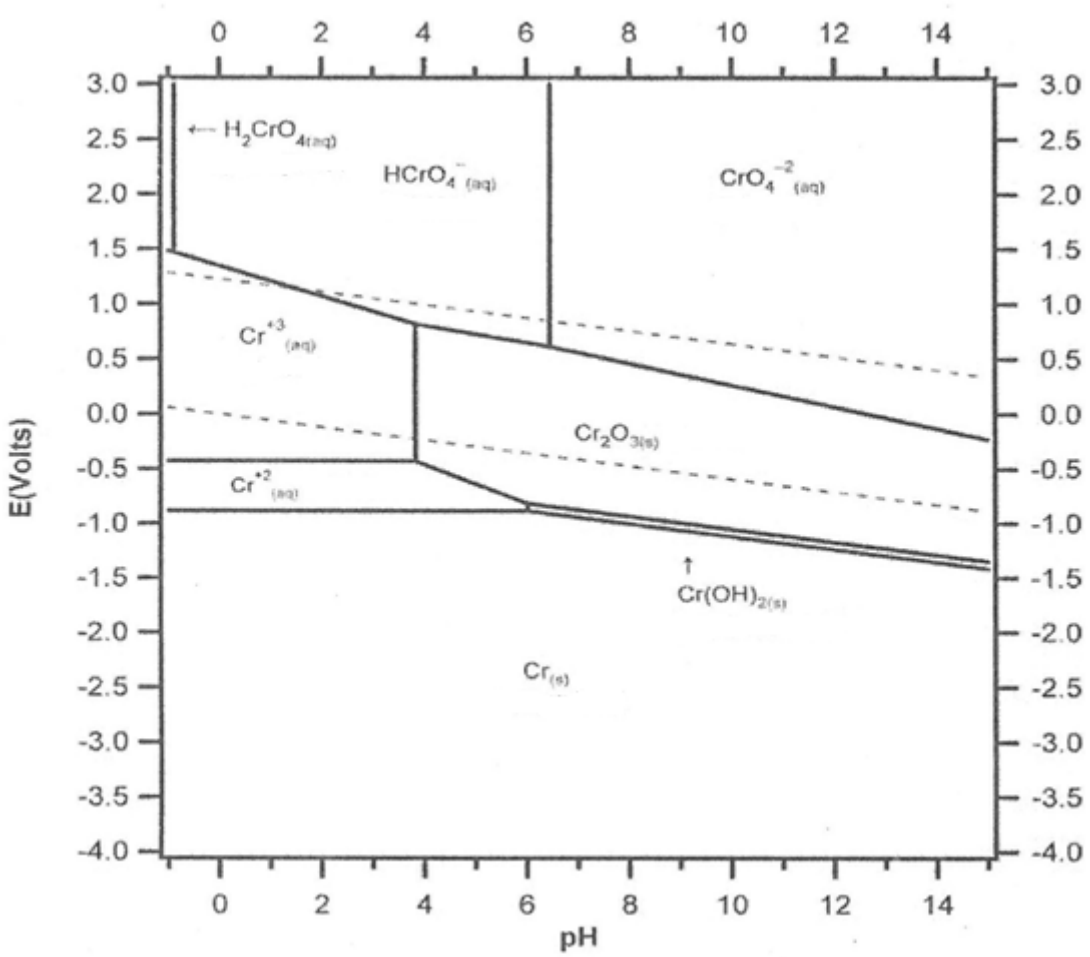

Figure 2.6. E-pH diagram of Cr-H_2O system at 25°C and 10^{-1} M for soluble species. **ΔG^o in kJ/mol: Cr (0.0), Cr^{2+} (-164.9), Cr^{3+} (-206.3), Cr_2O_3 (-1004.2), $Cr(OH)_2$ (-576.1), CrO_4^{-2} (-728.0), $HCrO_4^-$ (-764.8), H_2CrO_4 (-759.8), H_2O (-237.2), H^+ (0.0), OH^- (-157.3), (Schweitzer and Pesterfield , 2010).**

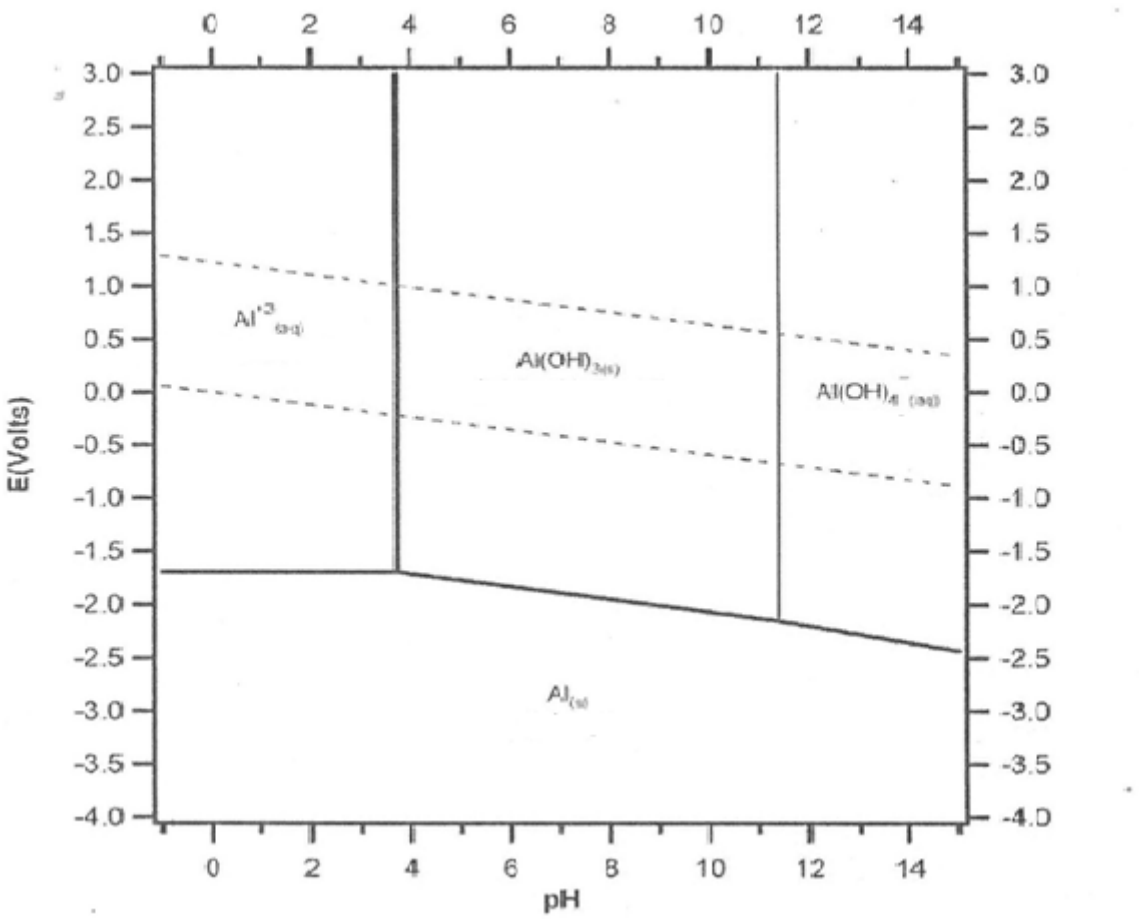

Figure 2.7. E-pH diagram of Al-H_2O system at 25°C and 10^{-1} M for soluble species.
ΔG^o in kJ/mol: Al (0.0), Al^{3+} (-485.3), $Al(OH)_3$ (-1138.9), $Al(OH)_4^-$ (-1305.4), H_2O (-237.2), H^+ (0.0), OH^- (-157.3) (Schweitzer and Pesterfield , 2010).

2.2.1.2.8 Electrocrystallisation process

Electrocrystallisation is a series of atomic-scale processes occurring from ion reduction in the vicinity of electrode to metal deposit formation. It includes two main processes, namely, nucleation and growth. During growth processes, metastable groups of atoms (clusters) form on the substrate surface and grow. More and more atoms of relatively high energy join the cluster to reduce their surface energy, while the cluster becomes more stable, until the cluster is large enough at critical size with enough mass-to-surface ratio, to grow into larger clusters or nuclei. The concurrent formation and growth of nuclei will depend on the driving force applied and the micro-environment surrounding these. The competition between nucleation and growth determines the grain characteristics of the deposit, i.e., size and orientations. The challenge is typically to maintain high nucleation and growth rates

simultaneously to achieve fine crystals at a high rate of metal plating (Anderson and Cubilas, 2010). Faces of the crystal grow with different orientations and bright deposits, are for instance, obtained when large crystal faces develop parallel to the substrate. The structure of the deposit also depends on the growth rate of the crystal in a given direction. Fibrous or laminar structures are typically obtained when crystals grow at a relatively high rate in perpendicular or parallel directions relative to the substrate, respectively. Deposit characteristics, such as structure, brightness, hardness, stress, etc., are thus strongly dependent on the initial stage of electrocrystallisation, which, in turn, depends on the atomic structure, the homogeneity of the substrate and the electrodeposition parameters. On foreign substrates, the electrocrystallisation process is significantly influenced by the electrode overpotential, the crystallographic metal-substrate misfit and the metal-substrate interaction (Astley, 1968; Jovicevic and Bewick, 2005). Different types of layer growth can occur, depending on the deposition conditions. Usually growth occurs either layer by layer, or as a three-dimenisional (3D) structure or as a mixture of the two. Defects, such as voids, can form in the two last cases when the rate of atom deposition at the bottom of the trench is lower than that occurring on the surface of previous surface layers (Dong et al., 1998; Huerta Garrido, 2007).

Basic steps of electrocrystallisation process includes a transfer or deposition of a aqua- or complexed metal ion as an adion to the surface site, i.e., crevice, plane surface, edge, hole, coner, followed by the diffusion of the adion across the surface to a growing edge. These steps of transfer and diffusion that are accompanied with more dehydration or desorption may occur continuously into a kink or vacancy where the adion coordinate with other adions while dehydration process continue, until it fully coordinates with other ions and electrons and become part of the metal incorporated in the lattice. A simplified schematic representation of electrocrystallisation processes is shown in Figure 2.8.

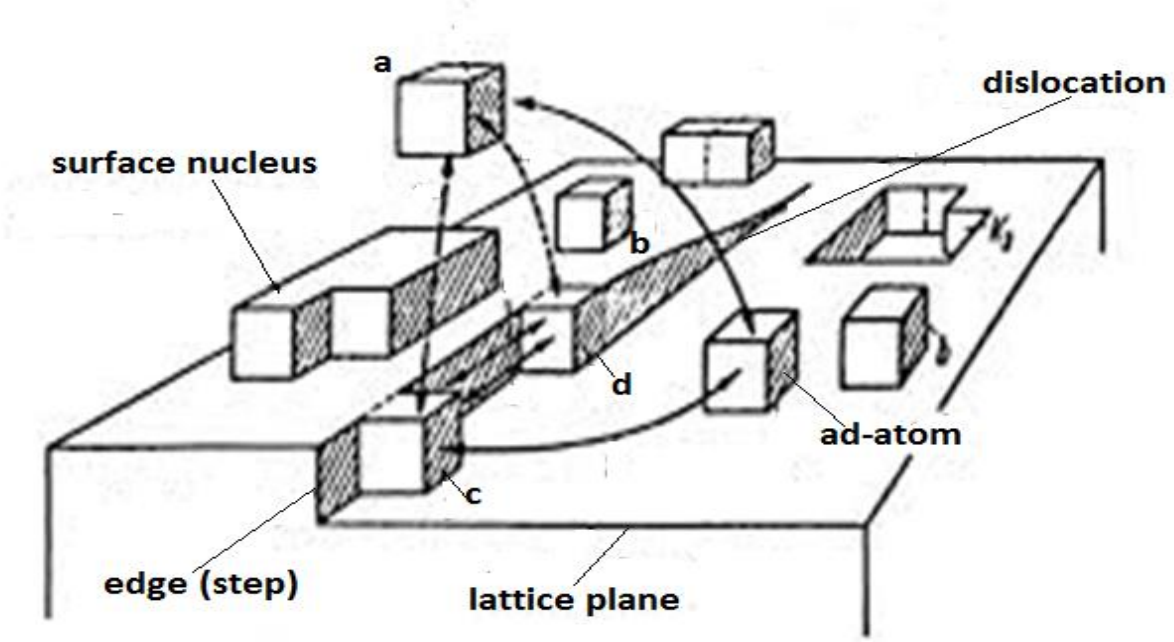

Figure 2.8. Schematic of an electrocrystallisation process showing different atom positions: other phase i.e., electrolyte, gas, melt (a), in the lattice plane (b), edge (step) site (c), growth (kink) site (d) (Schwartz, 1994).

2.2.1.2.9 Behaviour of metallic impurities present in the electrolyte during electrodeposition

Impurities present in the electrolyte may be taken up in the nickel deposit by either codeposition with the base metal or through occlusion of the electrolyte retained on the surface of the metal, especially when deposits are not smooth, or incorporated into the deposit as a solid precipitate, e.g., hydroxides that precipitate at the high pH conditions that may develop on the surface of the electrode. Impurities can co-deposit with nickel during electrowinning either through normal deposition when the impurity is more noble than nickel, in which case the ratio of the nickel and the impurity in the deposit will be proportional to their ratio in the electrolyte, or through anomalous co-deposition when the impurity is less noble than the nickel basic metal, in which case the plating of the impurity is favoured or that of nickel inhibited such that the ratio of nickel/impurity is significantly lower in the deposit than in the electrolyte. Impurities can also co-deposit by an underpotential mechanism due to the attraction between dissimilar metals. In nickel electrowinning, copper and cobalt have been found to co-deposit by normal and anomalous co-deposition, respectively (Fan and Piron, 1996; Panda, 2003), and aluminium and chromium probably through an underpotential deposition mechanism (Das and Gogia, 1988; O'Keefe and Holm, 2000). Low concentrations of some impurities in the

electrolyte can thus lead to relatively higher impurity to base metal ratios in the deposit compared with their ratios in the electrolyte, especially during anomalous codeposition or high-rate normal codeposition. In such cases, the levels of impurities in the electrolyte should be kept very low; this usually poses significant challenges in terms of purification of leach solutions. Typical allowable impurity levels found in the literature for good nickel deposit morphology are indicated in Table 2.5.

Table 2.5. Allowable impurity concentrations in the electrolyte for smooth and compact nickel deposits from sulfate electrolytes.

Impurity	**Range**	**References**
Copper	40 – 100 mg/L	Das and Gogia, 1991.
Cobalt	≈ 500 mg/L	Das and Gogia, 1991.
Chromium	5 – 10 mg/L	O'Keefe and Holm, 2000.
Aluminium	5 – 10 mg/L	O'Keefe and Holm, 2000; Das and Gogia, 1988; Mohanty et al., 2005.

Impurities report in the deposit by entrainment and occlusion of solids as well, when they precipitate at the electrode surface, as indicated earlier. This often occurs when the operating pH is higher than that required for precipitation of the impurity or the pH in the vicinity of the cathode is not controlled and may rise up to the impurity precipitation pH. It can be expected that the pH on the surface of cathodes in unbuffered sulfate electrolytes may increase by several pH units, in the neutral pH range, due to hydrogen ion reduction. This is illustrated by the overall reaction in Equation 2.14, resulting from the main cathodic reactions presented in Table 2.3.

$$Ni^{2+} + H_3O^+ + 3e^- \text{ ---------> } Ni^0 + ½\ H_2 + H_2O \qquad (2.14)$$

2.2.1.2.10 Electrowinning cell design

The cell for nickel electrowinning from sulfate electrolytes is usually a divided rectangular tank made from concrete and lined with an acid-resistant material to

contain the electrolyte. The cathodes and anodes are located parallel to each other at a fixed interelectrode pitch of typically 100 mm and immersed in the electrolyte. Cathodes may be in the form of nickel starter sheets that are typically plated on titanium cathode blanks up to a thickness of 1 mm in a separate cell and stripped from the blank to be used in the electrowinning cell as cathode substrate. More recently, permanent titanium cathodes have been introduced at some plants such as the Rustenburg Base Metal Refinery (Crundwell et al., 2011). Nickel plated on titanium typically develops higher internal stresses compared with that on nickel starter sheets but this offers some advantages in terms the of number of operating sequences in the tank house, which are reduced to only plating on the titanium cathode, harvesting from the cell, washing and stripping the nickel deposit from the titanium substrate, instead of the additional sequence relative to the starter sheet preparation. Small holes may also be drilled through the substrate so that when filled with nickel deposit, they hold the two sides of the plated nickel together to prevent disbonding of the nickel from the titanium. Cathodes are also typically fitted with plastic edges and bottom strips to permit easy separation of the deposit after electrodeposition.

Insoluble anodes are used for nickel electrowinning from sulfate solutions (Ji, 1994). Typical anodes used are rolled or cast lead generally alloyed with elements such as antimony, strontium, calcium and tin to provide corrosion resistance and mechanical strength (Holm and O'Keefe, 2000). Lead is generally alloyed with silver and/or calcium for zinc electrowinning and with antimony or calcium, tin and silver for copper electrowinning (RSR anodes, 2017). The durability of the lead anodes in this aggressive environment is achieved by the formation of a compact and electrically conducting lead dioxide layer on the surface (Habashi, 1999). The cathode and anode compartments are separated by membranes made generally of polyester or woven terylene. The mass transfer of the hydrogen ions generated at the anode to the cathode surface is limited by the membranes, by providing a porous barrier to convection and also by allowing a hydrodynamic head to be created by maintaining the height of catholyte slightly higher, e.g., 20 — 25 mm, than that of the anolyte so that the solution flows from the cathode compartment through the membrane to the anode compartment (Brown and Mason, 1977; Pavlides, 2000).

2.2.2 Nickel electrodeposits

2.2.2.1 Characteristics of nickel metal

Nickel has a number of characteristics, of which some of interest in this work are summarised in Table 2.6.

Table 2.6. Characteristics of nickel metal (Wikipedia, 2015).

Symbol	Ni
Atomic mass	58.6934g
Density	8.908 g/cm^3
Shear modulus	76 GPa
Bulk modulus	180 GPa
Poisson's ratio	0.31
Young's modulus	200 GPa
Crystal structure	FCC
Covalent radius	124 pm
Lattice constants	352.4, 352.4, 352.4 pm
Hardness	4.0 Mohs
Thermal coefficient	13.6 x10^{-6} m/m^{o}C

FCC: Face-centred cubic

2.2.2.2 Nature and origins of internal stresses in electrodeposits

Internal stresses are caused by forces that develop in a body in the absence of any external force applied at the boundaries of the body. Internal stresses in electrodeposits originate from different sources that are usually categorised in three groups: epitaxial stresses, thermal stresses and intrinsic or internal stresses (Vlassak, 2004; Giallonardo, 2013)

Epitaxial stresses occur when a deposit of a given lattice constant and crystal structure is deposited on a substrate with either a different lattice constant and/or

crystal structure such, as in the case of electrodeposition of nickel characterised by a face-centred cubic (FCC) crystal structure with lattice constants of 352.4, 352.4 and 352.4 pm (Web element data, 2016) on a titanium substrate with a hexagonal close-packed (HCP) crystal structure characterised by lattice constants of 395.08, 395.08 and 468.55 pm. In such cases, the film formed in the earlier stage of nickel electrodeposition, for which the FCC structure is favoured, will deform in an attempt to match the HCP crystal structure of the titanium substrate. The distance between nickel atoms in this initial film should thus be different from that in the normal energetically favoured FCC nickel lattice, resulting in stress development in the initial layers. As the thickness of the film grows, the crystal structure will tend more and more to the normal favoured FCC crystal structure in the deposit and the epitaxial stress would decrease (Sander et al., 2003).

The misfit strain in such intermediate thin films is defined by the ratio of the lattice constants of both the film and the substrate, as given in Equation 2.14, where a_f and a_s are the lattice constants of the film and the substrate, respectively. The lattice constant is a characteristic of crystal structures of materials. Table 2.7 gives the relationship between the lattice constants of some common crystal structures and the atomic radii of the solids. The misfit strain is related to the corresponding misfit stress by Hooke's law, the stiffness tensor formula of which depends on the crystal plane direction of both the film and the substrate (Vlassak, 2004; Floro and Chason, 1998). However, the direction of a crystal plane is a function of many parameters in the manufacturing process of the substrate and of the electrodeposition conditions used for the metal being electrodeposited, such that the misfit strain in the very thin layer deposited at the earlier stage of electrodeposition is not easily predictable. For cubic crystals such as nickel, the stiffness tensor formula is typically expressed in terms of the only three fouth order independent elastic constants, i.e. C_{11}, C_{12}, C_{44} in contracted notation, for modulus for axial compression, modulus for dilation on compression and shear modulus, respectively (Zhao et al., 2004). Typical elastic stiffness coefficients for the stiffness tensor of nickel are shown in Table 2.8.

$$\varepsilon_m = (a_s - a_f)/a_f \qquad (2.15)$$

where a_s is the lattice constant of the substrate,

a_f is the lattice constant of the film,

ε_m is the misfit strain.

Table 2.7. Lattice constants a_o of common crystal structures as a function of atomic radius of materials (Ouyang, 2009).

Structure	a_o in terms of r	Example	Atoms per cell
SC	$a_o = 2r$	Po	1
BCC	$a_o = 4r/(3)^{1/2}$	Fe, Ti, W, Mo, Nb, Ta, K, Na, V, Zr, Cr	2
FCC	$a_o = 4r/(2)^{1/2}$	Fe, Cu, Au, Pt, Ag, Pb, Ni	4
HCP	$a_o = 2r$, $c_o = 1.633a_o$	Ti, Mg, Zn, Be, Co, Zr, Cd	2

SC: Simple cube
BCC: Body-centred cubic
FCC: Face-centred cubic
HCP: Hexagoal close-packed
a_0, c_0: Lattice constantes
r: Atomicradius

Table 2.8. Elastic stiffness coefficients for some metals, constants in 10^{11} Pa (Allard, 1969).

Metal	C_{11}	C_{12}	C_{44}
Na	0.074	0.062	0.042
Pb	0.495	0.423	0.149
Cu	1.684	1.214	0.754
Ni	2.508	1.500	1.235
Cr	3.500	0.678	1.008
Mo	4.630	1.610	1.090
W	5 .233	2.045	1.607

C_{11}, C_{12} and C_{44}: Modulus for axial compression, modulus for dilation on compression and shear modulus, respectively.

Thermal stresses may develop in electrodeposited films when the temperature dependence of the thermal expansion coefficients of the plated metal and the substrate differ. During cooling, the material with the higher thermal expansion

coefficient will try to contract but will be restrained by the lesser contraction of the material with the lower thermal expansion coefficient. Thus the former material will be under tension while the latter will be under compression. Nickel electroplating from sulfate electrolytes is carried out typically at 60°C, and when the cathodes are removed from the electrolyte and cooled to ambient temperatures, significant stresses may develop at the interface of the plated metal with the substrate.

Consider the case of a nickel film, with a relatively higher thermal coefficient α_{Ni} of 13.4 x 10^{-6} m/m.°C, deposited at around 60°C on a titanium substrate, with a lower thermal coefficient α_{Ti} of 8.6 x 10^{-6} m/m.°C (Wikipedia, 2015; Web. element data, 2016). When this cathode is cooled to an ambient temperature of around 25°C, nickel will attempt to contract more than the titanium substrate to which it is bonded, and will impose a compressive stress on the titanium while a tensile stress is developed in the nickel. In such case, the magnitude of the strains developed in the thin plated nickel layer is usually estimated using the relationship shown as Equation 2.16 (Abdulaliyev et al., 2007), from which the stresses may be calculated, assuming that Hooke's law applies, as shown in Equation 2.16:

$$\varepsilon_{th} = (\alpha_{Ni} - \alpha_{Ti}) \,.\, \Delta T \qquad (2.16)$$

and

$$\sigma_{th} = E.\ \varepsilon_{th} \qquad (2.17)$$

where α_{Ni} is the thermal expansion coefficient of nickel (m/m.°C),

α_{Ti} is the thermal expansion coefficient of titanium (m/m.°C),

ΔT is the change in temperature (°C),

ε_{th} and σ_{th} are the thermal strain and thermal stress, respectively,

E is the Young's modulus (MPa).

The strain and stress developed in a thin plated nickel layer on a titanium substrate if the temperature changes from 60 to 25°C, taking Young's modulus as 220 GPa for nickel (Wikipedia, 2015) will thus be:

$$\varepsilon_{th} = (13.4 - 8.6) \times 10^{-6}.\ (60 - 25) = 168.10^{-6} \qquad (2.18)$$

$$\sigma_{th} = E.\ \varepsilon_{th} = 200\ \text{GPa} \times 168.10^{-6} = 3.36 \times 10^{-2}\ \text{GPa} \qquad (2.19)$$

Note that this thermal stress at the interface is small (33.6 MPa) compared with the typical range of internal stresses in the bulk of nickel electrodeposits from sulfate solutions, e.g., 200 to300 MPa. Moreover, the effect of thermal stress will be highest at the interface and less in the bulk nickel constituted of identical layers with the same thermal coefficient.

A third category of internal stresses originates from the deposition and growth processes. Most of the mechanisms for stress generation in this category are based on lattice distortion in the deposit and generate a macroscopic stress state in the whole deposit. Defects or imperfections in the structure of the metal usually disrupt the perfect arrangement of the surrounding atoms and cause distortion of the lattice planes and induce intrinsic stresses. Other forms of internal stress development in this category may be explained in terms of other mechanisms, such as grain growth by coalescence, where adjacent crystals exert forces on each other, phase transformation during the ion reduction process at the cathode surface (Vlassak, 2004) or exclusion zones that may develop due to mass transfer constraints. Typical defects occurring in metal electrodeposits are illustrated in Figure 2.9.

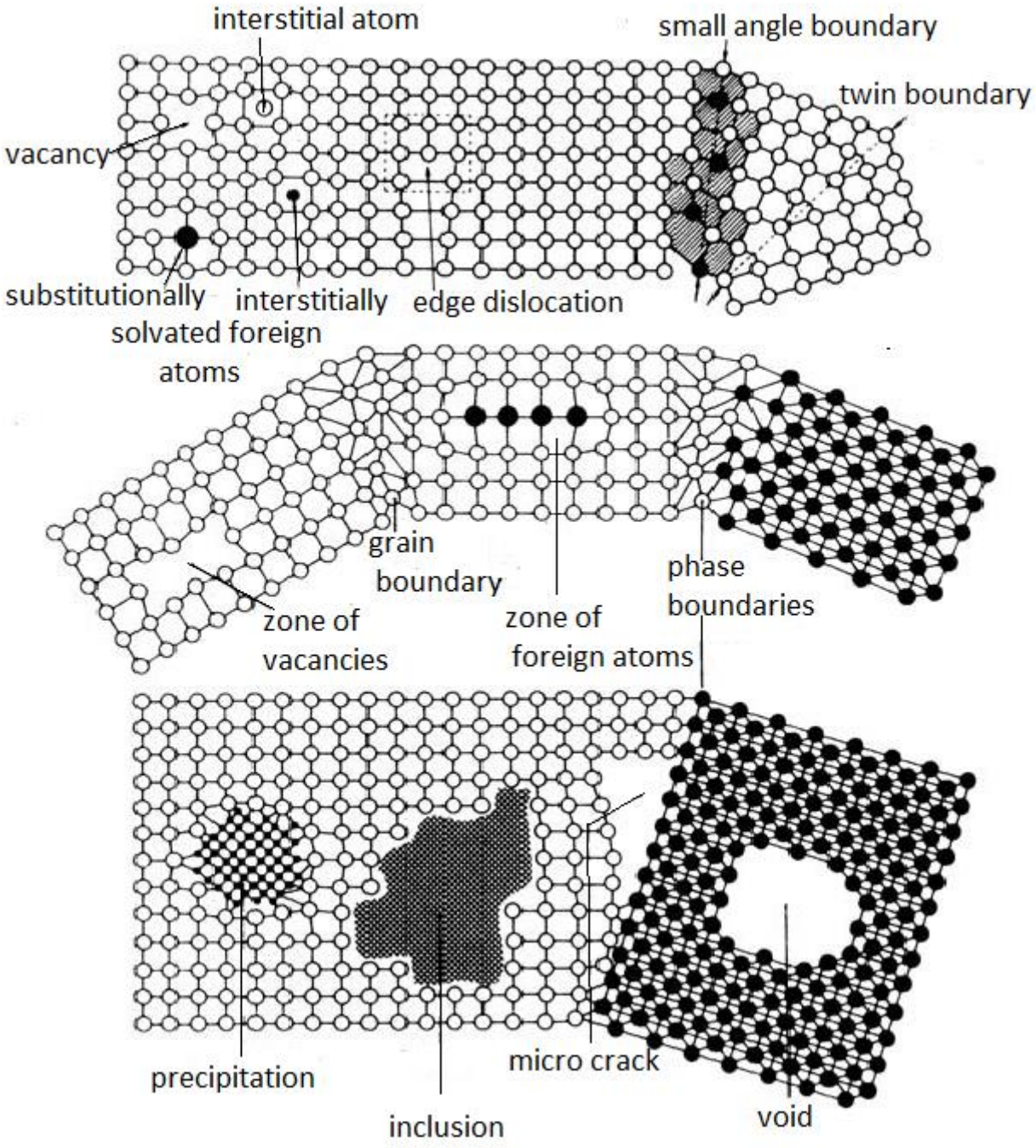

Figure 2.9. Metallic structure and defects (Giallonardo, 2013).

2.2.2.3 Mechanical properties of nickel

In the context of the present investigation, it is important to have some idea of the mechanical properties of nickel. Typical values, as low as 59 MPa for the 0.2% offset yield strength and 317 MPa for the tensile strength, respectively, were reported in Metal Handbook in the 1980 s (Davis, 2000). The relatively low mechanical properties of the nickel should be considered in the context of the physical constraints placed

on a thin plated layer on top of a substrate that may not allow deformation of the nickel even if the yield strength is exceeded, because the slip systems may not be able to operate due to the constraint by the substrate, causing the thin plated nickel to behave more like a brittle material.

However, these low values are in marked contrast to recent tensile tests carried out on pure nickel metal with relatively higher measured yield and tensile strengths (Mehregany and Roy, 1999; Dual et al., 2004). Moreover, the exact values of the relatively higher yield strength and tensile strength in a tensile test are affected by a number of parameters, such as the test strain rate, the specimen thickness (Soboyejo et al., 2003), the specimen size (Dual et al., 2004), temperature and microstructure. Typical values in the literature of recent values of the yield strength and tensile strength of pure nickel obtained under different test conditions in terms of the above parameters are given in Table 2.9 and Figure 2.10. In this work, the yield strength calculated using the grain size and the Hall-Petch relationship, as described in the section 3.3, was found to be around 250 MPa for pure nickel deposited from impurity-free electrolyte. It increased with impurities in the electrolyte, mainly by grain refinement, as can be noticed in Figures 4.3 to 4.6 in Chapter 4.

Table 2.9. Typical values of tensile properties of nickel (Davis, 2000; Soboyejo et al., 2003; Haluzan, 2004, Mehregany and Roy, 1999).

	Yield strength	Tensile strength
Metal Handbook (1979)	59	317
Jacobian et al. (1979)	410	600
Mazza et al. (1997)	405	782
Sharpe et al. (1997)	323	555
Xie et al. (2000)	400	540
Bucheit et al. (2002)	277	

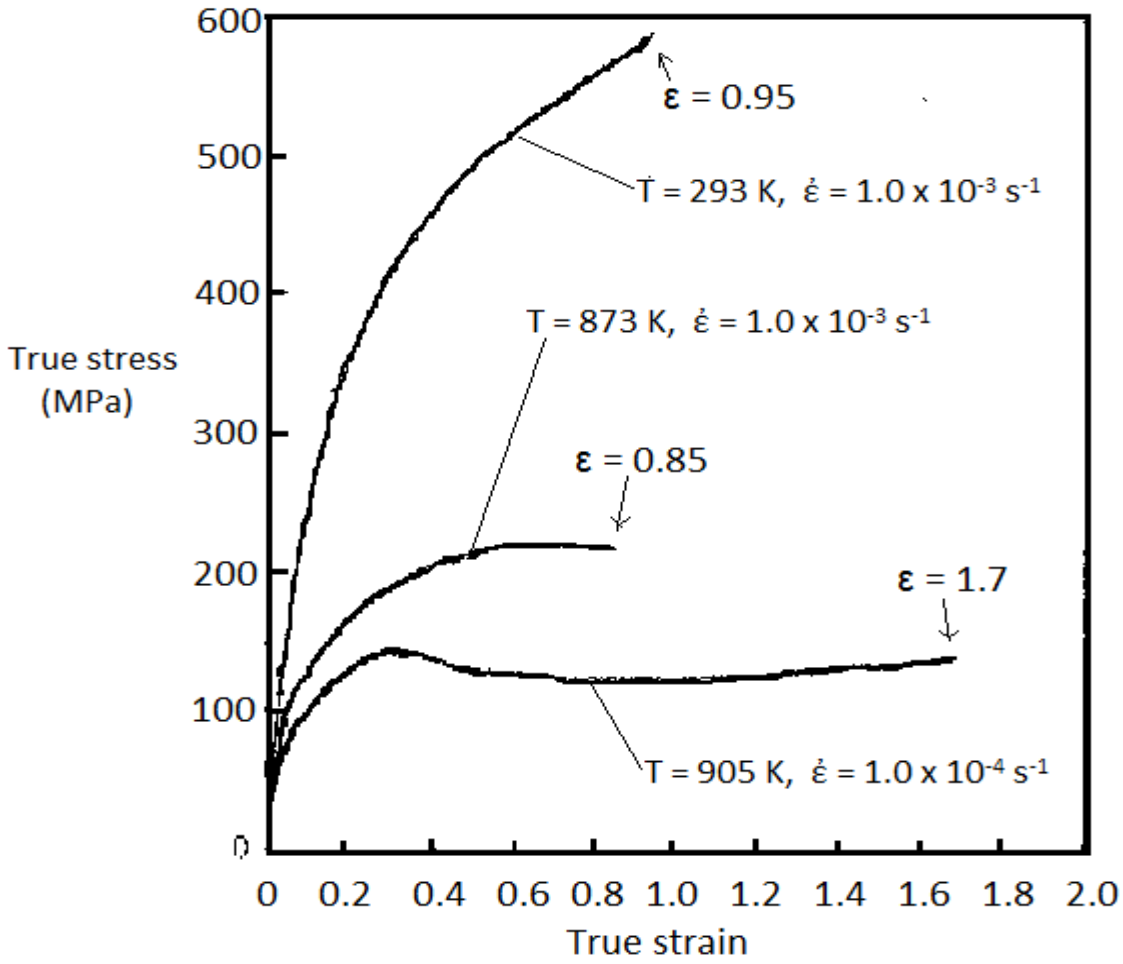

Figure 2.10. Typical true stress - true strain curve for pure nickel metal (Hesegawa and Fukutomi, 2002).

2.2.2.4 Mechanical properties of titanium

The cathode substrate used in this work was made of titanium. Its characteristics of interest for this study are the Young's modulus and Poisson's ratio used in Stoney's equation, introduced later as Equation 2.17. Typical values of these characteristics are 110 GPa and 0.28 for Young's modulus and Poisson's ratio, respectively **(Jorge et al., 2014).**

2.2.2.5 Effects of impurities on stress in electrodeposits

Impurities codeposited with the base metal usually differ in atomic radius, electronegativity, valence and crystal structure from the base metal. If an impurity with a larger radius is introduced into a crystal lattice, it would tend to be compressed but would generate local tensile stresses in the host metal to balance these forces, while the reverse would apply for a smaller radius impurity (Pruit and

Chakravartula, 2011). Impurity atoms in interstitial positions would always generate tensile stresses elsewhere in the lattice.

The lack of an atom at a particular position in the lattice, i.e., a vacancy, can also develop during a plating process if, for instance, the rate at which surface diffusion of adatoms occurs is too slow to move them from deposition sites to energetically most favoured positions on the surface. The mode of electrodeposition should change with increasing rate of plating from an orderly layer-by-layer deposition, i.e., so-called Frank van der Merwe growth, to three-dimensional growth, i.e., so-called Volmer-Weber growth (Dong et al., 1998), with a mixture of the two modes at intermediate rates. The vacancies may condense into voids or larger zones of vacancies. These may also be formed when, for instance, the deposit grows faster at the top of a trench than at the bottom.

2.2.2.6 Effect of impurities on the mechanical properties of electrodeposits

Metallic impurities affect the strength of the deposit in three ways. Impurities create more disturbed zones in terms of atom arrangement in the lattice, which reduce the size of the perfectly arranged atom areas or grains, also increasing the fraction of grain boundary area in the lattice. A relatively lesser distance between grain boundaries due to the multiplication of grain boundaries reduces the free path of dislocations in the lattice when these have to move to enable plastic deformation. A dislocation in the grain thus has a limited possibility to move in the lattice as it meets resistance at grain boundaries, the fractional area of which has been increased due to the grain size reduction (Corbett and Hoyt, 2005). A significant increase in the hardness of the material results from the grain size reduction. Impurities can also increase the hardness of the metal by a solid-solution hardening mechanism (Callister, 2007). As dislocations move in the slip planes, they meet impurity atoms codeposited in the lattice in their paths. The stress field surrounding impurity atoms can interact with the stress field surrounding dislocations and stop the dislocation motion and increase the stress required to deform the material plastically (Kelly et al., 1971). The dislocation density in the material is increased by impurities as well, as these can cause, for instance, more edge dislocations, stopping a sequence of base metal atoms. Stress fields of dislocations can interact between themselves and increase the metal hardness when the dislocation density increases significantly by the so-called work hardening mechanism. However, at very high dislocation densities, the range of which depends on the material, a decrease in hardening is

observed (Kubin and Devincre, 2000). The limitation of dislocation motion in the ductile material may cause some kind of brittle characteristics with fracture around the yield stress.

Microstructures such as grain boundaries or inclusions can also increase the material toughness as they interact with cracks or other flaws and stop or slow down their propagation. This usually occurs in brittle materials.

2.2.2.7 Constrained electrodeposits

Nickel is known as a ductile material that deforms plastically when an externally applied stress exceeds the yield stress in a tensile test. Relatively significant atomic displacement with an increase in interatomic bonds occurs before the yield stress is reached, where the minimum required shear stress in the slip planes to initiate slip (dislocation motions) is reached and from this point the specimen does not return to its original size or shape when unloaded. As a metal, it also usually contains defects other than dislocations, i.e., micro-cracks, voids and zones of vacancies, as shown in Figure 2.9.

When the possibility of extension under increased stress is limited, such as in the case of internally stressed nickel deposit constrained by the substrate during plating, relatively high stresses can develop in the deposit with almost no elongation and atomic displacement, making the deposit behave as a brittle material (Cree et al., 2006). Under these conditions, the energy related to the stress is usually released through the propagation of flaws, such as micro-cracks or similar defects such as voids or zones of vacancies, usually tending to fail in the form of delamination, peeling or cracking of the deposit, depending on the extent, location and direction of the propagation. This would occur because stressed materials always tend to relax to remain in their lowest energy state.

When plated on a relatively flexible substrate, the potential strain energy, the only energy source in the deposit-substrate system, is usually released through bending of the substrate that requires work to be done, with small deflections for relatively stiff substrates. The higher the substrate stiffness, the higher the energy required for the bending. For small deflections, because atoms are only slightly displaced (not to the extent of the atomic cohesive strength in a tensile test, for instance, where the critical shear stress in the slip planes is reached), atoms can still potentially move apart with the possibility to return to initial positions. The bulk of the deposit thus

remains in the elastic domain. In this way, the deflection of the relatively stiff but flexible substrate may be used to calculate the stress in the thin film that caused the substrate bending, using formulae available in the literature developed on basis of deformation in the elastic domain, provided that the deflections are small.

If the potential energy developed in a film is released in the form of the work required to bend the substrate, it is likely that the deposit is almost free of potential strain energy and not stressed enough for significant microcrack growth to occur, so that the types of failures mentioned above are usually not visually observed. Moreover, the bending of the substrate induces, in return, a bending stress field (tensor) in the deposit that can obviously interact with the possible very low remaining stress field of the primary field, i.e., the stress due to impurities, to prevent micro-crack propagation so that the deposit surface appears visually smooth.

2.2.2.8 Brittle fracture mechanism and fracture criteria

Microcracks already existing in electrodeposits will grow when the stress in the deposit is high enough, typically during electrodeposition on stiff substrates where the elongation of the deposit is constrained. It is known that, in a crack-containing material, the stress is not uniformly distributed. The stress is more concentrated at crack tips than in the bulk (Callister, 2007). The stress distribution around the crack tip may be expressed in terms of a stress intensity factor, the value of which depends on the shape and size of the tip, the rate of application and level of the applied stress. Cracks, even of very small length, can start to grow when the critical stress, as defined by Griffith's equation, develops in the material so that, in practice, using fracture mechanics concepts it is possible to determine whether a crack of given length in the material with known toughness will propagate at a given stress level. Very short cracks, i.e., micro-cracks, usually start to grow slowly in the so-called Stage I growth, with the slip planes usually making an angle of 45^{o} with the applied stress in tensile tests. As the micro-cracks grow the stress intensity factor at the crack tips increases and reaches to a level for the rapid Stage II growth, where the relatively high stress intensity factor at the crack tips creates local plastic zones where atoms are usually disordered and dislocations are emitted from the tips in these plastic zones to relax the high stress at the tips (Totten, 2008). Usually crack growth in Stage II occurs by cleavage, i.e., breaking of atomic bonds along specific planes. As the crack tips approach grain boundaries, they usually blunt and their opening become wider and wider while the grain boundary glides. In this case, as the crack radius increases

with blunting, the stress intensity factor significantly decreases and the crack propagation stops at the grain boundary. The tip stress can also be high enough, typically when there is some additional induced stress, i.e., phase transformation-induced stresses, or more applied stress, so that the crack can pass into the next grain with or without gliding of the grain boundary (Hong-Xian et al., 2013). Other microstructural barriers such as inclusions or pearlitic zones, can also stop Stage II growth (Ritchie, 1999). Impurities in the electrodeposits can play both the roles of microstructural barrier and stress inducer. When the stress intensity factor at the crack tip increases for some reason, e.g., crack length increment, tip radius decrement, increased applied or induced stress, and reach the critical stress intensity factor or fracture toughness, i.e., the resistance to fracture, crack propagation become unstable and proceeds continuously. This is Stage III crack growth that leads to failure. The stress intensity factor is thus a parameter used for predictions of crack growth and fracture at a microscopic level.

Fracture criteria can also be expressed in terms of an energy approach, where the driving force for crack propagation, i.e., the energy release rate, should exceed the sum of the energy required to create new crack surfaces and local plastic zones at crack tips. In practice fracture in brittle materials is experimentally observed and macroscopically predicted at that moment the overall stress in the material reaches the yield stress. The model of crack initiation in BCC metals, introduced by Cottrell (Pokluda and Sandera, 2010), can be extended to other structures, and applied also at the microscopic level for brittle fracture with limited plastic zones at crack tips. This can be done considering that the work done by the force acting in front of a number of dislocations along the distance of the Burgers vector equals the energy required for the creation of new crack surfaces and assuming the relation connecting the number of dislocations with the grain size in terms of the Hall-Petch relationship. The cracking mechanism in a ductile but constrained nickel deposit is thus likely to be a brittle fracture with little plastic deformation occurring at the crack tip.

2.3 Methods to assess internal stress

2.3.1 Stress measurements in deposited films

There are many methods for the measurement of stresses in thin electrodeposited films. These may be categorised as destructive methods, such as hole-drilling, deep hole and sectioning techniques, non-destructive methods, such as curvature-based,

ultrasonic and Barkhausen noise methods, or diffraction based techniques, such as the X-ray diffraction or neutron diffraction methods (Rossini et al., 2012; Withers and Bhadeshia, 2001; Ivetic et al., 2009). However, in-situ stress measurement in electrochemical cells presents some challenges. Typically, the use of strain gauges for stress measurement is more practical when the gauge is not immersed in a solution because an electrical circuit is involved. Either the gauge has to be placed on the non-immersed part of the substrate, with relatively less accurate measurement of the deflection, or it has to be placed on the immersed part of the substrate with adequate electric isolation to avoid the risk of short-circuiting. In the latter, case significant resistance to the bending may be introduced which could significantly affect accuracy considering the small range of deflection expected. Alternatively, the shear strain in the deposit may be measured because this was found to be approximately equal to the ratio between the deflection and the length of the cathode (Kittelty, 2002), from which the shear stress can be calculated using Hooke's law. In this case, knowledge of accurate elastic properties of the thin film obtained is required for the stress calculation, which is not easy to determine with high confidence. X-ray diffraction is also typically used for stress measurement in thin films, but is not applicable for in-situ stress measurements and also requires the elastic properties of the thin film. In this work, a curvature-based method was used for stress measurement in the nickel deposits.

2.3.1.1 Curvature-based methods

Curvature-based methods are widely used for internal stress measurements of electrodeposited thin films. They are based on the determination of the deflection of the substrate that occurs when deposition takes place only on one side of the substrate due to internal stress development in the deposit. Usually, either optical or mechanical methods are used for the measurement of either the deflection or the curvature, which is, in turn, used for the calculation of the internal stress using Stoney's equation (Freund and Suresh, 2005). An optical method may consist of measuring the change in relative spacing between two parallel incident laser beams reflecting off the substrate that has been curved due to the stress developed in the deposit layer deposited on one side of the substrate. The spacing of the reflected beams is measured using a charged-coupled device (CCD) camera and is related to the substrate curvature change, which is directly converted into stress using Stoney's equation (Sethuraman et al., 2013; Pharr et al., 2013; Chason, 2013). The reflected

beams would have the same spacing as that of the incident pair of beams if the substrate remained flat with zero curvature change. The inconvenience of this method when using an electrochemial cell is the fact that the beams have to cross some interfaces and media, such as the electrolyte and the wall of the electrochemical cell, before reflecting off the sample. In this case, some careful corrections in the use of the Stoney's equation relative to the deviation of the beam directions in the aqueous medium and the cell body should be taken into account (Overmeere et al., 2010) which is sometimes not easy to handle. The most used mechanical method for the determination of curvature for the calculation of internal stress via Stoney's equation involves a stylus that scans the back surface of a circular substrate along the radial direction by making physical contact with it. The out-of-plane displacement, as a function of the distance that the stylus has run from some reference point, is then converted to curvature or curvature radius (Freund and Suresh, 2005; Miyazaki et al., 2009). In this work, a mechanical method for the deflection measurement using a displacement sensor was used for internal stress measurement.

2.3.1.2 Stoney's equation and its limits

Stoney's equation, described in Equations 2.20 and 2.21 (Rosakis et al., 2006; Sander et al., 1995), is applicable for internal stress calculations for small deflections. This equation is widely used for curvature-based stress measurement in thin films on substrates. One of the advantages in using this equation is the fact that it does not require knowledge of the mechanical properties of the film, such as Young's modulus and Poisson's ratio, but rather only those of the substrate. It is mainly derived either through mechanical equilibrium approaches, where the net internal forces and bending moments are assumed to be zero, such as those developed by Hoffman, or by an equivalent elastic energy minimization approach, as developed by Flinn (Auciello and Krauss, 2001; Floro and Chason, 1998). It is only applicable for stresses in the elastic domain of materials because Hooke's law is used in these developments. Many other ways to derive this equation have been reported in the literature. They are all based on the idea that for a film that is much thinner than the substrate, the film is essentially unmodified by the compliance and bending of the substrate at small deflections. The boundary conditions stated in the literature for the accurate use of the Stoney equation are (Freund and Suresh, 2005):

1. The film thickness must be far less than that of the substrate (typically less than one tenth) so that the neutral axis with zero strain when the compound beam bends remains almost at the middle of the substrate thickness.

2. The deflection must be small so that the film is almost unmodified or remains in the elastic domain.

3. The substrate must be initially flat so that the initial deflection is zero.

4. An equi-biaxial stress state is assumed in the film.

The stress in a thin film (σ) on a thicker substrate may be described in terms of the curvature of the composite in terms of Stoney's equation:

$$\sigma = \frac{Es\ K}{6(1-\nu)}\frac{1}{tf}\ ts^2 \qquad (2.20)$$

$$\text{with}\quad K = \frac{2\delta}{ls} = \frac{1}{R} \qquad (2.21)$$

where ts is the substrate thickness (m),
tf is the film thickness (m),
Es is the substrate elastic modulus (MPa),
ν is the substrate Poisson's ratio,
ls is the substrate length (m),
K is the curvature (1/m),
δ is the deflection (m),
R is the curvature radius (m).

2.3.2 Determination of the mechanical properties of the deposit

The mechanical properties of the nickel deposits have been estimated through the determination of the yield stress. Typically, the yield stress of a material is determined by the sum of different components, such as those due to the change in grain size and solid strengthening. The yield stress component related to the change in average grain size is usually calculated using the Hall-Petch relationship that correlates the yield stress to the average grain size and intrinsic yield stress, as given in Equation 2.22 (Shaw et al., 2004; Morris, 2010), indicating that the yield strength of the material increases with decreasing grain size.

$$\sigma_y = \sigma_o + k/d^{1/2} \qquad (2.22)$$

where σ_y is the yield stress (MPa),

σ_o is the intrinsic yield stress (MPa),

k is a constant characteristic of the material (MPa$\sqrt{m}$),

d is the average grain size (m).

This relationship has been shown to apply for many metals for typical grain sizes (Armstrong, 2014; Shaw et al., 2004; Murakami et al., 2008). However, the relationship does not hold in the nanoscale range where the so-called reverse Hall-Petch relationship is observed. In this range of grain size, the material hardness rather decreases with decreasing grain size (Carlton and Ferreira, 2007; Mittal, 2009). Each metal has its own breakthrough at which the trend of hardness reverses with decreasing grain size. For most metals, including nickel, the breakthrough is around 20 nm, which is far lower than the range of grain size of more than 100 nm usually obtained for electroplated nickel. The slope of Hall-Petch line, i.e. k in equation 2.22, generally depends on the nature of the alloying element.

The average grain size is usually determined by the intercept method from surface images taken by SEM (scanning electron microscopy). Electroplated metals generally present a wide range of grain sizes with different grain sizes found for different regions of the same sample. In addition, the number of intercepts in the same region can vary with the direction of the intercept line. Thus, the average grain size of a region has to be obtained by considering different directions for the intercept line. A reasonable average grain size of the sample can be given by considering the average grain size of many different regions chosen on the deposit surface. The average size d for a given direction of intercept line is calculated using the intercept formula:

$$d = L / (M.N) \qquad (2.23)$$

where d is the average grain size (m),

L is the length of the intercept line (m),

M is the magnification of the image,

N is the number of intercepts.

The solid strengthening component of the yield stress due to impurities may be estimated by considering the interaction force between the solute atoms and dislocations, as developed by Cottrell. The increase in shear stress in a crystal, according to Friedel's theory for low solute concentrations, and the increase in yield stress due to solid strengthening in a polycrystalline solid when introducing a Taylor factor, is given by Equations 2.24 to 2.26 (Higashi and Uesugi, 2010; Yan, 2012; Proville and Patinet, 2008). This relationship indicates that the contribution to the yield stress due to the solid strengthening is proportional to the square root of the concentration of the impurity and a power of the absolute value of the misfit strain.

$$\sigma_s = 3G.b.C^{1/2}.\varepsilon^{2/3} \quad (2.24)$$

$$\text{with } b = \sqrt{2}.a/2 \text{ (for FCC materials)} \quad (2.25)$$

$$a = 2.\sqrt{2}.r \quad (2.26)$$

where G is the shear modulus (MPa),

b is the Burgers vector length (nm),

C is the impurity concentration (at %),

ε is the strain misfit,

r is the atomic radius (nm),

a is the lattice parameter (nm),

σ_s is the yield stress considering solid-solution hardening (MPa).

2.3.3 Methods used for adhesion test of electrodeposits

The adhesion of a substrate-coating system can be assessed by many adhesion tests available in the literature. Mechanical adhesion tests, such as those based on peeling, shearing and scratching, are mostly used for adhesion assessment of thin films coated on a substrate. In the first two methods, adhesives are used for the assessment of the adhesion of the coating to the substrate. The challenge is to find an adhesive that adheres strongly enough so that the failure occurs at the interface of the coating and substrate during the peel test, but which also would not

significantly alter the mechanical properties of the coating itself. In this work, the scratch test was used for the adhesion assessment of nickel deposit to the substrate.

2.3.3.1 Scratch test method

In this method, an indenter (stylus), generally made of diamond, chrome steel or tungsten, provided with a tip radius moves over a film surface while either a constant or progressively (either continuously or step-wise) increased load (Sergici and Randal, 2006; Majolaine , 1999; Blees et al., 2000) is applied on the indenter until failure of the interface between the film and the substrate occurs at the so called critical load, with the normal load applied on the indenter and the friction forces between the indenter and the specimen being recorded (Kovaleva et al., 2008, 2011). When adhesion failure occurs at the critical load, a set of indicative events usually accompanies the failure, such as separation between the coating and the substrate, observable using optical microscopy, or significant emission of acoustic waves resulting from the formation or propagation of micro-cracks when failure occurs at the interface, which can be recorded using acoustic sensors, or a sudden drop in depth of the indenter tip due to the space at the interface when failure occurs, which can be measured using linear motion sensors, or a sudden significant change in friction response that can be detected from the friction force measurement. Any of these phenomena alone or in combination with another can be used for the determination of the critical load (Angle, 2010; Secor, 1994).

The method is applied for both thick, in the range of millimetres (macro-scratch test), and thin, in the micro- and nano-range (micro-scratch and nano-scratch, respectively) (Li, 2013). The critical load measured is just an indicative value of the coating-substrate adhesion and is usually used to compare the cohesive or adhesion properties of coatings or bulk materials, respectively. Under recommended standard experimental conditions in terms of film parameters, i.e., thickness, hardness, and test parameters, such as the scratch rate, indenter radius, load rate, load type and friction coefficient at critical load (Steinmann et al., 1987; Tomastik and Ctvrtlik, 2013), it is used together with the relative friction coefficient for the determination of approximate interfacial shear stress or work of adhesion using different models available in the literature (Coghill and St. John, 1990) that take into account all these parameters. Alternatively, artificial intelligence systems are used to convert the measurement conditions and measured data so that data can be effectively used for comparisons of results (Socha et al., 2013). There are many standard conditions in

the literature for scratch tests for various systems (Kutilek and Miksovky, 2011; Angle, 2010; Socha et al., 2013). The detachment initiated in the vicinity of the indenter and the failure mode also depends on the relative hardness of both the film and the substrate so that the scratch test method may be less efficient in some systems, such as when the substrate is softer than the film. However, the method provides a good comparison of adhesions of identical film-substrate combinations, irrespective of the relative hardness of the film and substrate (Butler et al., 1970).

2.3.3.2 Limitation of the scratch test

Scratch tests involve a great number of variables and existing models invariably use assumptions and simplifications to deal with the complexity of scratch tests so that models that give a complete analytical description of the mechanics of scratch tests are problematic. Presently, there is no standard scratch test model that gives a complete description of mechanics for scratch testing of any system with confident calculation of interface adhesion strength in terms of shear stress, tensile stress or work of adhesion for failure (Kuiry, 2012). The critical normal load and/or the corresponding friction coefficient are the characteristic parameters often used for the presentation and comparison of scratch test results and are kinds of measures of relative adhesion strength.

2.3.4 Analytical techniques for nickel electrodeposits

A wide range of analytical techniques are available for the qualitative and quantitative analysis of the electrodeposits. This includes, among others, atomic absorption spectroscopy (AAS), SEM, transmission electron microscopy (TEM) and X-ray diffraction (XRD). In this work two analytical techniques were used for impurity analysis: inductively coupled plasma mass spectroscopy (ICP-MS) and energy-dispersive X-ray spectrometry (EDS).

In the ICP-MS technique, a diluted aqueous sample is introduced into a high temperature (6000 - 10000 K) plasma and is directly desolvated and elements are converted into gaseous atoms and then ionized positively at the end of the plasma-tube. This technique is widely used for analysis with high sensitivity for elements that preferentially form positive ions, such as the metallic impurities of interest in this work. The EDS technique, which is most commonly used in conjunction with SEM, can detect all elements from atomic number 4 (Be) to 92 (U) (Hafner, 2014), which includes oxygen (Z = 16) that cannot be analysed by other

analytical methods. The detection limit of this technique is typically about 1000 mg/kg by mass (0.1 mass %), which can be improved with longer count receiving times (Noran Instruments, 1999).

Chapter 3 Experimental and analysis

3.1 Electrodeposition experiments

In this work, synthetic standard electrolytes prepared with American Chemical Society (ACS) grade chemicals from Merck, containing 80 g/L nickel, added as $NiSO_4.6H_2O$ (Ni > 99.9%, Co < 0.001%, Cu < 0.001%, Fe < 0.001%, Mn < 0.002%, Mg < 0.005%, K < 0.01%, Na < 0.001%, Ca < 0.005%) , 8 g/L boric acid and 80 g/L sodium sulfate were used for all the experiments. The pH was adjusted to 3.5 using sulphuric acid (98.0%) from Merck. Impurities were added as high-purity copper sulfate, cobalt sulfate, aluminium (III) sulfate or chromium (III) sulfate prior the experiments in small amounts to the electrolyte to obtain the desired impurity concentration of only a few mg/L in the electrolyte. Experiments were done in a vertical parallel-plate cell and the temperature kept at 60 ± 1°C by circulating water through a jacket surrounding the cell. The nickel was plated using 100 ml electrolyte under galvanostatic conditions at a current density of 215 A/m^2 using a Schlumberger SI 1286 potentiostat as a galvanostat.

Titanium sheets with dimensions of 22 mm x 40 mm x 3 mm, of 99.6% purity, were used as rigid cathodes for visual assessment of the effect of impurities on the morphology of the deposit. A flexible cathode made of titanium foil, 0.75 mm thick, with the same exposed area was used for the internal stress measurements as well as for adhesion tests. During the deposition process, the titanium substrates were isolated on the back side with a thin silicone coating to avoid plating at the back of the cathode and so as not to significantly affect the mechanical properties of the titanium substrate.

The anode, of 20 mm x 40 mm active area, was made of a Pb — 0.1% Ag alloy. Its width was chosen slightly smaller than that of the cathode to discourage edge effects on the cathode. A polypropylene bag was used to isolate the anode from the catholyte and limit the transport of hydrogen ions produced at anode to the cathode surface. Both the titanium cathode and the lead alloy anode were clamped at the top in a cantilever arrangement so that they were vertically parallel in the electrolyte and separated by 15 mm to minimize disturbance of current distribution for small deflections. Experiments were conducted for 3 hours. This time gave, under the above conditions, an internal stress of approximately 200 MPa. Deposits for adhesion tests were plated for 45 minutes.

3.2 Internal stress measurements

The internal stress was measured using a thin (0.75 mm) titanium bending substrate used as cathode that was clamped in a cantilever arrangement parallel to the anode, free on the side opposing the anode and isolated electrically on the other side using a silicone coating so that deposition could occur only on the former side. As the stress developed in the film that deposits onto the substrate during electrodeposition, both the substrate and the deposit bent together as a compound beam. The deflection of the beam was monitored using a linear variable differential transformer (LVDT) of high sensitivity (750 mV/mm at 10 V under direct current (DC) supply) from Solartron as transducer, coupled to a datataker DT 50 from dataTaker as signal conditioner, that detected the linear bottom substrate motion during deflection via a light and electrically isolated rod pivoting around a well-lubricated fulcrum, the bottom of which was linked to the substrate bottom in the cell and the top to the LVDT core tip outside the cell. The average stress throughout the deposit was calculated using the Stoney equation (Equation 2.20 given in Chapter 2). The film thickness was estimated using the mass of the deposit in grams and the active plating area of 40 mm x 22 mm fixed from the set-up, using a nickel density of 8902 kg/m^3, the thickness being the volume/active area ratio. The titanium substrate elastic modulus and Poisson's ratio were taken as 110 GPa and 0.28, respectively, as reported in table 2.10. A schematic diagram of the experimental set-up for the stress measurement is given in Figure 3.1.

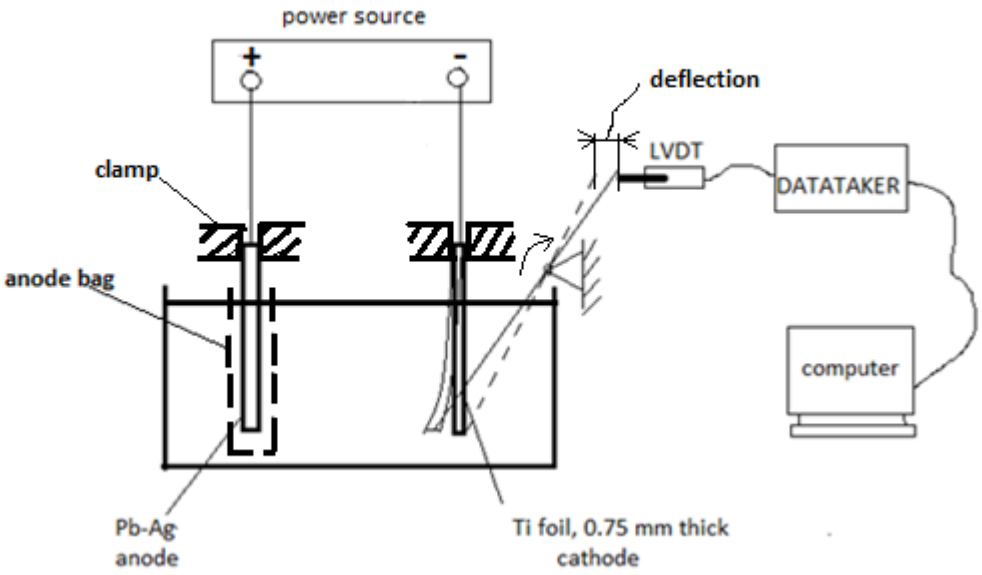

Figure 3.1. Schematic presentation of the experimental setup used for internal stress measurements in the electrodeposited nickel.

3.3 Yield stress determination

The yield stress of the electroplated nickel due to grain refinement was estimated in the present work by determining the average grain size, using the intercept method on SEM images, and calculating the yield stress using the Hall-Petch relationship. For all the electrodeposits an average intrinsic stress σ_o and the constant k of 20 MPa and 0.16 MPa.m$^{1/2}$, respectively, were taken as Hall-Petch constants as found in previous work for pure nickel (Carlton and Ferreira, 2007; Armstrong, 2013, 2014), assuming that the low levels of impurities investigated would not have a significant effect on these constants. The yield stress due to solid strengthening was calculated using Equation 2.21 and a nickel shear modulus and atomic radius of 76 GPa and 0.125 nm, respectively, as given in the literature (Wikipedia, 2015). The influence of solid strenghtening by the impurities was found to be insignificant compared with their influence on the grain size and thus the yield stress, as indicated in Table 4.1. In this work, the change of yield stress due to solid strengthening was neglected in view of the dominant effect of changes in grain size.

3.4 Adhesion strength assessment

The adhesion between the plated metal and the titanium substrate was measured using a simple set-up for the scratch method. The method is widely used and provides a good comparison of adhesion of similar film-substrate combinations although the failure mode depends on the coating system (Coghill and St. John, 1990; Butler et al., 1970). The relative adhesion strength of nickel electrodeposited on the titanium substrate (40 mm x 22 mm active area) of 0.75 mm thick at a current density of 215 A/m^2 for 45 minutes from impurity containing electrolytes (80 g/L Ni, 8 g/L boric acid, 80 g/L sodium sulfate, pH 3.5, temperature 60^{o}C, variable impurity contents) was assessed by using a beam balanced by one single mass of 50 g on one side and 50 equal small masses of 1 g each, giving a total mass of 50g on the other side. A needle indenter with a 2 µm tip radius was mounted vertically to the beam below the big single mass with the tip turned down so that by removing the small masses of 1 g one by one at 5 second intervals, the beam become progressively unbalanced and the indenter exerted an increasing step-wise load on the specimen in contact with the indenter tip. A linear piezo actuator (N-380 type, 10 N max, stroke 30 mm, maximum velocity 10 mm/s) under pushing mode was used to horizontally shift the board that carried the specimen relatively to the indenter at a rate of 0.1 mm/s, causing a scratch on the specimen. A small portable scale with liquid-crystal

display (LCD) of 100 g x 0.01 was used as junction between the board and the actuator so that it could measure friction forces between the specimen and the indenter tip as they were in relative motion in the horizontal direction while friction resisted their motion. The resistance to this relative motion of the specimen to the indenter made the actuator exert a force on the scale to overcome that resistance so that the scale could give a reading as a friction force value. To minimize the contribution of friction forces from other sources, both the board and the portable scale that were pushed together by the actuator were carried by a tray that was rolling on a smooth plank set on the laboratory bench so that when the indenter was not in contact with the specimen, there was almost no resistance to the tray motion. The normal load at a given step could be calculated from the difference between the single big mass of 50 g and the total mass of small masses removed on the other side of the beam. Particles of almost 1 cm^3 volume of a sheet of polystyrene (density: 1.04 g/cm^3) adjusted to 1 g each were used as small masses that were easy to remove manually. One small mass was removed every 5 s so that an additional normal load of 1g was applied on the specimen every 5 s and friction forces could be read from the scale step by step until a sudden change in friction response was noticed for one more single gram applied to the specimen (that could be at least five times or more the increase in friction force obtained after several grams normal load applied on the specimen). A countdown timer was used as timer, set for beeping every 5 s for removal of small masses. All the experiments were stopped when this sudden change in friction response, corresponding to the critical normal load, which is a measure of the cathode-substrate adhesion strength, was obtained.

The friction coefficient between the nickel deposit and the titanium substrate was calculated from the slope at the critical load of the friction force-normal load curve as previously done by Sukhorukov and Loset (2013) using Equation 3.1. A simplified schematic diagram of the set-up used for adhesion tests is represented in Figure 3.2.

$$\mu_k = \Delta F_n / \Delta F_f \qquad 3.1$$

where ΔF_n is the change of applied normal force at critical load,

ΔF_f is the change of measured friction force at critical load,

μ_k is the friction coefficient at the interface.

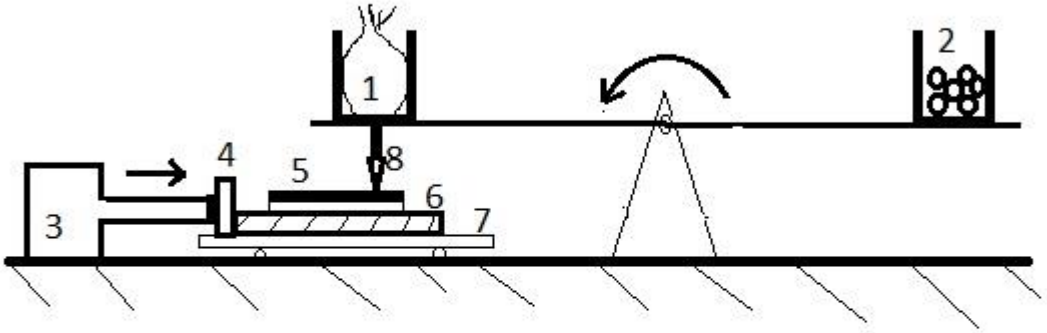

1. 50 g mass
2. 50 small masses of 1 g each
3. linear actuator
4. scale with LCD display
5. specimen (substrate and deposit)
6. carrying board
7. rolling tray
8. stylus indenter

Figure 3.2. Schematic presentation of the experimental setup used for adhesion strength measurements at the deposit-substrate interface.

3.5 Analysis of the deposit

The SEM analyses performed in this work were done on an ultrahigh resolution field emission (JEOL 6000F) machine at 15 kV acceleration voltage on all the samples. A silicon drift energy dispersive X-ray spectrometer (Oxford XMax 100 TLE energy) machine was used for EDS analysis and performed at 15 kV acceleration voltage. A Perkin Elmer ELAN 6100 inductively coupled plasma-mass spectrometer was used for ICP-MS analyses.

For all the electrodeposition experiments, the titanium substrates were washed in ethanol, rinsed with de-ionised water and air dried. The substrates were then pickled in a solution of nitric acid with some hydrofluoric acid in the volume ratio of 15 to 1 for 1 minute at ambient temperature, rinsed in de-ionised water and air dried. After electrodeposition, the electrode was rinsed with de-ionised water to remove entrapped solution and dried under atmospheric conditions. The deposit was then separated by peeling it from the titanium substrate and prepared for analysis.

For the EDS analysis, a portion of the nickel deposit sample was cold mounted in resin, polished with 800 and 1200 grit papers, rinsed with ethanol followed by de-ionised water and dried in air. Another portion of the deposit was cut using a pair of scissors into small pieces to obtain a representative sample of approximately 0.1 g, which was dissolved in aqua regia and diluted with de-ionised water for chemical analysis by ICP-MS. The dilutions were made such that sensibly detectible concentrations were obtained.

3.6 Potentiodynamic tests

Potentiodynamic cathodic polarisation tests were done to investigate the influence of aluminium and chromium in the electrolyte on the polarization characteristics of the system. Polarization was done at a scan rate of 5 mV/s from a potential of 0 to -1.2 V using a Ag/AgCl/3 M KCl reference electrode. A Schlumberger SI 1286 potentiostat was used to control and scan the potential of a titanium working electrode (22 mm x 40 mm active areas) using a Pb — 0.1%Ag alloy counter electrode of 20 mm x 40 mm active areas. Other parameters, such as the bath temperature, pH, boric acid, sodium sulfate and nickel concentrations, were kept constant, as described in section 3.1.

3.7 Range of impurity concentrations investigated

Electrolytes with both low and high ranges of impurities, up to 500 mg/L for copper and cobalt, 100 mg/L for chromium and 2500 mg/L for aluminium were used, as summarised in Table 3.1. Only one type of impurity at a given concentration was used for each experiment. All experiments were repeated at least three times to evaluate the repeatability of the results.

Table 3.1. Electrolyte impurity concentrations used for internal stress measurements (I), yield stress determinations (Y) and adhesion at the deposit-substrate interface (A).

Impurity concentration (mg/L)	Cu	Co	Al	Cr
0	I, Y, A	I , Y, A	I, Y, A	I, Y, A
5	I, Y, A	I, Y, A	I, Y, A	I, Y, A
10	I, Y, A	I, Y, A	I, Y, A	I, Y, A
15	I, Y, A	I, Y, A	I, Y, A	I, Y, A
20	I, Y, A	I, Y, A	I, Y, A	I, Y, A
25	I	I	I	I
40	I	I	I	I
50	I	I	I	I, Y
60	I	I	I	I
80	I	I	I	I, Y
100	I, Y	I, Y	I	I, Y
250	I, Y	I, Y		
300			I, Y	
500	I, Y	I, Y		
625			I	
1250			I, Y	
2500			I, Y	

Chapter 4 Results and discussion

4.1 Internal stress in nickel deposits as a function of impurity concentration in the electrolyte

The effects of impurities on the morphology of electrodeposited nickel are typically assessed by visual observation (O'Keefe and Holm, 2000; Das and Gogia, 1988, 1991). In this work, the internal stress in the deposit was also assessed using single-side plating on a flexible beam with recording of the deflection of the beam with an LVDT, as described in Section 3.2.

The results indicate that nickel electroplated from a nominally pure nickel sulfate solution contains internal tensile stresses, of the order of 200 MPa under the conditions used, and that these stresses are increased to lesser or larger extents, with values of up to 900 MPa, by the presence of impurities in the electrolyte, as indicated in Figures 4.1 and 4.2. This range of stress for nickel plated from an impurity-free electrolyte compares well with that found in the literature (Kopeliovich, 2013).

The results show that aluminium in the electrolyte quickly increased the internal tensile stress and at a relatively higher rate compared with copper and cobalt but also decreased it beyond 300 mg/L, such that at around 2500 mg/L, the stress was comparable to that obtained for the impurity-free electrolyte. Copper increased the stresses at concentrations close to 20 mg/L in the electrolyte but the internal stress leveled off at about 100 mg/L at a value of 600 MPa and only slightly increased at copper levels above 500 mg/L. Cobalt in the electrolyte tended to slightly shift the internal stress to more compressive values at low concentrations of up to around 25 mg/L and then increased the stress slightly and almost linearly at higher concentrations. Chromium in the electrolyte was the most harmful impurity. The tensile internal stress in the plated metal increased quickly with chromium in the electrolyte from very low concentrations, such that a nominal internal stress of about 900 MPa was generated by 100 mg/L of chromium.

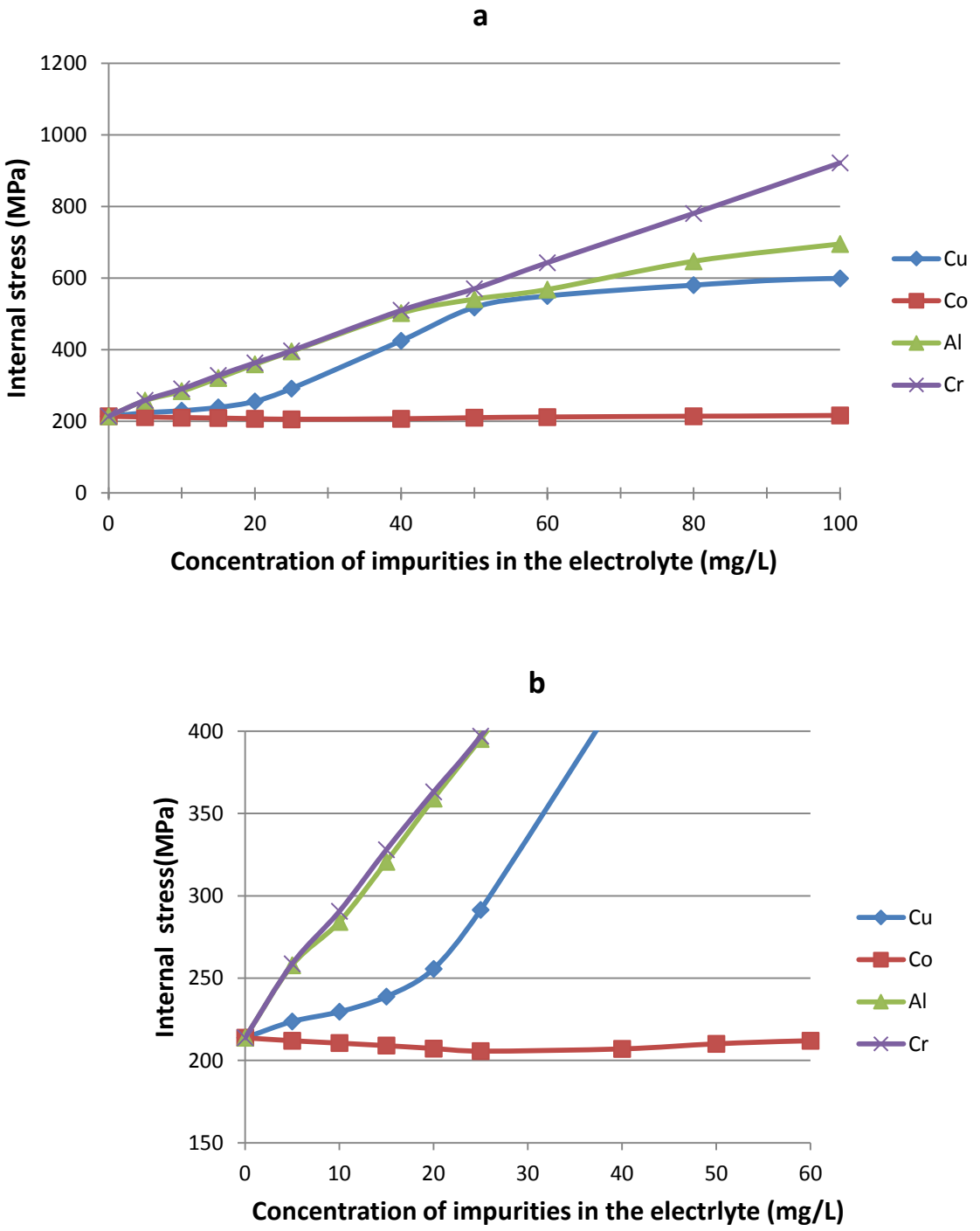

Figure 4.1. Measured internal stresses in electroplated nickel as a function of impurity concentrations in the electrolyte of up to 100 mg/L (a), 60 mg/L (b).

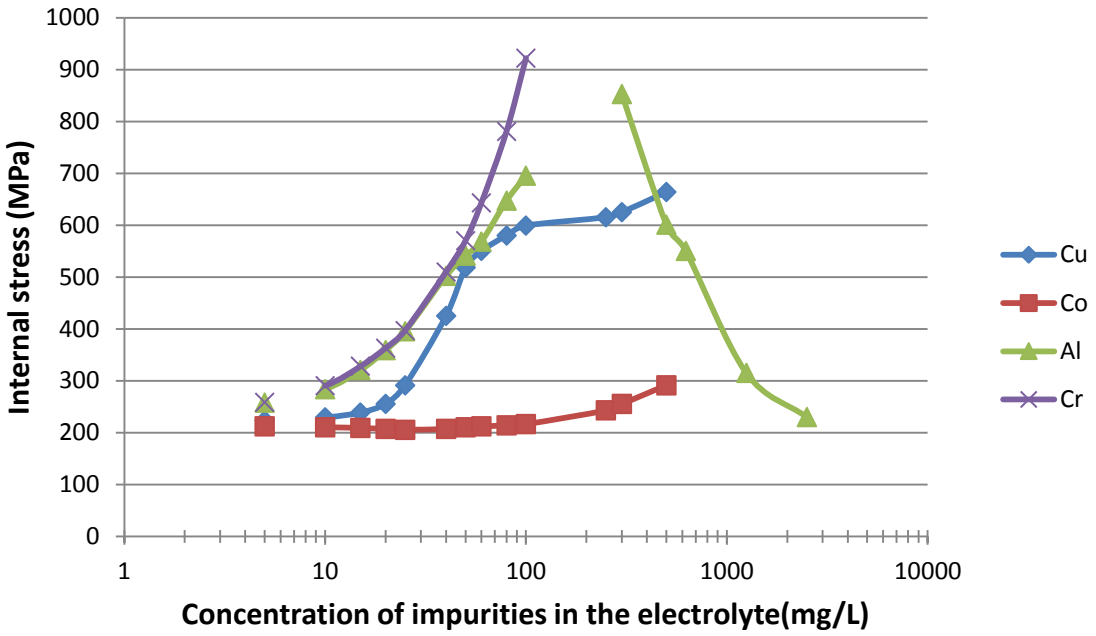

Figure 4.2. Internal stresses in electroplated nickel as a function of higher electrolyte impurity concentrations.

4.2 Internal stress in nickel deposits as a function of impurity concentration in the deposit

The results indicated in Figures 4.3 to 4.6 show similar trends for the impurity contents and the internal stresses in the plated nickel. It is clear that the level of internal stress developed is related to the degree of incorporation of the impurity in the plated nickel, which is, in turn, related to the impurity concentration in the electrolyte. Increasing impurity contents in the deposit gave an increase in internal stress in the deposit, probably due to local defect points giving lattice plane distortion in the deposit network as mentioned in Section 2.2.2.5 of Chapter 2. The relatively small effect of cobalt in the nickel on stress development is probably due to the small differences in the properties of these metals in terms of valence, atomic radius, and electronegativity that rule solid solutions.

Aluminium uptake in the deposit was proportional to that in the electrolyte and caused an increase in internal stress. However, at higher aluminium concentrations in the electrolyte, the uptake of aluminium in the deposit decreased and, as expected, the internal stress also decreased accordingly. These results are consistent with those found in previous work using visual characterisation of the nickel deposited from aluminium-containing electrolytes, where low concentrations of aluminium

significantly degraded the nickel cathode morphology while compact and smooth deposits were obtained at higher aluminium concentrations in the electrolyte (Kittelty, 2002; Mohanty et al., 2005; O'Keefe and Holm, 2000).

The impurity concentration and internal stress in the nickel deposit increased monotonically with copper and chromium concentrations in the electrolyte in the range of concentration investigated.

4.3 Mechanical properties and maximum stress criteria on nickel deposits

As mentioned in Section 2.2.2.8, the failures observed in nickel deposits during electrodeposition in terms of delamination, cracking or debonding are the consequence of the propagation of microcracks or similar flaws. In addition, it can be expected that the plated nickel would fail if plastically deformed in a highly localised manner, as would be likely once the internal stress approaches the flow stress of the material on a stiff substrate. In order to evaluate the effects of impurities via internal stresses developed in the nickel deposits obtained from impurity-containing electrolytes on such failures, internal stresses were compared with the estimated yield stress. The maximum stress criteria, which states that failure occurs when the maximum (normal) principle stress exceeds either the tension or compression strength for materials behaving as brittle materials, with or without local plastic zones at crack tips (Brinson and Brinson, 2015), can be applied for the prediction of macroscopic failure in the constrained nickel deposits.

The results shown in Figures 4.3b to 4.6b indicate some commensurate increases in the estimated yield stresses with impurity concentration in the deposit due to some degree of grain refining of the electroplated metal and solid-solution hardening, as indicated in Table 4.1, where a grain size d of a deposit is the average of grain size values found at different regions of the deposit, the grain size in a region being the average of grain size calculated for intercept lines drawn in different directions using the intercept method described in Section2.3.2. This is done because electroplated metals generally do have not the same grain size all over as mentioned in the same Section.

However it is clear that the expected effect of solid-solution hardening is negligible and so this was not further considered. The difference in the rate of change of the internal stress with impurity concentration was higher than that of grain refining on the yield stress, with the result that the internal stress exceeded the yield stress with

commensurate failure of the deposit at concentrations of around 4.5 mg/L for both chromium and aluminium, 45 mg/L for copper and 450 mg/L for cobalt. In the case of aluminium, however, the estimated yield stress once again exceeded the internal stress at around 1650 mg/L and relatively smooth and compact deposits were again obtained. Data used for the construction of figure 4.3a to 4.6a and 4.3b to 4.6b are provided in the appendice tables A1.1 to A1.8 and A2.1 to A2.2, respectively.

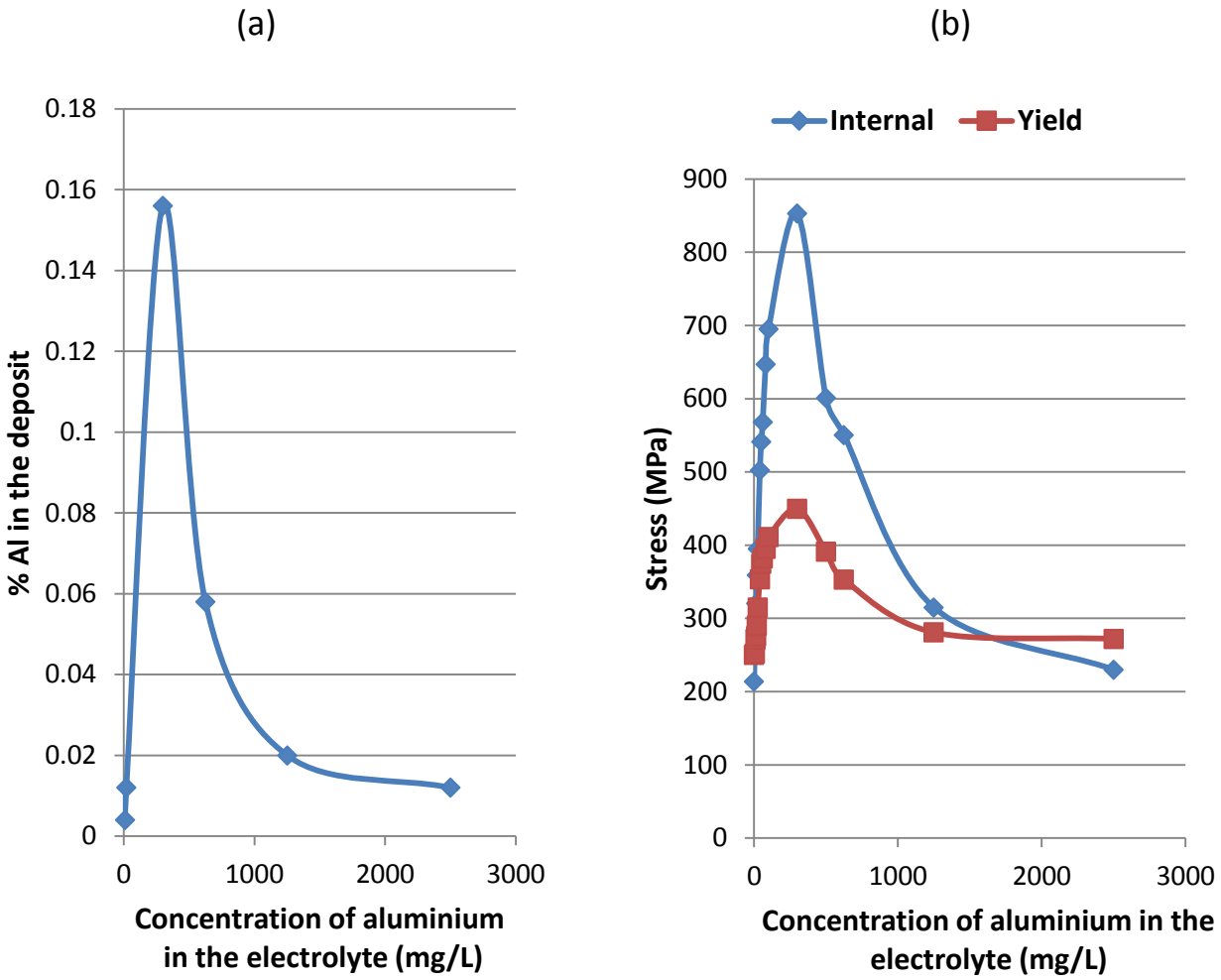

Figure 4.3. Variation of the (a) aluminium content in nickel electrodeposited from aluminium-containing electrolytes, (b) internal stress and calculated yield stress, as a function of concentration of aluminium in the electrolyte.

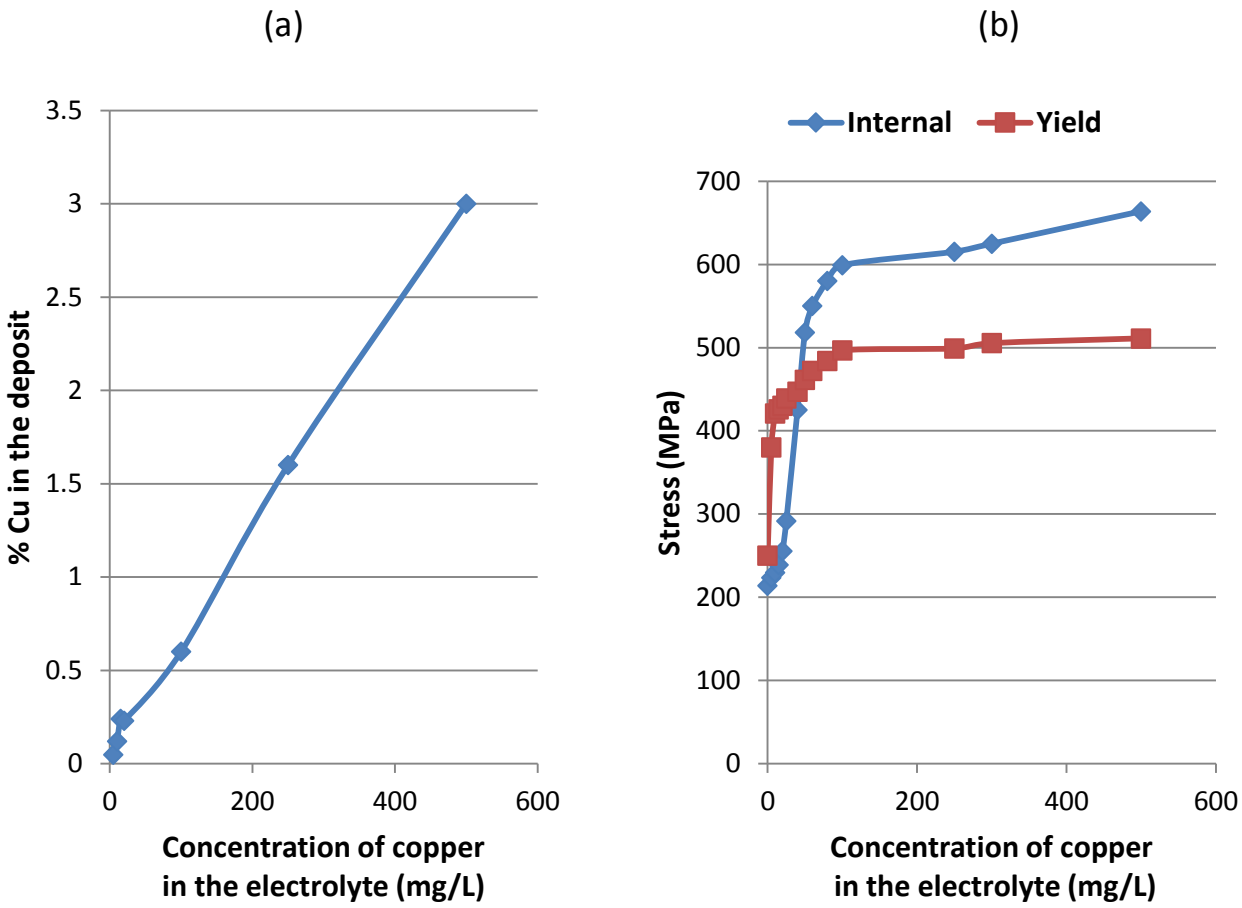

Figure 4.4. Variation of the (a) copper content in nickel electrodeposited from copper-containing electrolytes, (b) internal stress and calculated yield stress, as a function of concentration of copper in the electrolyte.

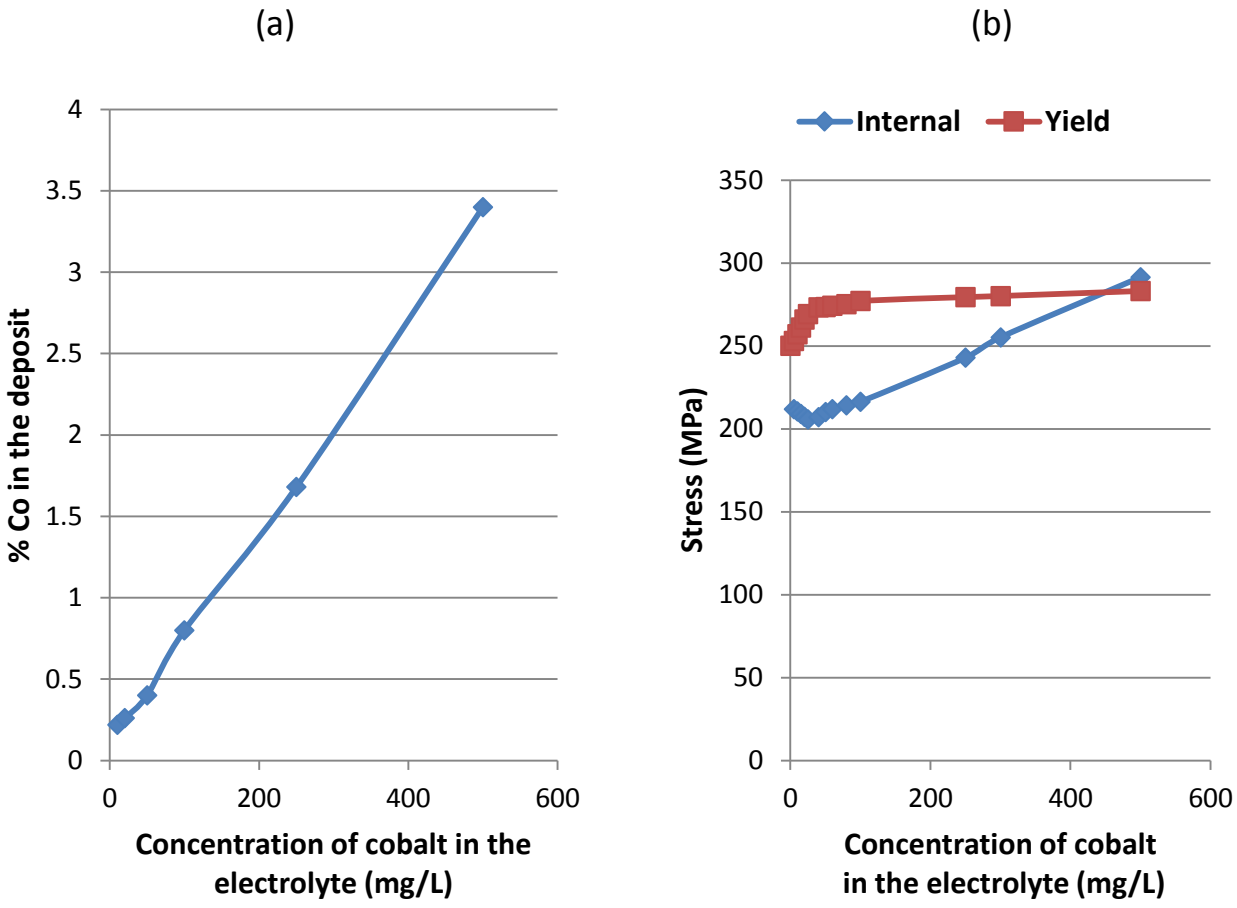

Figure 4.5. Variation of the (a) cobalt content in nickel electrodeposited from cobalt-containing electrolytes, (b) internal stress and calculated yield stress, as a function of concentration of cobalt in the electrolyte.

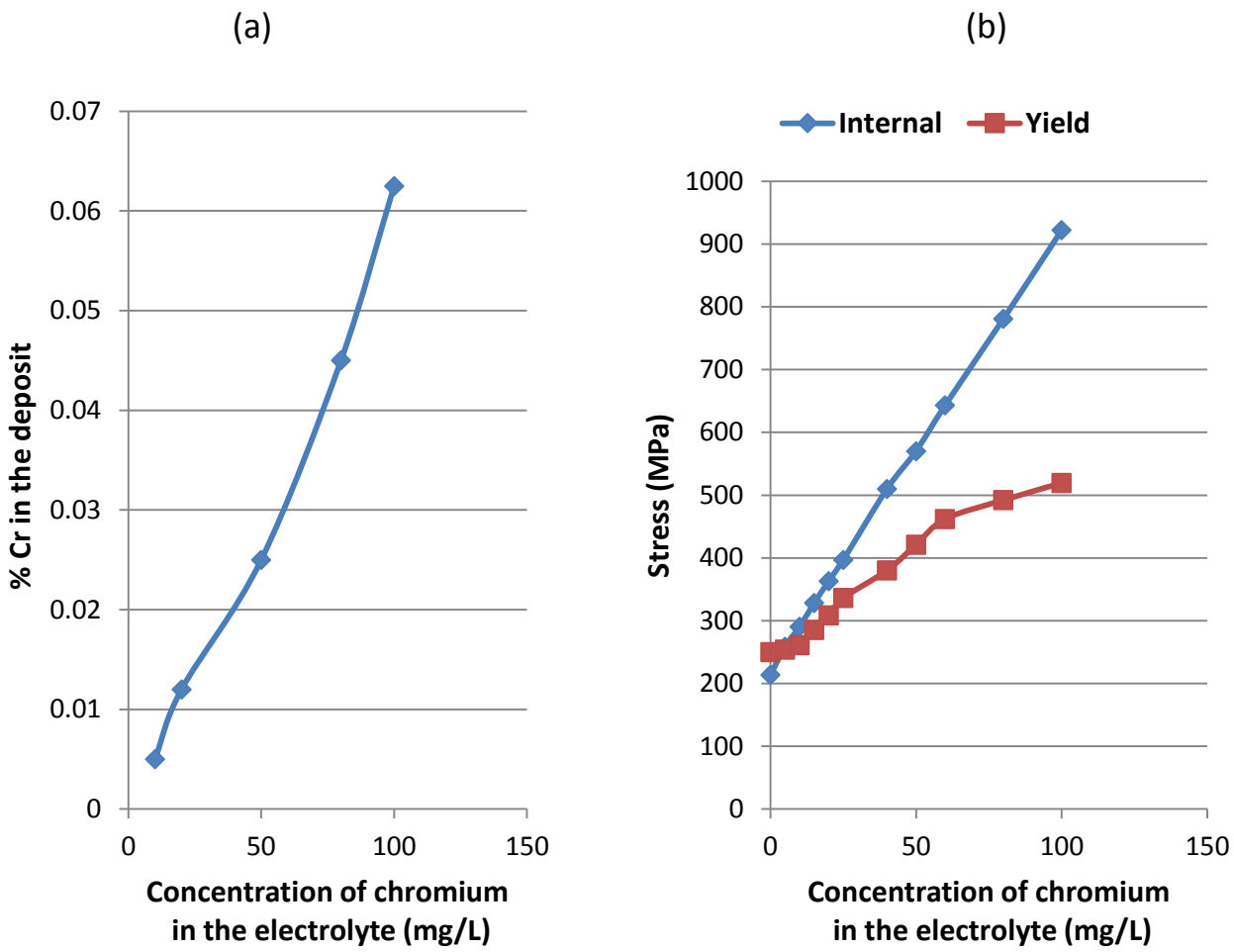

Figure 4.6. Variation of the (a) chromium content in nickel electrodeposited from chromium-containing electrolytes, (b) internal stress and calculated yield stress, as a function of concentration of chromium in the electrolyte.

Table 4.1. Measured grain size and calculated yield stress induced by impurities in nickel deposits.

Impurity type in the electrolyte	Electrolyte (mg/L)	Impurity concentration in the deposit (mass %)	Impurity concentration in the deposit (atomic %)	Strain misfit ε	Atomic radius r (nm)	Measured grain size d (nm)	Calculated yield stress σ_s due to solid-solution hardening (MPa)	Calculated yield stress σ_H due to grain size refinement (MPa)	σ_s/σ_H (%)
Al	10	0.004	0.01	0.144	0.143	405	1.714	271.3	0.631
	20	0.012	0.03			351	5.142	290.2	1.772
	300	0.156	0.34			139	66.727	449.8	14.835
	625	0.058	0.13			231	24.837	353.0	7.036
	1250	0.02	0.04			376	8.568	281.0	3.049
	2500	0.012	0.03			403	5.142	272.1	1.89
Cu	10	0.12	0.11	0.024	0.128	159	0.606	421.0	0.144
	15	0.24	0.22			155	1.213	426.0	0.285
	20	0.32	0.3			152	1.618	430.0	0.376
	100	0.6	0.55			113	3.034	496.8	0.611
	250	1.6	1.48			112	8.096	499.0	1.622
	500	3	2.78			106	15.195	511.2	2.973
Co	10	0.22	0.22	0.008	0.124	456	0.133	257.0	0.052
	20	0.26	0.26			423	0.157	266.0	0.059
	50	0.4	0.4			399	0.242	273.5	0.088
	100	0.8	0.8			387	0.484	277.2	0.175
	250	1.68	1.67			380	1.017	279.4	0.364
	500	3.4	3.39			369	2.059	283.1	0.727
Cr	10	0.005	0.01	0.032	0.129	441	0.055	261.0	0.021
	20	0.012	0.01			308	0.132	308.4	0.043
	50	0.025	0.03			159	0.274	421.1	0.065
	80	0.045	0.05			115	0.494	492.1	0.1
	100	0.0625	0.07			103	0.686	519.3	0.132

4.4 Deposit morphology

The degradation of the quality of the nickel deposited from sulfate electrolytes containing copper, cobalt, chromium and aluminium impurities under different electrodeposition conditions in the nickel deposit has been ascribed to internal stresses in previous work, where the internal stresses were not measured but the effects of impurities were evaluated by visual assessment of the deposit quality (Das and Gogia, 1988; Das and Gogia, 1991; O'Keefe and Holm, 2000; Mohanty et al., 2005). Results reported in the literature on impurity limits for nickel electroplating from sulfate electrolytes are summarised in Section 2.1.5 and Table 2.5, indicating that impurity concentrations for smooth nickel deposits from sulfate electrolytes range from 40 to 100 mg/L Cu, 5 to 10 mg/L Cr, 5 to 10 mg/L Al and around 500 mg/L Co.

Using the maximum stress criteria with the measured internal stress and the measured yield stress considering both the grain refinement and solid solution hardening described in section 2.3.2, combined with the visual assessment, similar results to those reported in the literature were found, as illustrated in Figures 4.3b to 4.6b and Table 4.2, which indicate visual observable failures of the deposits when the measured internal tensile stress exceeded the estimated yield strength of the plated metal. These failures are most likely the result of some kind of crack or similar defect propagating between adjacent layers in the deposit in the case of delamination, along the deposit-substrate interface for debonding and laterally or in other directions through the failed deposits. In this work, the impurity limits for smooth and well-adhered nickel deposits were found at concentrations of at 4.5 mg/L for both chromium and aluminium and around 45 mg/L for copper and 450 mg/L for cobalt. Beyond these concentrations, deposits started to crack more and more with increasing impurity concentration and delaminated and/or peeled at relatively higher concentrations. However, in the case of aluminium, relatively good nickel deposit morphology was also obtained from around 1650 mg/L aluminium in the electrolyte at which the estimated yield stress once again exceeded the internal stress. Selected photographs of deposits are presented in figure 4.7, showing typical good and bad morphology.

Table 4.2. Visual observation of the morphology of nickel deposited on the stiff titanium substrate at different concentrations of impurities.

Impurity concentration in the electrolyte (mg/L)	0	5	10	15	20	25	40	50	60	80	100	250	325	500	625	1250	2500
Al	N	Y/N	Y	Y	Y	Y	Y	Y	Y	Y	Y		Y	Y/N	Y/N	Y/N	N
Cu	N	N	N	N	N	N	Y/N	Y	Y	Y	Y	Y		Y			
Co	N	N	N	N	N	N	N	N	N	N	Y/N	Y/N		Y			
Cr	N	Y/N	Y	Y	Y	Y	Y	Y	Y	Y	Y						

Nickel: 80 g/L pH: 3.5
Boric acid: 8 g/L Temperature: 60 ± 1°C
Sodium sulfate: 80 g/L

N: good (for compact smooth deposit), Y: bad (for excessive cracks, delamination or peeling), Y/N: intermediate.

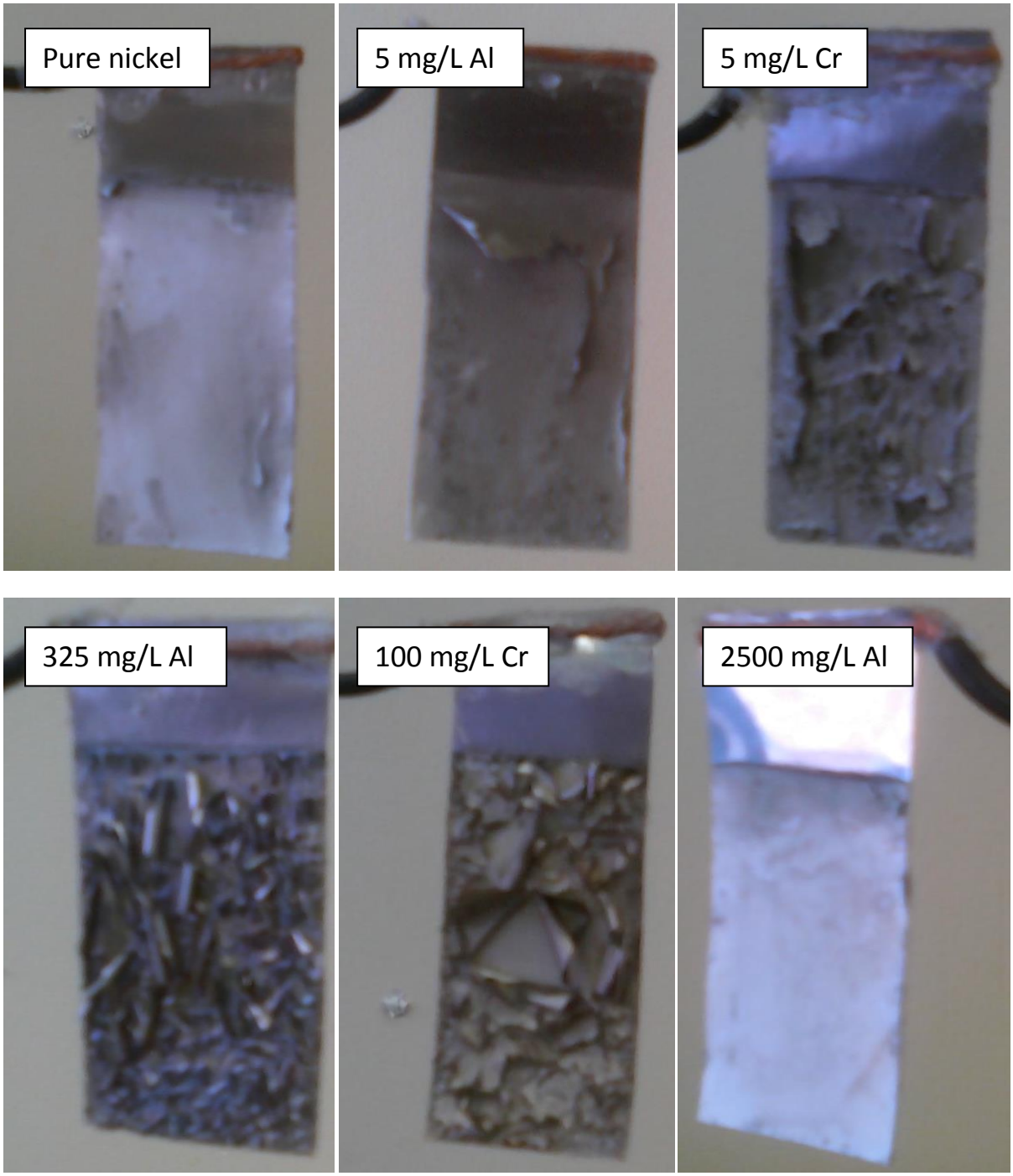

Figure 4.7. Typical photographs representing different nickel deposit conditions as a function of impurity concentration in the electrolyte.

4.5 Chemical composition of nickel deposits as a function of the impurity concentration in the electrolyte

The chemical compositions obtained from ICP analyses of the nickel deposits plated from the different electrolytes are indicated in Figures 4.3a to 4.6a. In the case of aluminium, the impurity content increased with aluminium concentration in the

electrolyte in the low range of concentrations and decreased with increasing aluminium concentrations in the electrolyte in the higher range, typically beyond 300 mg/L. Increasing impurity concentrations in the electrolyte resulted in increasing concentrations in the plated metal for copper, cobalt and chromium, in the range of impurity concentrations investigated. The ratios of impurity/nickel in both the electrolyte and the deposit are indicated in Figure 4.8 (constructed on the manipulation of appendices tables A2.1 and A2.2) and Table 4.3, which show that copper and cobalt are preferentially plated to nickel but not so as expected in the case of aluminium and chromium. The impurity content in the deposit is proportional, according to Faraday's law, to the partial current density, which, in turn, varies exponentially with the overpotential according to the Bulter-Volmer equation (Garrido, 2009), when the plating reaction itself is rate determining, and linearly with the concentration in the electrolyte if mass transfer is rate determining. The much higher overpotential for copper plating of about 0.61 V (considering copper and nickel reduction potentials of + 0.34 V_{SHE} and – 0.27 V_{SHE}, respectively), should favour its plating at low overpotentials for nickel plating but the ratio of copper to nickel plating should decrease with increasing overpotentials for nickel as its plating should strongly increase as it would be under reaction control while that of copper should already be under mass-transfer control and should not change significantly at increasing overpotentials. The higher Cu/Ni ratio in the deposit compared with the ratio in the electrolyte indicates that the effect of the higher overpotential for copper is still dominant at the electrode potentials realised at the current density of 215 A/m^2 used in the present case.

At a cathode potential of around – 0.6 V_{SHE} (– 0.799 $V_{Ag/AgCl}$), the cobalt overpotential (– 0.33 V), based on a reversible potential of – 0.27 V_{SHE} (– 0.469 $V_{Ag/AgCl}$), is slightly lower than that of nickel but the higher ratio of Co/Ni in the deposit than that in the electrolyte indicates cobalt deposits by anomalous deposition described in Section 2.2.1.2.9. The higher deposition rates of copper and cobalt can be seen in Figures 4.8a and 4.8b, where the atomic ratio in the deposit is significantly above the 1/1 ratio in the electrolyte. In contrast the cathode potential of – 0.6 V_{SHE} (– 0.799 $V_{Ag/AgCl}$) is significantly more positive than the reduction potentials of – 1.66 V_{SHE} (– 1.859 $V_{Ag/AgCl}$) and – 0.74V_{SHE} (– 0.939 $V_{Ag/AgCl}$) of aluminium and chromium, respectively (Wikipedia, 2015), but yet they reported in the deposit. These impurities most probably plated on the nickel substrate by an underpotential deposition mechanism, mentioned in the same section, with relatively low deposition rates, as also found in

the potentiodynamic results reported in Section 4.7. Possible underpotential deposition of aluminium and chromium on nickel substrate has been reported in some previous studies (Berg et al., 1991; Surviliene et al., 2013) and codeposition with nickel from sulfate electrolytes in some other studies (O'Keefe and Holm, 2000; Das and Gogia, 1988; Mohanty et al., 2005). The anomalous codeposition of cobalt from a nickel electrolyte has also been reported by Fan and Piron (1996).

Table 4.3. Chemical composition of the nickel deposits as a function of impurity concentrations in the electrolyte.

Impurity type in the electrolyte	Impurity concentration in the electrolyte (mg/L)	Impurity concentration in the deposit (mass %)	Impurity concentration in the deposit (atomic %)	Nickel concentration in the deposit (atomic %)	Impurity concentration in the electrolyte (mmol/L)	Mol ratio in the electrolyte (mmol/L Me/mmol/L Ni)	Atom ratio in the deposit (at% Me/at% Ni)
Al	10	0.004	0.01	99.99	0.37	2.72E-04	8.70E-05
	20	0.12	0.026	99.74	0.74	5.43E-04	2.62E-04
	300	0.156	0.34	99.66	11.11	8.15E-03	3.41E-03
	625	0.058	0.13	99.87	23.15	1.70E-02	1.26E-03
	1250	0.02	0.04	99.96	46.30	3.40E-02	4.35E-04
	2500	0.012	0.03	99.97	92.59	6.79E-02	2.61E-04
Cu	10	0.12	0.11	99.89	0.16	1.15E-04	1.11E-03
	15	0.24	0.22	99.78	0.24	1.73E-04	2.22E-03
	20	0.32	0.3	99.7	0.31	2.31E-04	2.96E-03
	100	0.6	0.55	99.45	1.57	1.16E-03	5.57E-03
	250	1.6	1.48	98.52	3.93	2.89E-03	1.50E-02
	500	3	2.77	97.23	7.87	5.77E-03	2.85E-02
Co	10	0.22	0.22	99.78	0.17	1.24E-04	2.20E-03
	20	0.26	0.26	99.74	0.34	2.49E-04	2.60E-03
	50	0.4	0.4	99.6	0.85	6.22E-04	4.00E-03
	100	0.8	0.8	99.2	1.70	1.25E-03	8.03E-03
	250	1.68	1.67	98.33	4.24	3.11E-03	1.70E-02
	500	3.4	3.39	96.61	8.48	6.23E-03	3.50E-02
Cr	10	0.005	0.01	99.99	0.19	1.41E-04	5.60E-05
	20	0.012	0.01	99.99	0.38	2.82E-04	1.34E-04
	50	0.025	0.03	99.97	0.96	7.05E-04	2.80E-04
	80	0.045	0.05	99.95	1.54	1.13E-03	5.04E-04
	100	0.0645	0.07	99.93	1.92	1.41E-03	7.23E-04

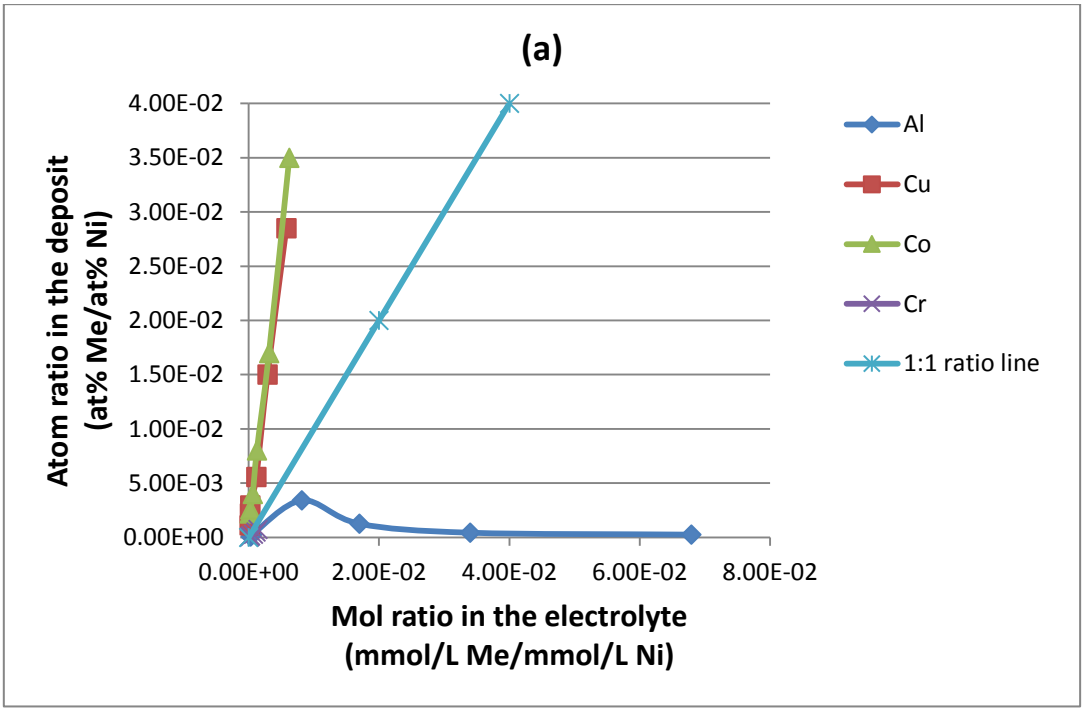

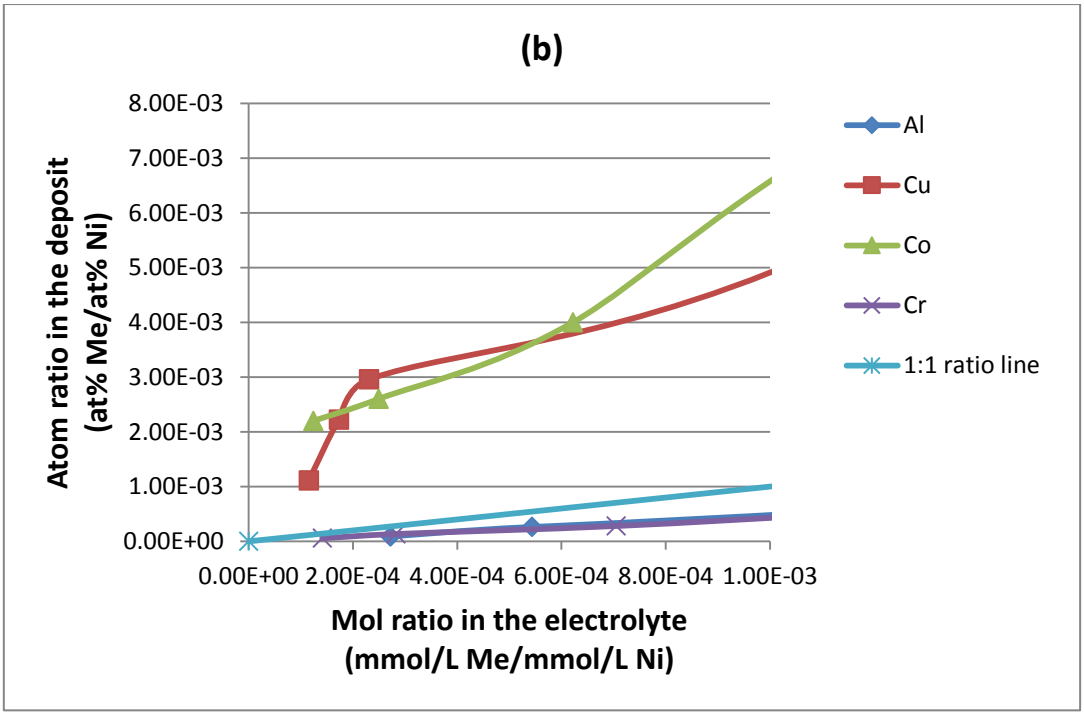

Figure 4.8. Chemical compositions of the nickel deposits as a function of impurity concentration in the electrolytes (a), detail at lower concentrations (b).

4.6 Current efficiency

The current efficiency calculated from the actual nickel deposit mass obtained from the deposited mass and the nickel atom percent (m%) from chemical analysis results, and the theoretical nickel deposit mass calculated using Faraday's law, was found to be about 90% for impurity-free electrolyte, which is relatively low compared with typical current efficiencies of 92 to 97% reported for practical plants (Schlesinger and Paunovic, 2010; Holm and O'Keefe, 2000; Ji, 1994). The effect of impurities in the electrolyte on the current efficiency of nickel plating is shown in Figure 4.9, indicating that the current efficiency is more sensitive to the aluminium and chromium compared with copper and cobalt impurities. Side reactions, which include hydrogen and impurity ion reduction at the cathode surface, are generally the main causes of current efficiency drops in electrowinning. The contribution of hydrogen reduction to reduce the current efficiency to around 90% in the absence of impurities is expected to remain almost constant in the case of this work because all the impurities investigated are not known hydrogen-reduction catalysts relative to nickel. Therefore, the drop of current efficiency seems not to be mainly due to hydrogen reduction.

Alternatively, the drop in current efficiency in nickel electroplating could have been due to the inhibition of nickel plating in the presence of the impurities, by, for instance, forming metal hydroxyl species at the surface of the cathode that could have prevented nickel plating, provided that hydrogen deposition was not similarly affected. In the latter case, it is difficult to determine the fraction of charge flow that hydroxyl species might have hindered at some active sites because their formation would not have involved charge flow but rather a change of pH level. However, precipitate formation is not deemed likely for the impurities investigated in this work under the buffered bulk conditions used, even for chromium and aluminium impurities as also shown further in EDS results in Section 4.8, in contrast to the work of Mohanty et al. (2005). The observed drops in current efficiency in the presence of impurities in the electrolyte are thus likely related to their codeposition with nickel by either normal or anomalous mechanisms, or repeated surface underpotential plating of impurities and entrapment by subsequent nickel plating. A significant drop of current efficiency in the presence of low aluminium and chromium concentrations was also reported in the literature (Mohanty et al., 2005; O'Keefe and Holm, 2000).

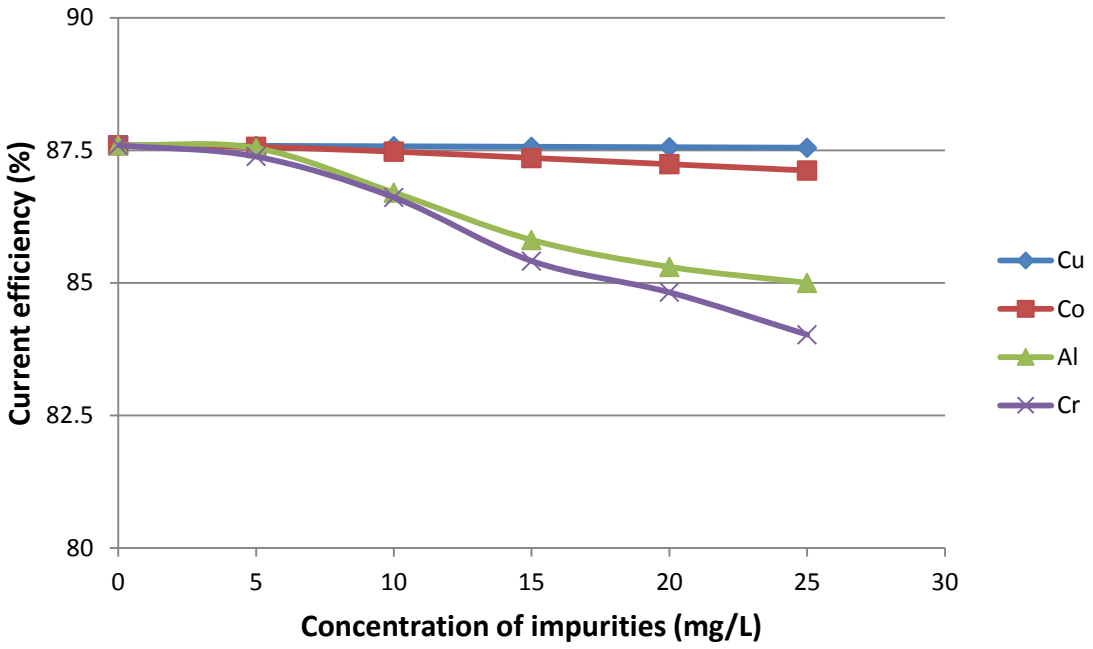

Figure 4.9. Influence of electrolyte impurities on the current efficiency of nickel plating.

4.7 Potentiodynamic polarisation curves

The probability of entrained precipitates was likely to be low, as follows from the absence of predominance indications at pH 3.5 on the E-pH diagrams in the range of concentration of 10^{-3} — 10^{-5} M in the electrolyte as mentioned in Section 2.2.1.2.7. The difference in pH between the bulk electrolyte and that close to the cathode surface was expected to be low because the electrolyte was buffered by boric acid probably through the formation of a nickel borate complex, as discussed in the same Section (Tilak et al., 1977; Yin and Lin, 1996; Gangasingh and Talbot, 1991). Nonetheless, the chemical analysis of deposits showed traces of aluminium and chromium, the reduction potentials of which are far more negative than the potential at which the nickel was plated. To further investigate the kinetics of the processes occurring at the cathode, potentiodynamic polarisation tests were carried out using electrolytes containing aluminium and chromium impurities.

The results shown in Figures 4.10 and 4.11 indicate that the potential at which nickel plating initiated in the presence of aluminium and chromium impurities in the electrolyte did not change significantly from that of an impurity-free nickel electrolyte; the rise in cathodic current started at around – 0.56 V vs Ag/AgCl for both aluminium- and chromium-containing electrolytes. This result seems to be consistent

with the deposition of only nickel in the very early stage of deposition, which may be accompanied by underpotential deposition of these impurities on the nickel deposit. A decrease of overpotentials at low levels of these impurities for a constant total charge flow at the cathode, which, when combined with the decrease of the mass of nickel in the presence of aluminium and chromium impurities, as indicated by the drop in current efficiency, might have been the result of either impurity codeposition with nickel or more hydrogen reduction at the electrode.

The mechanism by which aluminium and chromium influence the efficiency of nickel is not simple or well known. In view of the limited current that could have been generated by the deposition of the relatively small amount of the impurity metals, it is likely that the main effect of these were to favour hydrogen reduction relative to nickel deposition with a decrease of overpotential at low levels of these impurities. However, in the presence of aluminium at higher aluminium concentrations, where the effect of aluminium would have been reduced and the deposit structure would have tended to that of the pure nickel electrolyte, the reverse, i.e, a rise in overpotential (Figure 4.12), was observed. This increase in overpotential could also have resulted in higher current efficiencies, as reported in the literature (O'Keefe and Holm, 2000; Das and Gorgia, 1988), although this was not specifically investigated in the present work.

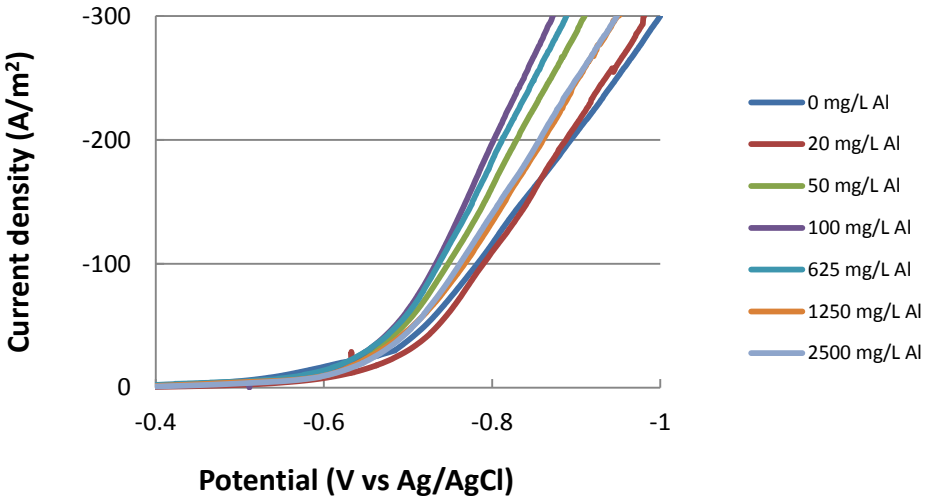

Figure 4.10. Potentiodynamic cathodic polarisation on titanium for a nickel sulfate electrolyte containing aluminium at the levels indicated.

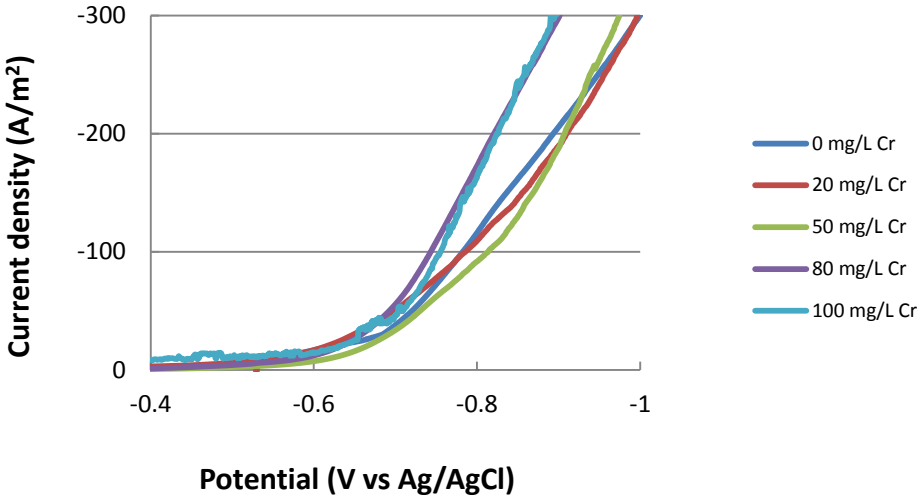

Figure 4.11. Potentiodynamic cathodic polarisation on titanium for a nickel sulfate electrolyte containing chromium at the levels indicated.

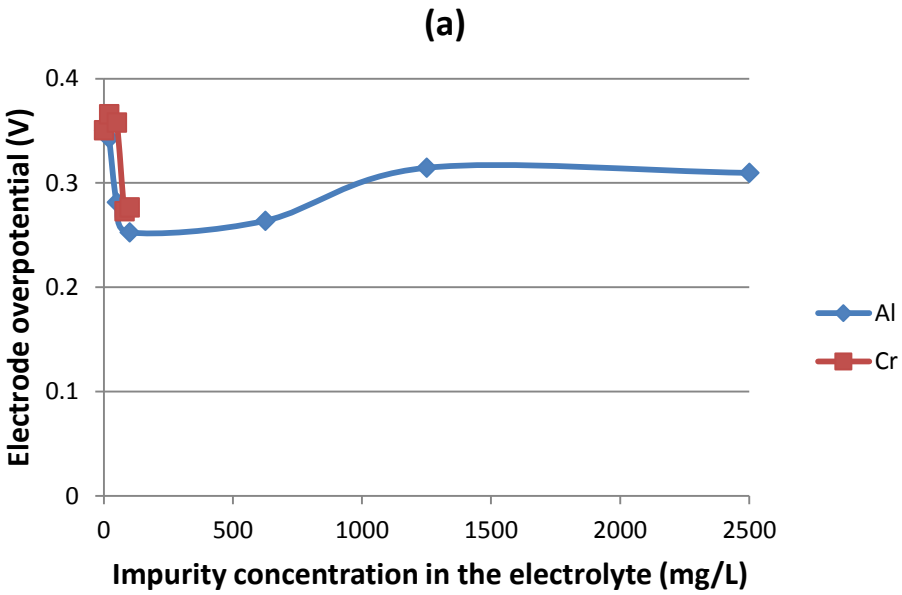

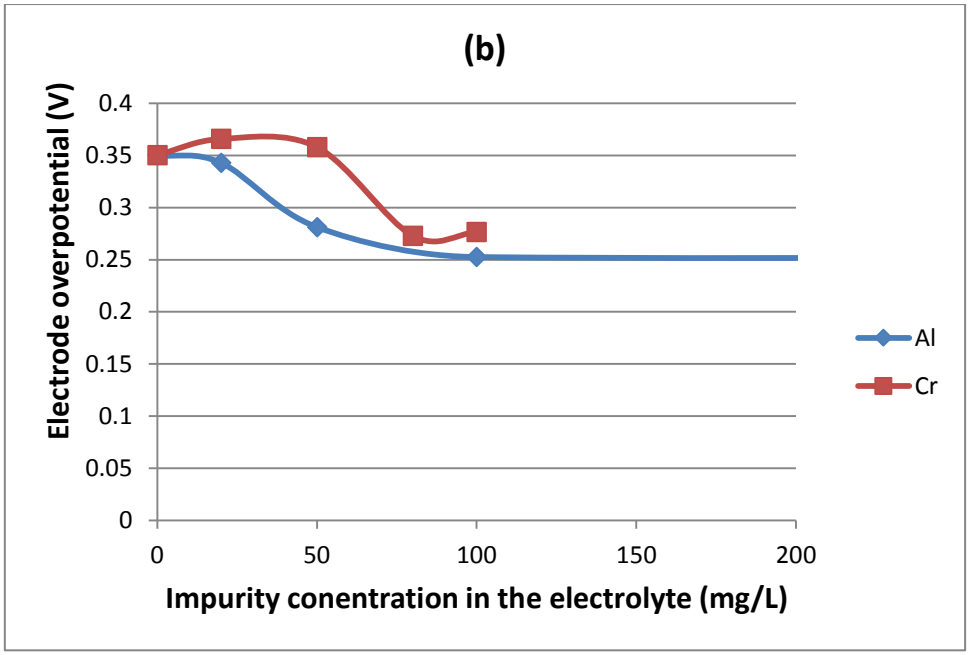

Figure 4.12. Influence of aluminium and chromium present in a nickel sulfate electrolyte on the cathodic overpotential on a titanium electrode polarized galvanostatically at 215 A/m^2 (a), detail at lower concentrations (b).

4.8 Energy-dispersive X-ray spectrometry analysis of the nickel deposits

In the absence of modifying agents, the possibility of some precipitate layer formation on the surface of nickel deposited from the aluminium impurity-containing electrolyte that could have caused the aluminium detected with qualitative analysis of the deposit, has been the subject of discussion in previous work (O'Keefe and Holm, 2000; Mohanty et al., 2005). O'Keefe and Holm (2000) proposed that such a layer might dissolve when the aluminium concentration in the electrolyte becomes very high, with resulting visually observable smoother deposits. In such case, aluminium should not report in the bulk of nickel deposit and the aluminium detected with the ICP analysis could have originated from these surface layers or residual aluminium containing electrolyte on the surface of the nickel. Unfortunately they did not chemically analyse the deposited nickel in their work. The work of Mohanty et al. (2005), which used boric acid as modifying agent, reported precipitate formation that might account for the traces of aluminium detected in the deposit. Unfortunately the pH and temperature used in their work were not reported. The present work showed that this is likely not the case under our working conditions, referring to the E-pH diagram and the range of impurities in the electrolyte and the pH of 3.5 used in presence of boric acid discussed in Section 2.2.1.2.7, combined with

the results relating to the current efficiency and potentiodynamic tests discussed in Sections 4.6 and 4.7, respectively. In order to establish that the traces of aluminium were indeed not from such precipitates or superficial layers that might contain oxygen, i.e., oxides or hydroxides, and that the impurities detected by ICP indeed originated from the bulk deposit, EDS-SEM analyses as a second analytical method were conducted on polished nickel deposits obtained from aluminium- and chromium-containing electrolytes. The sample volume of the EDS signal is such that the bulk composition rather than the surface would be characterised (Noran Instruments, 1999).

The results presented in Figures 4.13 and 4.14 show traces of aluminium and chromium impurities in the nickel deposit that compare with those from ICP-MS analysis, as shown in Table 4.4. Oxygen is a main element in the formation of oxides and hydroxides but was not detected. The trend for the impurity content in the EDS results was found to be similar to those obtained with ICP-MS. The aluminium in the nickel deposit was detected at intermediate concentrations but was found to be below the detection limit, considered to be around 1000 parts per million (mass basis), of the EDS technique for low as well as high aluminium concentrations. Chromium was not detected for nickel plated from electrolyte containing 80 mg/L but only at 100 mg/L chromium. Relatively large surface areas were considered to account for the impurity distribution in the deposit and selected spectra are presented to show the trend and range of impurity content, with the impurity concentrations being below the detection limit of the instrument for many samples. Copper- and cobalt-containing deposits were not analysed because the precipitation pH of these impurities on the relative E-pH diagrams (figures 2.4 and 2.5, recpectively), is clearly very far from pH 3.5 so that it is improbable that the traces of these impurities detected with ICP are from precipitates.

(a)

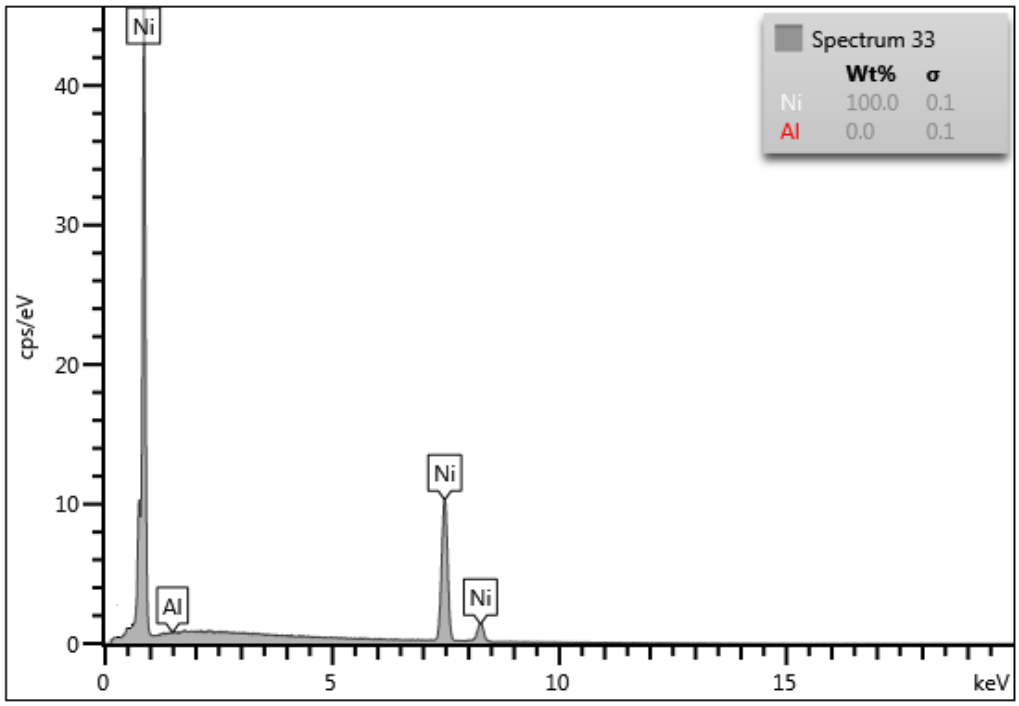
Spectrum 33
Wt% σ
Ni 100.0 0.1
Al 0.0 0.1
Ni
Al
Ni
Ni
cps/eV
0
10
20
30
40
0
5
10
15
keV

(b)

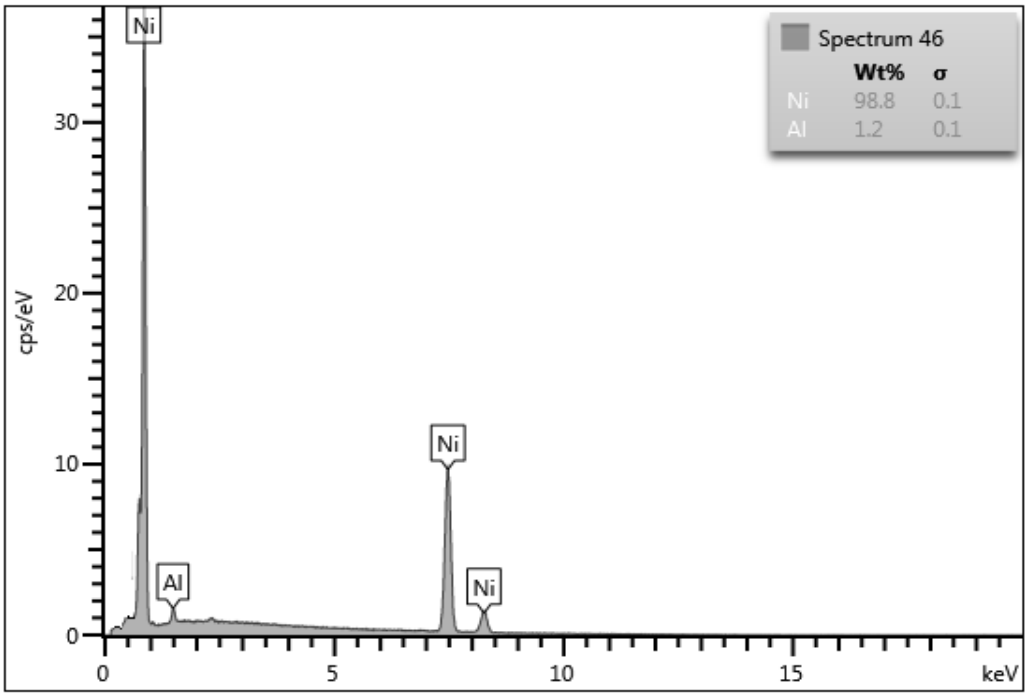
Spectrum 46
Wt% σ
Ni 98.8 0.1
Al 1.2 0.1
Ni
Al
Ni
Ni
cps/eV
0
10
20
30
0
5
10
15
keV

(c)

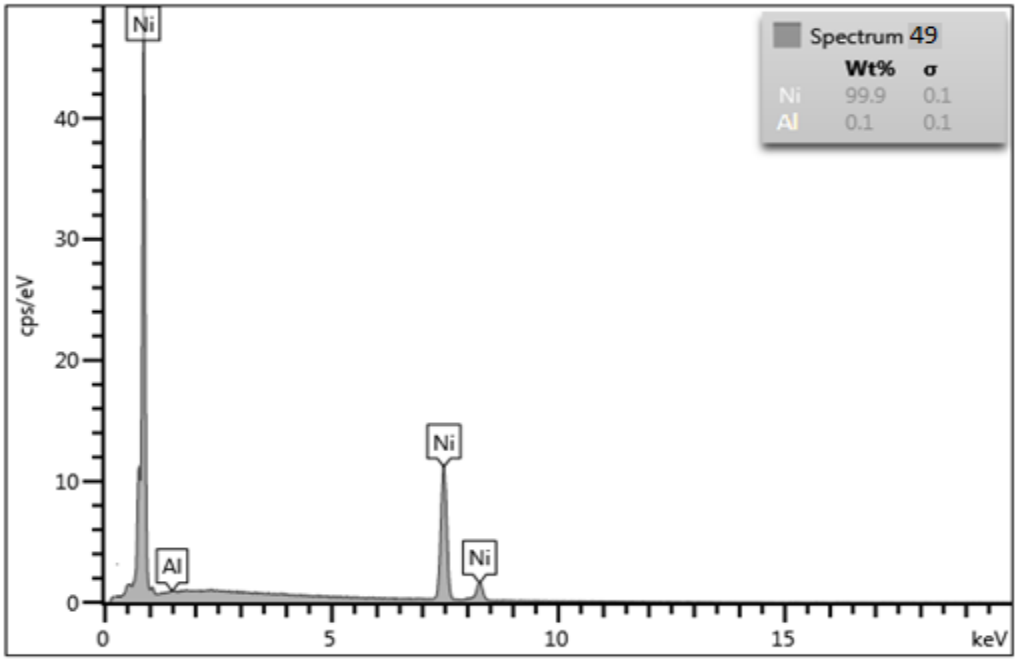

(d)

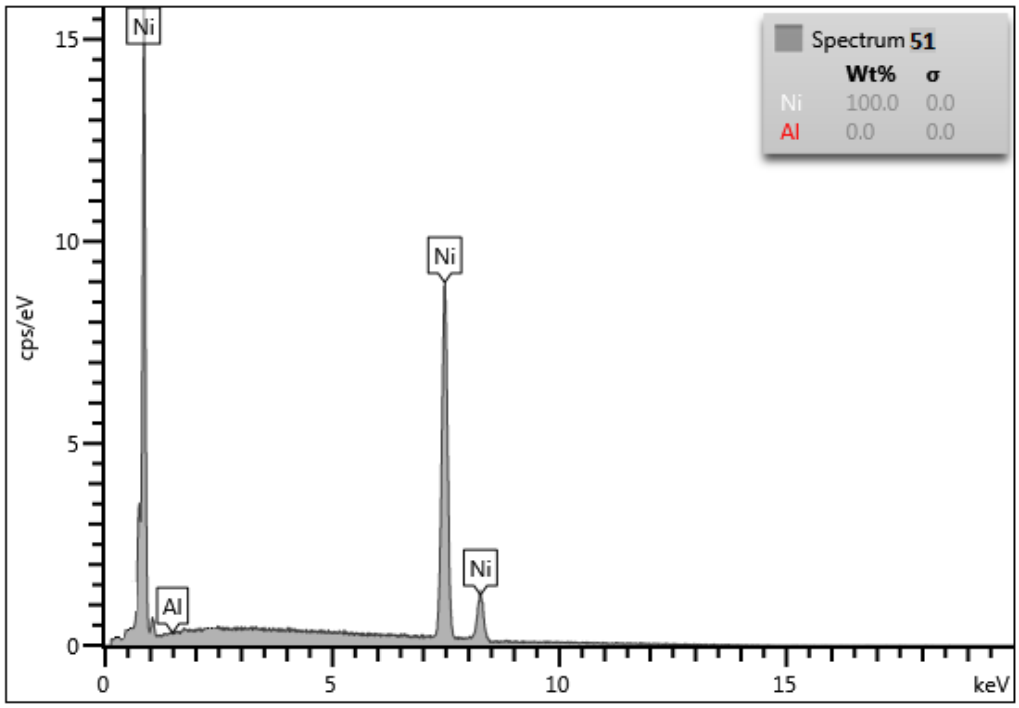

Figure 4.13. EDS spectra of nickel electrodeposited from aluminium-containing electrolytes: 20 mg/L Al (a), 300 mg/L Al (b), 625 mg/L Al (c), 2500 mg/L Al (d).

(e)

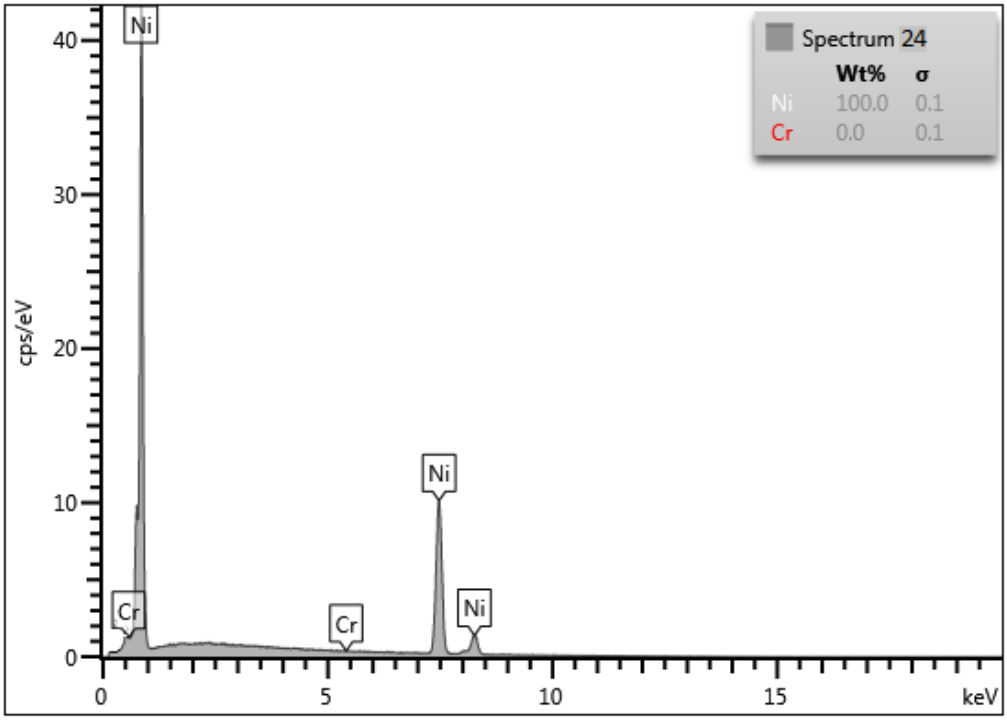

(f)

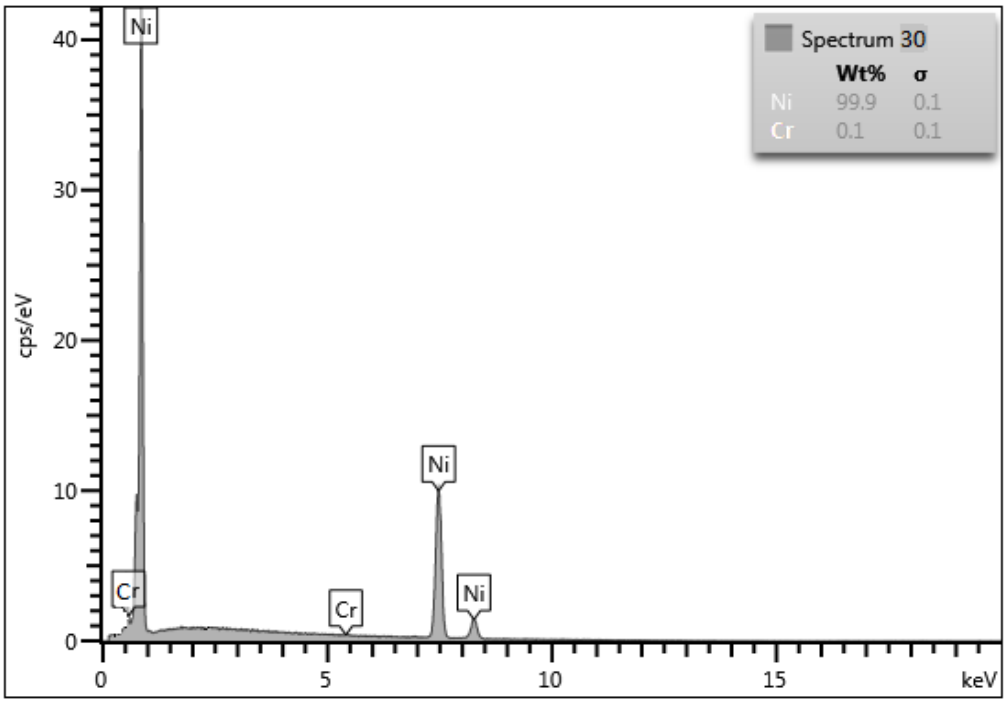

Figure 4.14. EDS spectra of nickel electrodeposited from chromium-containing electrolytes: 80 mg/L Cr (e), 100 mg/L Cr (f).

Table 4.4. Comparison of the trends indicated by EDS-SEM and ICP-MS results on nickel electrodeposited from aluminium- and chromium-containing electrolytes.

Impurity	Concentration in electrolyte (mg/L)	Impurity deposit content by EDS (mass %)	Impurity deposit content by ICP (mass %)
Aluminium	20	0.0	0.012
	300	1.2	1.56
	625	0.1	0.058
	2500	0.0	0.012
Chromium	80	0.0	0.045
	100	0.1	0.063

4.9 Relative adhesion strength of the nickel deposit to the titanium substrate as a function of impurity concentration in the electrolyte

A recent development in the electrowinning of nickel introduced the use of titanium as a permanent cathode substrate. Studies of the effects of impurities present in the electrolyte on the adhesion strength between the nickel deposit and the titanium substrate are almost absent in the literature. In the present work, the adhesion of the plated nickel to the titanium substrate was evaluated using standard adhesion tests for thin films on substrates. The results of the scratch tests described in Section 3.4 on the adhesion to the titanium substrate of nickel electroplated are presented as friction force as a function of loading curves for the metal plated from impurity-containing electrolytes in Figures 4.15 to 4.18, and also expressed in terms of calculated friction coefficients at separation as a function of impurity levels in the electrolytes in Figure 4.19. Appendice tables A4.1 to A4.4 contain the data used for the construction of these figures.

The scratch test results should be considered in the context of the idea to use these to quantify the qualitative visually observed effects of impurities on the quality of the plated nickel, as reported in Table 4.2. The visual observations indicated that both aluminium and chromium degraded the plated nickel at levels of 5 mg/L in the electrolyte, while copper and cobalt did not visually affect the coating up to levels of 20 mg/L. The friction coefficients at separation indicated in Figure 4.19 do not reflect these trends because aluminium and copper in the electrolyte caused significant reductions in the measured friction at separation, while chromium showed the least effect. The fact that the scratch technique could not detect the significant defects

that were visually observed is an indication that the technique will have to be refined to be useful in the present context. Moreover, the use of the term 'friction' in the scratch test context is unfortunate because the relative movement of the indenter to the coating is not predominantly a sliding movement typically associated with friction measurements, rather that of ploughing through the coating. The force associated with the indenter ploughing through the coating would, of course, be dependent on the normal force applied and the mechanical properties of the coating but such that it would be difficult to discern the degree of attachment of the coating to the substrate in a quantitatively meaningful way.

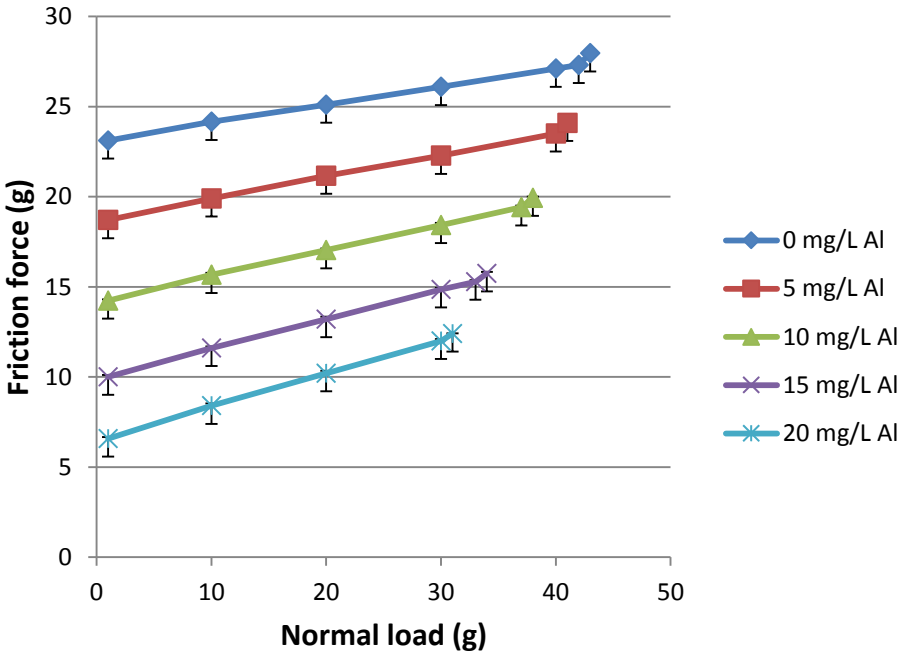

Figure 4.15. Friction force as a function of the normal load measured during scratch tests on nickel electroplated from nickel electrolytes containing the concentrations of aluminium indicated.

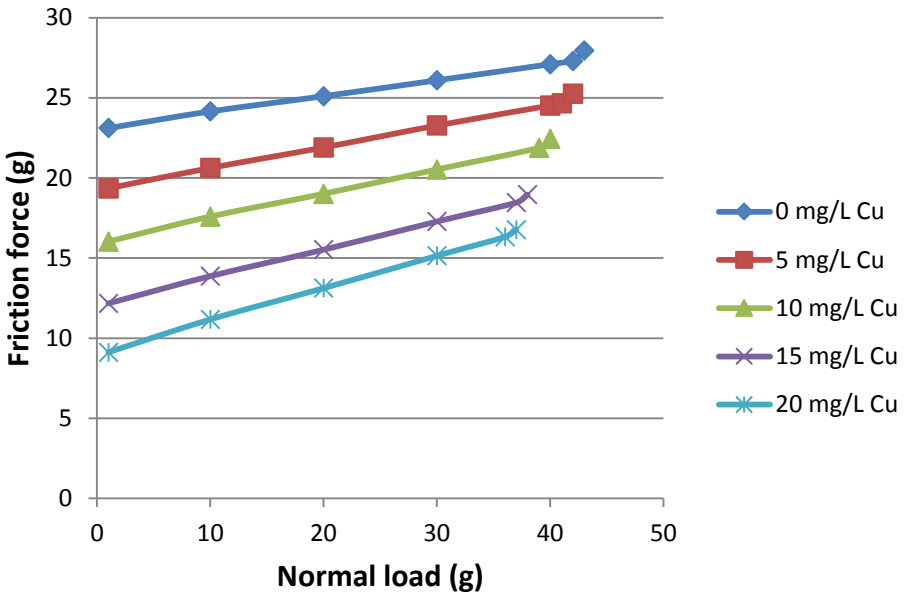

Figure 4.16. Friction force as a function of the normal load measured during scratch tests on nickel electroplated from nickel electrolytes containing the concentrations of copper indicated.

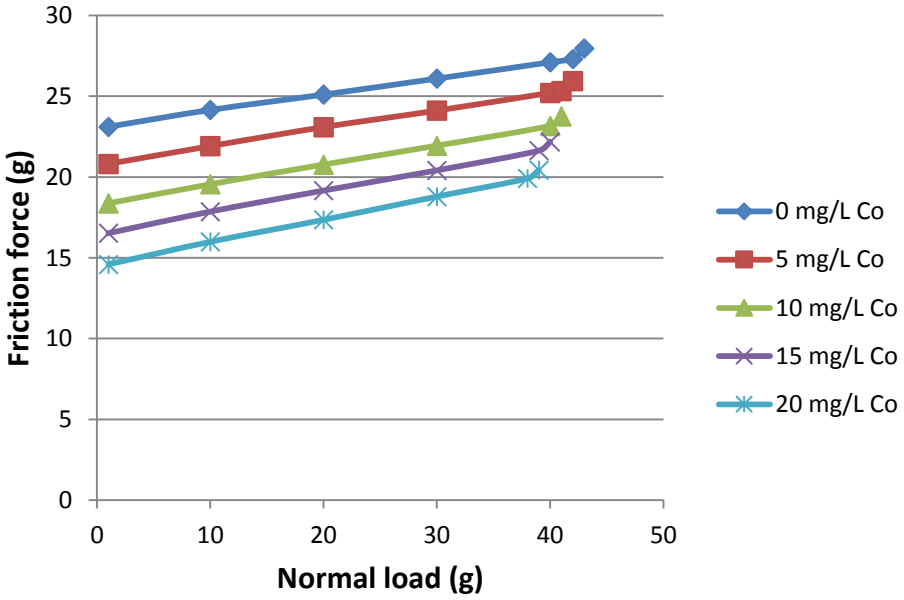

Figure 4.17. Friction force as a function of the normal load measured during scratch tests on nickel electroplated from nickel electrolytes containing the concentrations of cobalt indicated.

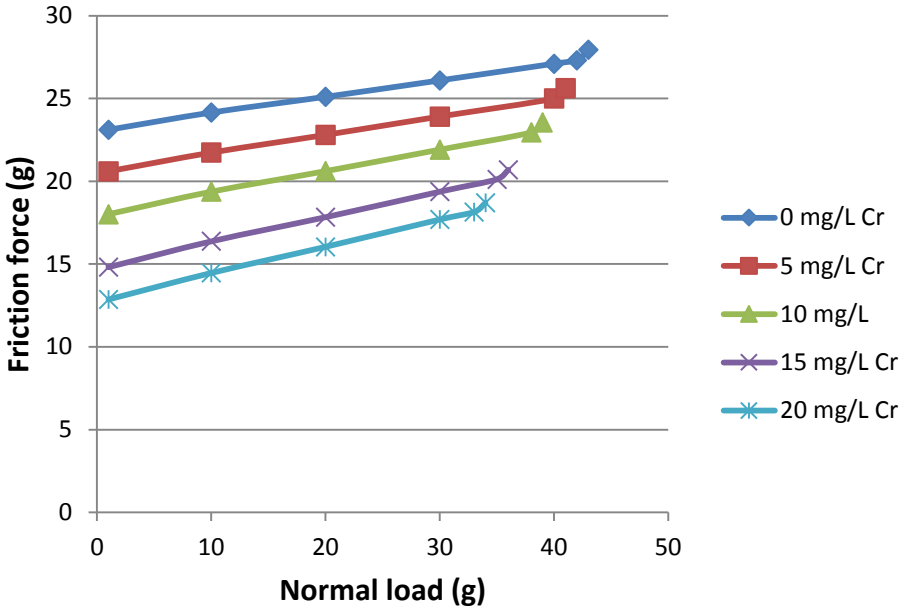

Figure 4.18. Friction force as a function of the normal load measured during scratch tests on nickel electroplated from nickel electrolytes containing the concentrations of chromium indicated.

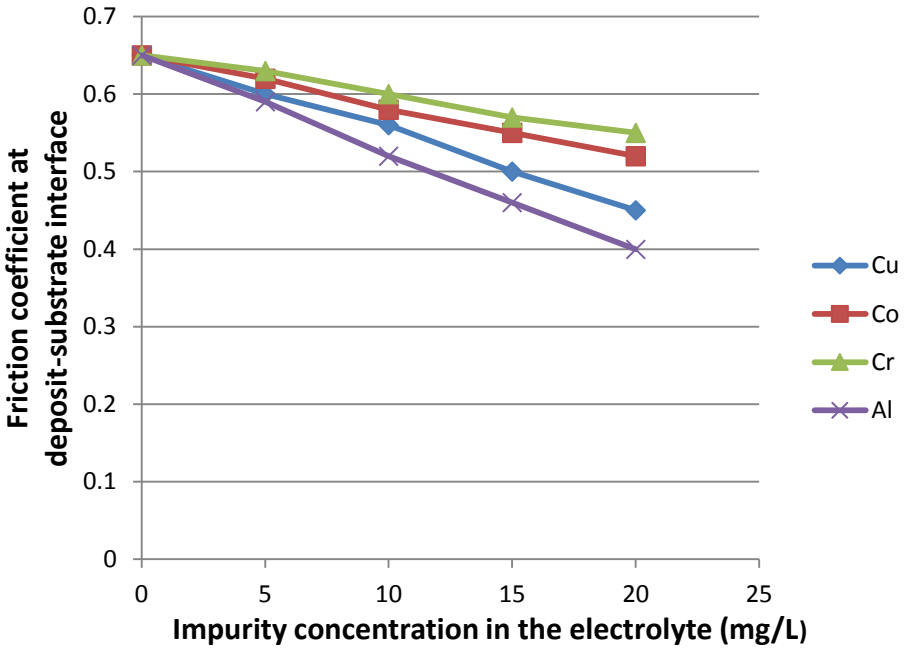

Figure 4.19. Friction coefficients at separation as a function of impurity concentration in the electrolyte for various impurities.

5. Conclusions

In this work, the influence of impurities added to an aqueous nickel sulfate electrolyte on the internal stresses developed in nickel electrodeposited on a titanium substrate, as well as the deposit morphology and adhesion to the substrate, were investigated using stress measurements, visual observations, chemical analyses, microstructural characterization and adhesion tests.

It was found that the stress in the nickel deposit increased with impurity concentration in the electrolyte for copper, chromium and cobalt impurities, with a slight decrease of stress at low cobalt concentrations, i.e., below 25 mg/L. High stresses were found at intermediate aluminium concentrations and lower stresses at both low and high aluminium concentrations in the electrolyte with associated smoother and more compact nickel deposits, as were also noted in the literature based on visual observations. The levels of internal stresses correlated well with the levels of impurities taken up in the nickel deposits.

The visually observed failure of the nickel plated on a stiff substrate correlated well with conditions for which the internal stress, calculated from deflection measurements on the flexible substrate, exceeded the predicted flow stress of the plated nickel, estimated from grain size measurements. Such measurements may thus be useful predictors for stress-related failures of electroplated nickel.

The current efficiency decreased in the presence of all the impurities investigated, most probably by normal and anomalous co-deposition with nickel for copper and cobalt, respectively. The conditions used in this work in terms of pH and impurity concentration range in the electrolyte, as well as with the added buffer, would not have favoured the precipitation of metal hydroxides. The absence of hydroxides in the plated nickel was confirmed by the absence of significant oxygen in the EDS analyses of nickel deposits containing aluminium and chromium. However, although aluminium and chromium are not hydrogen reduction catalysts, significant decreases in current efficiency were measured, as is also reported in the literature. It is proposed that the reduction in current efficiency is due to the inhibition of nickel plating by these impurities rather than increasing hydrogen evolution, although significant increases in the nucleation overpotential were not detected.

Mechanical failure of electroplated nickel is primarily driven by the high internal stresses that develop during plating, with failure depending on the ability of the material to resist the forces so generated by the strength of the material itself and by its bonding to the substrate. Visual observation of cracking and/or disbondment is a simple means to characterise such failures but only represent the end result when the ability of the material, as well as that of the bond to the substrate, to resist the internal forces are exceeded. An independently measure of the strength of the bond to the substrate would thus be of value, as was attempted in this work using scratch tests. The scratch test results, in the form of friction coefficients at separation, indicated that the adhesion was relatively weaker in the presence of aluminium in the electrolyte, followed by copper, cobalt and chromium, respectively. These results do not correlate with visual observations of the plated nickel, which indicated cracked or disbonded plated nickel at low impurity levels for both aluminium and chromium in the electrolyte, i.e., 10 mg/L, and only at higher levels for copper, i.e., 50 mg/L, and cobalt, i.e., 250 mg/L.

The present work thus indicated that the presence of low concentrations of impurities such as aluminium, copper and chromium in a sulfate electrolyte can significantly affect the characteristics of the electroplated nickel in terms of composition, mechanical properties and especially the internal stresses generated in such deposits. The influence of aluminium differs from that of the other impurities in the sense that, while the effects of copper and chromium saturated at higher concentrations, that of aluminium strongly diminished at higher concentrations such that at about 1 g/L in the electrolyte its effect on the plated nickel was minimal.

The practical implications of this work are clear, although it should be emphasized that the effect of the impurities was studied in isolation and that further work would be required to characterise the effect of the simultaneous presence of multiple impurities, as would more typically occur in practice.

6. References

Abdulaliyev, Z., Ataoglu, S. and Guney, D., Thermal stresses in butt-jointed thick plates from different materials, Journal of Welding Research, (86)7, 2007, pp. 201s-204s.

Allard, S., Metals: thermal and mechanical data, International Tables of Selected Constants, Chap.2, (16), 1969, pp. 243-281, Pergamon Press, United States.

Alrehaily, M., Joseph, J.M., Biesinger, M.C., Guzonas, D.A. and Wren, J.C., Gamma-radiolysis-assisted cobalt oxide nanoparticles formation, Physics-Chemistry, Physical Chemistry Chemical Physics, (15)3, 2013, pp. 1014-1024.

Anderson, M.W. and Cubilas, P., Synthesis mechanism: crystal growth and nucleation, Zeolites and Catalysis: Synthesis, Reactions and Applications, Chap. 1, 2010, pp. 1-56, Wiley, United States.

Angle, J., Nanoscratch testing of thin film on glass substrate, from Google: http//: www.nanovea.com/App-notes/ Thin films, 2010, pp. 1-11.

Armstrong, R.W., 60 years of Hall-Petch: past to present nanoscale connections, Materials Transactions, (55)1, 2014, pp. 2-12.

Armstrong, R.W., Hall-Petch analysis of dislocation pileups in thin material layers and in nanopolycrystals, Materials Research Society, (28)13, 2013, pp. 1792-1798.

Astley, D.J., Kinetic studies in electrocrystallisation of metals, Ph.D. thesis, 1968, University of Newcastle, Australia.

Auciello, O. and Krauss, A.R., In-situ Real-time Characterisation of Thin Films, Book, 2001, Wiley- Interscience Publication, United States.

Berg, R.W., Hjuler, H.A., Qingfeng, L. and Bjerrum, N.J., Influence of substrates on the electrochemical deposition and dissolution of aluminium in $NaAlCl_4$ melts, Journal of the Electrochemical Society, (138)3, 1991, pp 763-766.

Bernstein, I.M. and Thompson, A.W., Effect of hydrogen on behaviour of materials, Hydrogen Effects in Metals, Metallurgy Society of AIME, 1976, pp. 455-466.

Blees, M.H., Winkelman, G.B., Balkenende, A.R. and den Toonder, J.M.J., The effect of friction on scratch adhesion testing: Application to a sol-gel coating on polypropylene, Thin Solid Films, (359)1, 2000, pp. 1-13.

Brahmajirao, V., Rajarao, N.S.S.V. and Sarma, A.V., Studies on ion-solvent interaction of electrolyte solutions – Part 3: Activity coefficient studies of 2-2 electrolytes, International Journal of Science and Technology, (1)10, 2012, pp. 1-15.

Brinson, H. F. and Brinson, L.C., Stress and strain analysis and measurement, Polymer Engineering Science and Viscoelasticity: An introduction, Chap. 2, 2015, pp. 15- 55, Springer, United States.

Brown, H.T., and Mason, P.G., Electrowinning of nickel at Bindura Smelting and Refining Company, Journal of the Southern Africa Institute of Mining and Metallurgy, (77)7, 1977, pp. 143-145.

Butler, D.W., Stoddart, C.T.H. and Stuart, P.R., The stylus or scratch method for thin film adhesion measurement: Some observations and comments, Journal of Applied Physics, (3)6, 1970, pp. 877-883.

Callister, W.D., Material Science and Engineering: An introduction, 7th edition, 2007, pp. 1-975, Wiley, United States.

Carlton, C.E. and Ferreira, P.J., What is behind the inverse Hall-Petch effect in nanocrystalline materials? Acta Materialia, (55)11, 2007, pp. 3749-3756.

Chason, E., Measurement of stress evolution in thin films using real-time in-situ wafer curvature, note, 2013, pp. 1-35, Brown University, United States.

Christina, V., G.D.S., Antonio, P.A.S., Dragunski, D.C., Peraro, D.N.C., Tarley, C.R.T. and Caetano, J., Highly improved chromium III uptake capacity in modified sugarcane bagasse using different chemical treatment, Quimica Nova, (35)8, 2012, pp. 1606-1611.

Coghill, M.D.E. and St. John, D.H., Scratch adhesion testing of soft metallic coatings on glass, Surface and Coatings Technology, (41)2, 1990, pp. 135-146.

Corbett, C. B. and Hoyt, J.J., Modelling the effect s of impurities on microstructure formation in nanocrystalline nickel thin films, Journal of Materials, (57)9, 2005, pp. 71-73.

Cree, A.M., Hainsworth, S.V. and Weidmann, G.W., A strain-energy method for determining residual stresses in anodized thin films, Transactions of the Institute of Metal Finishing, (84)5, 2006, pp. 246-251.

Crundwell, F., Moats, M., Ramachandran, V., Robinson, T. and Davenport, W.G., Extractive Metallurgy of Nickel, Cobalt and Platinum Group Metals, 2011, pp. 1-535, Elsevier Science & Technology, United Kingdom.

Cuppett , J.D., Duncan, S.E. and Dietrich, A.M., Evaluation of copper speciation and water quality factors that affect aqueous copper tasting response, Chemical Senses, (31)7, 2006, pp. 689-697.

Das, S.C. and Gogia, S.K., The effect of Co^{2+}, Cu^{2+}, Fe^{2+} and Fe^{3+} during electrowinning of nickel, Journal of Applied Electrochemistry, (21)1,1991, pp. 64-72.

Das, S.C. and Gogia, S.K., The effect of Mg^{2+}, Mn^{2+}, Zn^{2+} and Al^{3+} on the nickel deposit during electrowinning from sulfate bath, Metallurgical Transaction B, (19)6, 1988, pp. 823-830.

Davalos, C.E., Lopez, J.R., Ruiz, H., Mendez, A., Antonio-Lopez, R. and Trejo, G., Study of the role of boric acid during the electrochemical deposition of Ni in a sulfamate bath, International Journal of Electrochemical Science, (8)7, 2013, pp. 9785-9800.

Davis, J.R., Nickel, Cobalt and their Alloys, 2000, pp. 1-425, ASM Speciality Handbook, Netherlands.

Deni, R.M., The effect of addition agents on cathode overpotential and cathode quality in copper electrowinning, Master's thesis, 1994, Laurentian University, Canada.

Dong, L., Schnitker, J., Smith, R.W. and Srolovitz, D.J., Stress relaxation and misfit dislocation nucleation in the growth of misfitting films: A molecular dynamics simulation study, Journal of Applied Physics, (83)1, 1998, pp. 217-227.

Dual, J., Simons, G., Villain, J., Vollmann, J. and Weippert, C., Mechanical properties of MEMS structures, ICEM 12, 12th International Conference on Experimental Mechanics, 2004, pp. 1-8, Politecnico di Bari, Italy.

Eastman, J., Matsumoto, T., Narita, N., Heubaum, F. and Birnbaum, H.K., Hydrogen effects in hydrogen-embrittlement or enhanced ductility, Technical Report ADA094271, 1980, pp. A-L, University of Illinois, Urbana.

Epelboin, I., Jousselline, M. and Wiart, R., Impedance measurement for nickel deposition in sulfate and chloride electrolytes, Journal of Electroanalytical Chemistry, (119)1, 1981, pp. 61-71.

Fan, C. and Piron, D.L., Study of anomalous nickel-cobalt electrodeposition with different electrolytes and current densities, Electrochimica Acta, (41)10, 1996, pp. 1713-1719.

Floro, J.A. and Chason, E., Curvature-based techniques for real-time stress measurement during thin film growth, Sandia National Laboratories, Albuquerque, NM 87185-1415, 1998, pp.1-34.

Freund, L.B. and Suresh, S., Thin film materials: stress, defect formation and surface evolution, AIAA Journal, (43)4, 2005, pp. 922-923.

Gangasingh, D. and Talbot, B., Anomalous electrodeposition of nickel-iron, Journal of The Electrochemical Society, (138)12, 1991, pp. 3605-3611.

Garrido, J.A., Electron transfer at electrode-solution interface, Biosensors and Bioelectronics I, note, 2009, pp. 1-21.

Giallonardo, J.D., Structure and properties of electrodeposited nanocrystalline nickel and nickel-iron alloy continuous foils, Ph.D. thesis, 2013, University of Toronto, Canada.

Goods, S.H., Kelly, J.J., Talin, A.A., Watson, R. and Michael, J.R., Electrodeposition of nickel from low temperature sulfamate electrolyte, Part II: Properties and structure of electrodeposits, Journal of The Electrochemical Society, (153)5, 2006, C325-C331.

Habashi, F., Texbook of Hydrometallurgy, 2th edition, 1999, Laval University, Canada.

Hafner, B., Energy Dispersive Spectroscopy on SEM: A primer, Characterisation Facility, note, University of Minnesota, 2014, pp. 1-26.

Haluzan, D., Microwave LIG-MEMS variable capacitors, Master's thesis, 2004, University of Saskatchewan, Canada.

Hesegawa, M. and Fukutomi, H., Microstructural study on dynamic recrystallisation and texture formation in pure nickel, Materials Transactions, (43)5, 2002, pp. 1183-1190.

Hessani, S., A mathematical model of codeposition of nickel-iron on rotating disc electrode, Journal of The Electrochemical Society, (136)12, 1989, pp. 3611-3616.

Higashi, K. and Uesugi, T., Modelling solid solution strengthening using first-principles results of misfit strain with Friedel model in Al-based alloys, Proceedings of the 12th International Conference on Aluminium Alloys, 2010, pp. 1412-1425.The Japan Institute of Light Metals, Japan.

Hinz, K., Altmaier, M., Gaona, X., Rabung, T., Schild, D., Richmann, M., Reed, D., Alekseevcd, E.V. and Geckeisa, H., Interaction of Nd(III) and Cm(III) with borate in dilute to concentrated alkaline NaCl, $MgCl_2$ and $CaCl_2$ solutions: Solubility and TRLFS studies, New Journal of Chemistry, (39)2, 2015, pp. 849-859.

Holm, M. and O'Keefe, T.J., Electrolyte parameter effects in the electrowinning of nickel from sulfate electrolytes, Minerals Engineering, (13)2, 2000, pp. 193-204.

Hong-Xian, X., Bo, L., Fu-Xing, Y. and Toa, Y., Effect of grain boundary sliding on toughness of ultrafine grain structure steel: A molecular dynamics simulation study, Chinese Physics B, (22)1, 2013, pp. 1-8.

Huerta Garrido, M.E., Experimental and mechanistic study of copper electrodeposition in the absence and presence of chloride ions and polyethylene glycol, Ph.D. thesis, 2007, University of Waterloo, Canada.

Ivetic, G., Lanciotti, A. and Polese, C., Electric strain gauge measurement of residual stress in welded panels, Journal of Strain Analysis for Engineering Design, (44)1, 2009, pp. 117-126.

Ji, J., Fundamental aspects of nickel electrowinning from chloride electrolytes, Ph.D. thesis, 1994, University of British Columbia, Canada.

Jing, L.U., Yang, Q.H. and Zhang, Z., Effects of additives on nickel electrowinning from sulfate system, Transaction of Nonferrous Metals Society of China, (20), 2010, pp. 97-101.

Jorge, R.M.N., Campos, J.C.R., Tavares, J.M.R.S., Vaz, M.A.P. and Santos, S.M., Analysis of a bar-implant use a meshless method, Biodental Engineering II, 2014, pp. 142, Taylor and FrancisGroup, United Kingdom.

Jovicevic, J.N. and Bewick, A., A study of initial stages of the electrochemical deposition of metals on foreign substrates: Lead and thallium on copper and silver surfaces, Physics, Chemistry and Technology, (3)2, 2005, pp. 183-203.

Kelly, A., Brown, L.M. and Ham, R.K., Strengthening mechanisms in crystals, from Google: academic.uprm.edu/Courses/MechMet, 1971, pp. 9-70.

Kittelty, D., The electrocrystallization of nickel and its relationship with the physical properties of the metal, Ph.D. thesis, Murdoch University, 2002.

Kopeliovich, D., Nickel electroplating, Substances and Technology, from Google: http://www.substech.com/ dokuwiki doku.php? id = Nickel-electroplating, 2013.

Kovaleva, M., Kolpakov, A., Poplavsky, A., and Sirota, A., Effect of ion surface treatment of NiTi on adhesion strength of nanoscale coating obtained by the pulsed vacuum-arc technique, 18th International Conference of Composite Materials, 2008, pp. 1-4, Joint Research Center, Belgorod State University, Russia.

Kovaleva, M.G., Arseenko, M.Y., Prozorova, M.C. and Tyurin, Y.N., Properties of titanium power coatings deposited on a substrate of steel-1030, Nanomaterials: Application and Properties, (1)Part II, 2011, pp. 369-372.

Kubin, L.P. and Devincre, B., From dislocation mechanisms to dislocation microstructures and strain hardening, LEM, CNRS-ONERA, 29 Av. de la Division Leclerc BP 72, 92322 Châtillon Cedex, France, 2000, pp. 1-21.

Kuiry, S., Advanced scratch testing for evaluation of coating, Tribology and Mechanical Testing, Bruker note, 2012, pp. 1-36, United States.

Kutilek, P. and Miksovky, J., The procedure of evaluating the practical adhesion strength of new biocompatible nano- and micro-thin films in accordance with international standards, Acta of Bioengineering and Biomechanics, (13)3, 2011, pp. 87-94.

Li, D., Understanding coating failures using scratch testing, Nanovea Mechanical Testers note, from google: nanovea.com/App-notes/Coating-failure-scratch, 2013, pp. 1-10.

Liu, R., Duay, J. and Lee, S.B., Heterogenous nanostructured electrode materials for electrochemical energy storage, Chemical Communications, (47)5, 2011, pp. 1384-1404.

Luo, J.K., Pritschow, M., Flewitt, A.J., Spearing, S.M., Fleck, N.A. and Milne, W.I., Effects of process conditions on properties of electroplated nickel thin films for micro-system applications, Journal of The Electrochemical Society, (153)10, 2006, pp. 155-161.

Lupi, C., Pasquali, M. and Dell'Era, A., Studies concerning nickel electrowinning from acidic and alkaline electrolytes, Minerals Engineering, (19), 2006, pp. 1246-1250.

Majolaine, K.D., Adhesion characterisation of hard coatings by scratch test, Master's thesis, Queen's University, 1999.

Mehregany, M. and Roy, S., Introduction to MEMS, Micro-engineering Aerospace Systems, 1999, pp. 1-28, The Aerospace Press, United States.

Mittal, R., Strengthening mechanism of metals, National Institute of Technology Rourkela, Metallurgy and Material Engineering, Roll No 10604038, 2009, pp. 1-9.

Miyazaki, S., Fu, Y.Q. and Huang, W.M., Thin film shape memory alloys: Fundamental and device applications, 2009, pp. 1-457, Cambridge University Press, United State.

Mohanty, U.S., Tripathy, B.C., Singh, P., Das, S.C. and Misra, V.N., Electrodeposition of nickel in the presence of Al^{3+} from sulfate baths, Journal of Applied Electrochemistry, (35)6, 2005, pp. 545-549.

Moharana, M., Mapping of structure and properties evolved during sono-electroplating of nickel thin films, Master's thesis, 2009, National Institute of Technology Rourkela, India.

Morris, D.G., The origins of strengthening in nanostructured metals and alloys, Revista de Metalurgia, (46)2, 2010, pp. 173-186.

Murakami, T., Sahara, R., Harako, D., Akiba, M., Narushima T. and Ouchi, C., The effect of solute elements on hardness and grain size in platinum based binary alloys, Materials Transactions, (49)3, 2008, pp. 538-547.

Nicol, M.J. and Kittelty, D., The electrocrystallization of nickel and its relationship with the physical properties of the metal, electrometallurgy 2001, eds, Dtrizac, J.E., Kelsall, G.H., Gonzalez, J.A., Montreal, Quebec: CIM, 2001, pp. 361-373.

Noran Instruments, Energy Dispersive X-Ray Microanalysis: An Introduction, Middleton, 1999, United States.

O'Keefe, T.J. and Holm, M., The anomalous behaviour of Al^{3+} in nickel electrowinning from sulfate electrolytes, Metallurgical and Materials Transactions B, (31)6, 2000, pp. 1203-1211.

Ouyang, L. Z., Crystal structure of metals, South China University of Technology, Materials for Mechanical and Engineering, 2009, pp. 2-94.

Overmeere, Q.V., Vanhumbeeck, J.F. and Proost, J., On the use of a multiple beam optical sensor for in-situ curvature monitoring in liquids, Review of Scientific Instruments, (81)4, 2010, pp. 1-10.

Panda, A., Electrodeposition of nickel-copper alloys and nickel-copper-alumina nano-composites into deep recesses for MEMS, Ph.D. thesis, 2003, Anna University, India.

Parkinson, R., Electroforming - a unique metal fabrication process, NiDl Technique series, No 10084, 2009, pp. 1-15, Nickel Development Institute, Canada.

Pathak, S., Guinard, M., Vernooij, G.C., Cousin, B., Wang, Z., Michler, J., and Philippe, L., Influence of lower current densities on the residual stress and structure of thick nickel electrodeposits, Surface and Coatings Technology, (205)12, 2011, pp. 3651-3657.

Pavlides, A.G., Developments in cobalt and nickel electrowinning technology, Bateman Engineering, Retrived from http:// www.bateman.com/papers/Ni%/EW, December/2012.

Pharr, M., Suo, Z. and Vlassak, J.J., Measurement of the fracture energy of lithiated silicon electrodes of Li-ion batteries, Nano Letters 13, 2013, pp. 5570-5577.

Pokluda, J. and Sandera, P., Micromechanisms of fracture and fatigue: in a multi-scale context, Fatigue Fracture - Technology and Engineering, Chap. 2, 2010, pp. 69-98, Springer, United States.

Proville, L. and Patinet, S., Depinning transition for a screw dislocation in a model solid solution, Physical Review B, (78)10, 2008, pp. 1-9.

Pruit, L.A. and Chakravartula, A.M., Mechanics of Biomaterials: Fundamental Principles for Implant Design, 2011, pp. 1-681, Cambridge University Press, United Kingdom.

Ritchie, R.O., Mechanisms of fatigue-crack propagation in ductile and brittle solids, International Journal of Fracture, (100)1, 1999, pp. 55-83.

Rosakis, A.J., Huang, Y., Jiang, H. and Ngo, D., The effect of thin film/substrate radii on Stoney formula for thin film/substrate subjected to non-uniform axisymmetric misfit strain and temperature, Journal of Mechanics of Materials and Structures, (1)6, 2006, pp. 1-14.

RSR anonodes, For electrorefining and electrowinning, retrieved from October 2017, from http:// http://www.rsranodes.com/pdf/Company_Brochure_English.pdf, 2017.

Rossini, N.S., Dassisti, M., Benyounis, K.Y. and Olabi, A.G., Method of measuring residual stress in components, Material and Design, (35), 2012, pp. 572-588.

Sander, D., Enders, A. and Kirschner, J., A simple technique to measure stress in ultrathin films during growth, Review of Scientific Instruments, (66)9, 1995, pp. 4734-4735.

Sander, D., Meyerheim, H., Ferrer, S. and Kirschner, J., Stress, strain, magnetic anisotropy: All is different in nanometer thin films, Advances in Solid State Physics, (43), 2003, pp. 547-561.

Santana, A.I.C., Diaz, S.L., Barcia, O.E. and Mattos, O.R., A kinetic study on nickel electrodeposition from sulfate acid solutions, Journal of the Electrochemical Society, (156)8, 2009, pp. 326-330.

Schlesinger, M. and Paunovic, M., Electrodeposition of nickel, Modern Electroplating, 5th edition, Chap. 3, 2010, pp. 79-114, Wiley, United States.

Schwartz, M., Deposition from aqueous solutions: An overview, Handbook of Deposition Technologies for Films and Coatings – Science, Technology and Application, Chap. 10, 1994, pp. 506-616.

Schweitzer, G.K. and Pesterfield L.L., The Aqueous Chemistry of the Elements, 2010, pp. 156-371, Oxford University Press, United Kingdom.

Secor, E.D., A constant-depth scratch test for the measurement of adhesion at film-substrate interfaces, Master's thesis, Naval Post-graduate School, Monterey, California, 1994.

Sergici, A.O. and Randal, N.X., Scratch testing of coatings, Advanced Materials & Processes, April 2006, pp. 41-43.

Sethuraman, V.A., Nguyen, A., Chon, M.J., Nadimpalli, S.P.V., Wang, H., Abraham, D.P., Bower, A.F., Shenoy, V.B. and Guduru, P.R., Stress evolution in composite silicon electrodes during lithiation/delithiation, Journal of The Electrochemical Society, (160)4, 2013, pp. 739-746.

Shaw, L.L., Ortiz, A.L. and Villegas, J.C., Hall-Petch relationship in a nanotwinned nickel alloy, Scripta Materialia, (51)8, 2004, pp. 801-806.

Smith, R.M., Orinakova, R., Turonova, A., Kladekova, D. and Galova, M., Recent developments in the electrodeposition of nickel and some nickel-based alloys, Journal of Applied Electrochemistry, (36)9, 2006, pp. 957-972.

Soboyejo, W.O., Bucheit, T. and Allameh, J.L., An investigation of the effects of thickness on mechanical properties of LIGA nickel MEMS structures, Journal of Materials Science (38)20, 2003, pp. 4129-4135.

Socha, V., Kutilek, P. and Viteckova, S., The evaluation of the practical adhesion strength of biocompatible thin films by fuzzy logic expert system and international standards, Journal of Electrical Engineering, (64)6, 2013, pp. 354-360.

Sofronis, P., Liang, Y. and Aravas, N., Hydrogen induced shear localization of plastic flow in metals and alloys, European Journal of Mechanics-A/Solid, (20)6, 2001, pp. 857-872.

Stein, B., A practical guide to understanding, measuring and controlling stress in electroformed metals, AESF Electroforming Symposium, 1996, pp. 1-7, Rochester, United States.

Steinmann, P.A., Tardy, Y. and Hintermann, H.E., Adhesion testing by the scratch test method: The influence of intrinsic and extrinsic parameters on the critical load, Thin Solid Films, (154)1-2, 1987, pp. 333-349.

Sukhorukov, S. and Loset, S., Friction of sea ice on sea ice, Elsevier, Cold Regions Science and Technology, (94), 2013, pp. 1-12.

Supicova, M., Rozik, R., Tenkova, L., Orinakova, R. and Galova, M., Influence of boric acid on the electrochemical deposition of nickel, Journal of Solid State Electrochemistry, (10)2, 2006, pp. 61-68.

Surviliene, S., Cesuniene, A., Selskis, A. and Butkiene, R., Effect of Cr (III) + Ni (II) solution chemistry on electrodeposition of CrNi alloys from aqueous oxalate and glycine baths, Transactions of the Institute Metal Finishing, (91)1, 2013, pp. 24-31.

Thorsten, C., Chemistry of borate-boric acid buffer system, CR Scientific LLC, Web. March 2013, http://www.crscientific.com/experiment4.html.

Tilak, B.V., Gendron, A.S. and Mosoiu, A.M., Borate buffer equilibria in nickel refining electrolytes, Journal of Applied Electrochemistry, (7)6, 1977, pp. 495-500.

Tomastik, J. and Ctvrtlik, R., Nanoscratch test: Tool for evaluation of cohesive and adhesive properties of thin films and coatings, EPJ Web of Conferences, (48), 2013, pp. 1-4.

Totten, G.E., Fatigue crack propagation, Advanced Materials and Processes, (166)5, 2008, pp. 39-41.

Trejo, G., Frausto-Reyes, C., Gama, S.C., Meas, Y. and Orozco, G., Raman study of benzylideneacetone on silver, International Journal of Electrochemical Science, (7)9, 2012, pp. 8436-8443.

Vlassak, J., Thin film mechanics: Overview, DEAS Harvard University, 2004, pp. 1-26.

Watson, S.A., Nickel sulfate solutions, Nickel Development Institute, from Google: https://nickelinstitute.org/Media/Files, 1989, pp. 1-5.

Watson, S.W. and Walters, R.P., The effects of chromium particles on nickel electrodeposition, Journal of The Electrochemical Society, (138)12, 1991, pp. 3633-3637.

Web., Element data, Technical data for the element, from Google: periodictable.com/Element/data, 2016.

Wikipedia, data page, Hardness of elements, reduction potential table, Thermal expansion, from Google: http://www.en.m.wikipedia.org, 2015.

Withers, P.J. and Bhadeshia, H.K.D.H., Residual stress: Part 1- Measurement techniques, Materials Science and Technology, (17)4, 2001, pp. 355-365.

Woo, Y. and Kim, S., Sensitivity analysis of plating conditions on mechanical properties of thin films for MEMS applications, Journal of Mechanical Science and Technology, (25)4, 2011, pp. 1017-1022.

Wu, R., Oliazedeh, M. and Alfantazi, A.M., Electrical conductivity and density of $NiSO_4/H_2SO_4$ solutions in the range of modern nickel electrorefining and electrowinning electrolyte, Journal of Applied Electrochemistry, (33)11, 2003, pp. 1043-1047.

Yan, S., Strengthening aluminium by zirconium and chromium, Master's thesis, 2012, Worcester Polytechnic Institute, United States.

Yin, K.M. and Lin, K.T., Effect of boric acid on the electrodeposition of iron, nickel and iron-nickel, Surface and Coatings Technology, (78)1-3, 1996, pp. 205-210.

Zech, N. and Landolt, D., The influence of boric acid and sulfate ions on the hydrogen formation in Ni-Fe plating electrolytes, Electrochimica Acta, (45)21, 2000, pp. 3461-3471.

Ziebell, T.D. and Schuh, C.A., Residual stress in electrodeposited nanocrystalline nickel-tungsten coatings, Journal of Material Research, (27)9, 2012, pp. 1271-1284.

Zhao, L., Chen, K., Patnaik, P.C., Tse, J.S., Elastic properties of multi-component nickel solid solutions, The Minerals, Metals & Materials Society, K1A OR6, 2004, pp. 1-6.

7. Appendices

Appendix 1.

A Linear Variable Differential Transformer (LVDT) of high sensitivity (750 mV/mm at 10 V DC), of stroke – 5 to +5 mm for – 3000 to + 3000 mV characteristics from Solartron as transducer, coupled to a datataker DT 50 as signal conditioner, was used to detect the linear bottom substrate deflection for the stress measurement via Stoney's equation as mentioned in Section 3.2. The final change of potential read at the end of experiments and the relative deflections and measured stresses are presented in the Table A1.9 to A1.20 from which the average stresses were calculated as indicated in Tables A1.1 to A1.8.

Table A1.1. Internal stress in nickel with copper-containing electrolytes.

Cu concentration in the electrolyte(mg/L)	0	5	10	15	20	25	40	50
Average stress (MPa)	213.7	223.6	229.5	238.8	255.6	291.5	425.1	518.2
Standard deviation	0.129	0.140	0.208	0.135	0.114	0.154	0.146	0.164
Measured stress (Mpa) Experiment 1	213.6	223.5	229.7	238.9	255.5	291.3	425.0	518.1
Measured stress (Mpa) Experiment 2	213.7	223.7	229.3	238.6	255.7	291.5	425.1	518.1
Measured stress (Mpa) Experiment 3	213.9	223.7	229.6	238.8	255.5	291.6	425.3	518.4

Table A1.2. Internal stress in nickel with copper-containing electrolytes (continued).

Cu concentration in the electrolyte(mg/L)	60	80	100	250	300	500
Average stress (MPa)	550.1	580.2	599.1	615.3	625.0	663.9
Standard deviation	0.187	0.129	0.151	0.190	0.118	0.171
Measured stress (Mpa) Experiment 1	550.3	580.1	599.1	615.1	625.1	663.8
Measured stress (Mpa) Experiment 2	550.1	580.4	599.0	615.5	625.0	663.8
Measured stress (Mpa) Experiment 3	550.0	580.2	599.3	615.4	624.9	664.1

Table A1.3. Internal stress in nickel with cobalt-containing electrolytes.

Co concentration in the electrolyte(mg/L)	0	5	10	15	20	25	40
Average stress (MPa)	213.7	212.0	210.6	209.0	207.3	205.6	207.0
Standard deviation	0.129	0.117	0.189	0.151	0.157	0.143	0.138
Measured stress (Mpa) Experiment 1	213.6	212.0	210.3	209.0	207.1	205.6	207.2
Measured stress (Mpa) Experiment 2	213.7	211.9	210.6	209.2	207.3	205.8	206.9
Measured stress (Mpa) Experiment 3	213.9	212.1	210.6	208.9	207.4	205.5	207.0

Table A1.4. Internal stress in nickel with cobalt-containing electrolytes (continued).

Co concentration in the electrolyte(mg/L)	50	60	80	100	250	300	500
Average stress (MPa)	210.104	212.0	214.2	216.3	242.9	255.2	291.5
Standard deviation	0.193	0.166	0.135	0.193	0.189	0.180	0.170
Measured stress (Mpa) Experiment 1	210.159	211.8	214.3	216.1	243.0	255.2	291.7
Measured stress (Mpa) Experiment 2	210.264	212.1	214.2	216.4	242.7	255.4	291.4
Measured stress (Mpa) Experiment 3	209.889	212.025	214.1	216.5	243.0	255.0	291.4

Table A1.5. Internal stress in nickel with aluminium-containing electrolytes.

Al concentration in the electrolyte(mg/L)	0	5	10	15	20	25	40	50
Average stress (MPa)	213.7	257.9	284.1	320.7	359.0	395.2	502.2	541.1
Standard deviation	0.129	0.127	0.174	0.125	0.182	0.158	0.114	0.180
Measured stress (Mpa) Experiment 1	213.6	257.9	284.0	320.9	359.2	395.4	502.3	541.1
Measured stress (Mpa) Experiment 2	213.7	257.7	284.0	320.7	359.0	395.2	502.1	541.3
Measured stress (Mpa) Experiment 3)	213.9	258.0	284.3	320.6	358.8	395.1	502.2	541.0

Table A1.6. Internal stress in nickel with aluminium-containing electrolytes (continued).

Al concentration in the electrolyte(mg/L)	60	80	100	300	500	625	1250	2500
Average stress (MPa)	568.2	647.1	695.2	853.0	601.1	550.3	315.1	230.1
Standard deviation	0.177	0.100	0.167	0.130	0.140	0.149	0.105	0.132
Measured stress (Mpa) Experiment 1	568.4	647.0	695.4	853.0	601.2	550.2	315.2	230.2
Measured stress (Mpa) Experiment 2	568.2	647.2	695.2	853.1	601.2	550.5	315.0	230.2
Measured stress (Mpa) Experiment 3	568.1	647.1	695.1	852.9	601.0	550.4	315.1	230.0

Table A1.7. Internal stress in nickel with chromium-containing electrolytes.

Cr concentration in the electrolyte(mg/L)	0	5	10	15	20	25
Average stress (MPa)	213.7	258.7	290.5	328.0	363.1	397.0
Standard deviation	0.129	0.148	0.196	0.149	0.155	0.134
Measured stress (Mpa) Experiment 1	213.6	258.7	290.3	327.8	363.2	397.1
Measured stress (Mpa) Experiment 2	213.7	258.9	290.5	328.0	362.9	396.9
Measured stress (Mpa) Experiment 3	213.9	258.6	290.7	328.1	363.2	396.9

Table A1.8. Internal stress in nickel with chromium-containing electrolytes (continued).

Cr concentration in the electrolyte(mg/L)	40	50	60	80	100
Average stress (MPa)	509.8	570.1	643.2	780.9	922.0
Standard deviation	0.082	0.182	0.146	0.140	0.157
Measured stress (Mpa) Experiment 1	509.8	570.3	643.1	780.9	922.1
Measured stress (Mpa) Experiment 2	509.9	570.0	643.4	780.7	921.9
Measured stress (Mpa) Experiment 3	509.7	570.0	643.1	781.0	921.9

Table A1.9. Stress measurement with copper-containing electrolytes: Experiment1.

Impurity	Impurity concentration in the electrolyte (mg/L)	LVDT voltage (V)	Final Potential change read (mV)	Calculated deflection (mm)	Measured stress (MPa)
Cu	0	10	952.9	1.270	213.6
Cu	5	10	996.8	1.329	223.5
Cu	10	10	1024.6	1.370	229.7
Cu	15	10	1065.6	1.420	238.9
Cu	20	10	1139.7	1.520	255.5
Cu	25	10	1299.3	1.732	291.3
Cu	40	10	1895.4	2.527	425.0
Cu	50	10	2310.7	3.081	518.1
Cu	60	10	2454.5	3.273	550.3
Cu	80	10	2587.4	3.450	580.1
Cu	100	10	2672.2	3.563	599.1
Cu	250	10	2743.5	3.658	615.1
Cu	300	10	2788.1	3.718	625.1
Cu	500	10	2960.7	3.948	663.8

Table A1.10. Stress measurement with copper-containing electrolytes: Experiment 2.

Impurity	Impurity concentration in the electrolyte (mg/L)	LVDT voltage (V)	Final Potential change read (mV)	Calculated deflection (mm)	Measured stress (Mpa)
Cu	0	10	953.1	1.271	213.7
Cu	5	10	997.8	1.330	223.7
Cu	10	10	1022.8	1.364	229.3
Cu	15	10	1064.4	1.419	238.6
Cu	20	10	1140.6	1.521	255.7
Cu	25	10	1300.1	1.733	291.5
Cu	40	10	1896.1	2.528	425.1
Cu	50	10	2310.6	3.081	518.1
Cu	60	10	2453.5	3.271	550.1
Cu	80	10	2588.5	3.451	580.4
Cu	100	10	2671.6	3.562	599.0
Cu	250	10	2745.0	3.660	615.5
Cu	300	10	2787.5	3.717	625.0
Cu	500	10	2960.6	3.947	663.8

Table A1.11. Stress measurement with copper-containing electrolytes: Experiment 3.

Impurity	Impurity concentration in the electrolyte (mg/L)	LVDT voltage (V)	Final Potential change read (mV)	Calculated deflection (mm)	Measured stress (Mpa)
Cu	0	10	954.0	1.272	213.9
Cu	5	10	997.9	1.330	223.7
Cu	10	10	1023.9	1.365	229.6
Cu	15	10	1065.1	1.420	238.8
Cu	20	10	1139.7	1.520	255.5
Cu	25	10	1300.7	1.734	291.6
Cu	40	10	1896.7	2.529	425.3
Cu	50	10	2312.0	3.083	518.4
Cu	60	10	2452.8	3.270	550.0
Cu	80	10	2587.7	3.450	580.2
Cu	100	10	2672.9	3.564	599.3
Cu	250	10	2744.9	3.660	615.4
Cu	300	10	2787.1	3.716	624.9
Cu	500	10	2962.0	3.949	664.1

Table A1.12. Stress measurement with cobalt-containing electrolytes: Experiment 1.

Impurity	Impurity concentration in the electrolyte (mg/L)	LVDT voltage (V)	Final Potential change read (mV)	Calculated deflection (mm)	Measured stress (Mpa)
Co	0	10	952.	1.270	213.6
Co	5	10	945.6	1.261	212.0
Co	10	10	937.9	1.251	210.3
Co	15	10	932.1	1.243	209.0
Co	20	10	923.6	1.232	207.1
Co	25	10	917.0	1.222	205.6
Co	40	10	924.0	1.232	207.2
Co	50	10	937.3	1.250	210.2
Co	60	10	944.6	1.260	211.8
Co	80	10	956.0	1.275	214.3
Co	100	10	963.9	1.285	216.1
Co	250	10	1083.8	1.445	243.0
Co	300	10	1138.2	1.518	255.2
Co	500	10	1300.9	1.734	291.7

Table A1.13. Stress measurement with cobalt-containing electrolytes: Experiment 2.

Impurity	Impurity concentration in the electrolyte (mg/L)	LVDT voltage (V)	Final Potential change read (mV)	Calculated deflection (mm)	Measured stress (Mpa)
Co	0	10	953.1	1.271	213.7
Co	5	10	944.9	1.260	211.9
Co	10	10	939.3	1.252	210.6
Co	15	10	933.1	1.244	209.2
Co	20	10	924.7	1.233	207.3
Co	25	10	917.9	1.224	205.8
Co	40	10	922.8	1.230	206.9
Co	50	10	937.8	1.250	210.3
Co	60	10	946.1	1.261	212.1
Co	80	10	955.3	1.274	214.2
Co	100	10	965.2	1.287	216.4
Co	250	10	1082.4	1.443	242.7
Co	300	10	1139.1	1.519	255.4
Co	500	10	1299.6	1.733	291.4

Table A1.14. Stress measurement with cobalt-containing electrolytes: Experiment 3.

Impurity	Impurity concentration in the electrolyte (mg/L)	LVDT voltage (V)	Final Potential change read (mV)	Calculated deflection (mm)	Measured stress (Mpa)
Co	0	10	954.0	1.272	213.9
Co	5	10	945.9	1.261	212.1
Co	10	10	939.4	1.253	210.6
Co	15	10	931.8	1.242	208.9
Co	20	10	925.0	1.233	207.4
Co	25	10	916.7	1.222	205.5
Co	40	10	923.2	1.231	207.0
Co	50	10	936.1	1.248	209.9
Co	60	10	945.7	1.261	212.0
Co	80	10	954.8	1.273	214.1
Co	100	10	965.6	1.287	216.5
Co	250	10	1083.9	1.445	243.0
Co	300	10	1137.5	1.517	255.0
Co	500	10	1299.5	1.733	291.4

Table A1.15. Stress measurement with chromium-containing electrolytes: Experiment 1.

Impurity	Impurity concentration in the electrolyte (mg/L)	LVDT voltage (V)	Final Potential change read (mV)	Calculated deflection (mm)	Measured stress (Mpa)
Cr	0	10	952.9	1.271	213.6
Cr	5	10	1153.8	1.538	258.7
Cr	10	10	1294.9	1.726	290.3
Cr	15	10	1462.2	1.950	327.8
Cr	20	10	1619.8	2.160	363.2
Cr	25	10	1771.2	2.362	397.1
Cr	40	10	2273.7	3.032	509.8
Cr	50	10	2543.7	3.392	570.3
Cr	60	10	2868.4	3.824	643.1
Cr	80	10	3482.8	4.644	780.9
Cr	100	10	4112.9	5.484	922.1

Table A1.16. Stress measurement with chromium-containing electrolytes: Experiment 2.

Impurity	Impurity concentration in the electrolyte (mg/L)	LVDT voltage (V)	Final Potential change read (mV)	Calculated deflection (mm)	Measured stress (Mpa)
Cr	0	10	953.1	1.271	213.7
Cr	5	10	1154.7	1.540	258.9
Cr	10	10	1295.7	1.728	290.5
Cr	15	10	1462.9	1.950	328.0
Cr	20	10	1618.6	2.158	362.9
Cr	25	10	1770.1	2.360	396.9
Cr	40	10	2274.2	3.032	509.9
Cr	50	10	2542.3	3.390	570.0
Cr	60	10	2869.6	3.826	643.4
Cr	80	10	3482.2	4.643	780.7
Cr	100	10	4111.7	5.482	921.9

Table A1.17. Stress measurement with chromium-containing electrolytes: Experiment 3.

Impurity	Impurity concentration in the electrolyte (mg/L)	LVDT voltage (V)	Final Potential change read (mV)	Calculated deflection (mm)	Measured stress (Mpa)
Cr	0	10	954.0	1.272	213.9
Cr	5	10	1153.3	1.538	258.6
Cr	10	10	1296.6	1.729	290.7
Cr	15	10	1463.5	1.951	328.1
Cr	20	10	1619.7	2.160	363.2
Cr	25	10	1770.3	2.360	396.9
Cr	40	10	2273.5	3.031	509.7
Cr	50	10	2542.3	3.390	570.0
Cr	60	10	2868.5	3.825	643.1
Cr	80	10	3483.4	4.645	781.0
Cr	100	10	4111.6	5.482	921.9

Table A1.18. Stress measurement with aluminium-containing electrolytes: Experiment 1.

Impurity	Impurity concentration in the electrolyte (mg/L)	LVDT voltage (V)	Final Potential change read (mV)	Calculated deflection (mm)	Measured stress (Mpa)
Al	0	10	952.9	1.270	213.6
Al	5	10	1150.2	1.534	257.9
Al	10	10	1266.8	1.689	284.0
Al	15	10	1431.1	1.908	320.9
Al	20	10	1602.1	2.136	359.2
Al	25	10	1763.6	2.351	395.4
Al	40	10	2240.5	2.987	502.3
Al	50	10	2413.3	3.218	541.1
Al	60	10	2535.2	3.380	568.4
Al	80	10	2885.8	3.848	647.0
Al	100	10	3101.7	4.136	695.4
Al	300	10	3804.5	5.073	853.0
Al	500	10	2681.4	3.575	601.2
Al	625	10	2453.8	3.272	550.2
Al	1250	10	1405.9	1.874	315.2
Al	2500	10	1026.7	1.369	230.2

Table A1.19. Stress measurement with aluminium-containing electrolytes: Experiment 2.

Impurity	Impurity concentration in the electrolyte (mg/L)	LVDT voltage (V)	Final Potential change read (mV)	Calculated deflection (mm)	Measured stress (Mpa)
Al	0	10	953.1	1.270	213.7
Al	5	10	1149.5	1.532	257.7
Al	10	10	1266.7	1.689	284.0
Al	15	10	1430.3	1.907	320.7
Al	20	10	1601.2	2.135	359.0
Al	25	10	1762.5	2.350	395.2
Al	40	10	2239.5	2.986	502.1
Al	50	10	2414.4	3.219	541.3
Al	60	10	2534.2	3.379	568.2
Al	80	10	2886.6	3.849	647.2
Al	100	10	3100.5	4.134	695.2
Al	300	10	3805.1	5.073	853.1
Al	500	10	2681.5	3.575	601.2
Al	625	10	2455.2	3.274	550.5
Al	1250	10	1404.9	1.873	315.0
Al	2500	10	1026.9	1.369	230.2

Table A1.20. Stress measurement with aluminium-containing electrolytes: Experiment 3.

Impurity	Impurity concentration in the electrolyte (mg/L)	LVDT voltage (V)	Final Potential change read (mV)	Calculated deflection (mm)	Measured stress (Mpa)
Al	0	10	954.0	1.272	213.9
Al	5	10	1150.6	1.534	258.0
Al	10	10	1268.0	1.691	284.3
Al	15	10	1430.0	1.907	320.6
Al	20	10	1600.5	2.134	358.8
Al	25	10	1762.3	2.350	395.1
Al	40	10	2239.9	2.987	502.2
Al	50	10	2412.8	3.217	541.0
Al	60	10	2533.7	3.378	568.1
Al	80	10	2886.4	3.848	647.1
Al	100	10	3100.3	4.134	695.1
Al	300	10	3803.9	5.072	852.9
Al	500	10	2680.4	3.574	601.0
Al	625	10	2454.7	3.273	550.4
Al	1250	10	1405.5	1.874	315.1
Al	2500	10	1025.8	1.368	230.0

Graphs in Figures 4.3a to 4.6a were constructed with manipulation of the raw data presented in Tables A1.1 to A1.8 and 4.1.

Appendix 2.

A Perkin Elmer ELAN 6100 Inductively Coupled Plasma-Mass Spectrometer was used for ICP-MS analyses. Readings given in millilitre (ml) were multiplied by a constant (dilution factor) relative to the dilution made for the sensitivity of the element to convert in weight percentage (m%). The composition in atom percentage (at%) was obtained using the formulae A2 and data are given in Table A2.1 to A2.2 below where Me, M and A are relative to the impurity, mass (g) and the atomic mass (g) respectively.

$$at\% = (M_{Me}/A_{Me}) / (M_{Me}/A_{Me} + M_{Ni}/A_{Ni}) \qquad (A2)$$

Table A2.1. ICP data results for nickel deposited from aluminium- and cobalt-containing electrolytes.

Impurity concentration in the electrolyte (mg/L)	Al reading (mg/L)	m% Al	%at Al	Co reading (mg/L)	m% Co	%at Co
10	0.2	0.004	0.01	1.1	0.22	0.22
15						
20	0.6	0.012	0.03	1.3	0.26	0.26
50				2	0.4	0.4
80						
100				4	0.8	0.8
250				8.4	1.68	1.67
300	7.8	0.156	0.34			
500				17	3.4	3.39
625	2.9	0.058	0.13			
1250	1	0.02	0.04			
2500	0.6	0.012	0.03			

Table A2.2. ICP data results for nickel deposited from copper- and chromium-containing electrolytes.

Impurity concentration in the electrolyte (mg/L)	Cu reading (mg/L)	m% Cu	%at Cu	Cr reading (mg/L)	m% Cr	%at Cr
10	0.3	0.12	0.11	0.04	0.005	0.01
15	0.6	0.24	0.22			
20	0.8	0.32	0.30	0.1	0.012	0.01
50				0.2	0.025	0.03
80				0.36	0.045	0.05
100	1.5	0.6	0.55	0.5	0.0625	0.07
250	4	1.6	1.48			
300						
500	7.5	0.3	2.78			
625						
1250						
2500						

Graphs in figures 4.3b to 4.6b, 4.8, and 4.9 were constructed with manipulation of the raw data presented in Tables A2.1 and A2.2.

Appendix 3

The cathodic overpotentials on a titanium electrode polarized galvanostatically at 215 A/m^2 from aluminium and chromium containing electrolytes were obtained the figures 4.9 and 4.10, outcome of potentiodynamic scan tests, by subtracting 0.56 V (plating potential) from the actual potential.

Table A3.1. Electrode cathodic overpotentials at 215 A/m^2 from aluminium- and chromium-containing electrolytes during potentiodynamic tests.

Impurity concentration in the electrolyte (mg/L)	Cathodic potential for Al containing electrolytes (V)	Cathodic overpotential for Al containing electrolytes (V)	Cathodic potential for Cr containing electrolytes (V)	Cathodic overpotential for Cr containing electrolytes (V)
0	1.000	0.440	1.000	0.440
20	0.981	0.421	0.997	0.437
50	0.910	0.350	0.974	0.414
80			0.901	0.341
100	0.872	0.312	0.890	0.330
625	0.889	0.329		
1250	0.949	0.389		
2500	0.949	0.389		

Graphs in figure 4.11 were constructed with manipulation of the raw data presented in Table A3.1.

Appendix 4

When progressively applying normal loads to the indenter with singular weights of 1g each and recording friction forces using a liquid-crystal display (LCD) small portable scale of 100 g x 0.01 and an actuator as described in the paragraph 3.4 during the scratch tests, data have been collected. For simplification, Tables A4.1 to A4.4 present only data obtained after every 10 more weights from start and those obtained around the critical load as in the plots. Friction coefficients were calculated by the formulae 7.1.using data at critical loads.

$$\mu_k = \Delta F_n / \Delta F_f \qquad (7.1)$$

Table A4.1. Applied loads and friction forces recorded for nickel deposited from copper-containing electrolytes.

Applied normal load (g)	Friction force at 0 mg/L Cu	Friction force at 5 mg/L Cu	Friction force at 10 mg/L Cu	Friction force at 15 mg/L Cu	Friction force at 20 mg/L Cu
1	23.11	19.35	16.03	12.17	9.12
10	24.15	20.62	17.59	13.87	11.17
20	25.1	21.9	19.01	15.52	13.12
30	26.09	23.27	20.53	17.28	15.14
31					
32					
33					
34					
35					
36					16.32
37				18.46	16.77
38				18.96	
39			21.88		
40	27.1	24.52	22.44		
41		24.65			
42	27.3	25.25			
43	27.95				
44					

Table A4.2. Applied loads and friction forces recorded for nickel deposited from cobalt-containing electrolytes.

Applied normal load (g)	Friction force at 0 mg/L Co	Friction force at 5 mg/L Co	Friction force at 10 mg/L Co	Friction force at 15 mg/L Co	Friction force at 20 mg/L Co
1	23.11	20.81	18.37	16.52	14.59
10	24.15	21.91	19.55	17.86	15.99
20	25.1	23.09	20.77	19.16	17.35
30	26.09	24.11	21.94	20.41	18.79
31					
32					
33					
34					
35					
36					
37					
38					19.91
39				21.63	20.43
40	27.1	25.21	23.17	22.18	
41		25.32	23.75		
42	27.3	25.94			
43	27.95				
44					

Table A4.3. Applied loads and friction forces recorded for nickel deposited from chromium-containing electrolytes.

Apllied normal load (g)	Friction force at 0 mg/L Cr	Friction force at 5 mg/L Cr	Friction force at 10 mg/L Cr	Friction force at 15 mg/L Cr	Friction force at 20 mg/L Cr
1	23.11	20.6	18.01	14.81	12.86
10	24.15	21.73	19.37	16.37	14.46
20	25.1	22.8	20.61	17.83	16.04
30	26.09	23.91	21.91	19.37	17.69
31					
32					
33					18.14
34					18.69
35				20.12	
36				20.69	
37					
38			22.95		
39			23.55		
40	27.1	25			
41		25.63			
42	27.3				
43	27.95				
44					

Table A4.4. Applied loads and friction forces recorded for nickel deposited from aluminium-containing electrolytes.

Apllied normal load (g)	Friction force at 0 mg/L Al	Friction force at 5 mg/L Al	Friction force at 10 mg/L Al	Friction force at 15 mg/L Al	Friction force at 20 mg/L Al
1	23.11	18.7	14.23	10.01	6.58
10	24.15	19.9	15.66	11.6	8.4
20	25.1	21.16	17.03	13.2	10.2
30	26.09	22.27	18.43	14.85	12
31					12.4
32					
33				15.28	
34				15.74	
35					
36					
37			19.41		
38			19.93		
39					
40	27.1	23.5			
41		24.09			
42	27.3				
43	27.95				
44					

Graphs in Figures 4.15 to 4.19 were constructed with manipulation of the raw data presented in Tables A4.1 to A4.4.